

# Software tools for quantum control: Improving quantum computer performance through noise and error suppression

Harrison Ball,<sup>1</sup> Michael J. Biercuk,<sup>1,\*</sup> Andre Carvalho,<sup>1</sup> Rajib Chakravorty,<sup>1</sup> Jiayin Chen,<sup>1</sup> Leonardo A. de Castro,<sup>1</sup> Steven Gore,<sup>1</sup> David Hover,<sup>1</sup> Michael Hush,<sup>1</sup> Per J. Liebermann,<sup>1</sup> Robert Love,<sup>1</sup> Kevin Nguyen,<sup>1</sup> Viktor S. Perunicic,<sup>1</sup> Harry J. Slatyer,<sup>1</sup> Claire Edmunds,<sup>2</sup> Virginia Frey,<sup>2</sup> Cornelius Hempel,<sup>2</sup> and Alistair Milne<sup>2</sup>

<sup>1</sup>*Q-CTRL, Sydney, NSW Australia & Los Angeles, CA USA*

<sup>2</sup>*ARC Centre for Engineered Quantum Systems, The University of Sydney, NSW Australia*

(Dated: April 24, 2022)

Effectively manipulating quantum computing hardware in the presence of imperfect devices and control systems is a central challenge in realizing useful quantum computers. Susceptibility to noise in particular limits the performance and algorithmic capabilities experienced by end users. Fortunately, in both the NISQ era and beyond, quantum control enables the efficient execution of quantum logic operations and quantum algorithms exhibiting robustness to errors, without the need for complex logical encoding. In this manuscript we introduce the first commercial-grade software tools for the application and integration of quantum control in quantum computing research from Q-CTRL, serving the needs of hardware R&D teams, algorithm developers, and end users. We survey quantum control and its role in combating noise and instability in near-term devices; our primary focus is on quantum firmware, the low-level software solutions designed to enhance the stability of quantum computational hardware at the physical layer. We explain the benefits of quantum firmware not only in error suppression, but also in simplifying higher-level compilation protocols and enhancing the efficiency of quantum error correction. Following this exposition, we provide an overview of Q-CTRL’s classical software tools for creating and deploying optimized quantum control solutions at various layers of the quantum computing software stack. We describe our software architecture leveraging both high-performance distributed cloud computation and local custom integration into hardware systems, and explain how key functionality is integrable with other software packages and quantum programming languages. Our presentation includes a detailed technical overview of central product features including a multidimensional control-optimization engine, engineering-inspired filter functions for high-dimensional Hilbert spaces, and a new approach to noise characterization. Finally, we present a series of case studies demonstrating the utility of quantum control solutions derived from these tools in improving the performance of trapped-ion and superconducting quantum computer hardware.

## CONTENTS

I. Introduction	2	B. Performance evaluation for arbitrary controls	12
II. Quantum control for quantum computing	3	1. Modelling noise and error in D-dimensional systems	13
A. Quantum firmware: embedding control at the physical layer	4	2. Multi-dimensional filter functions in the frequency domain	13
B. The benefits of quantum control across the quantum computing stack	5	C. Optimization tools to maximize control performance	14
III. Q-CTRL product architecture and integrations	6	1. Optimizer framework	15
A. Product overview	7	2. Constrained Optimizations	16
B. Cloud-compute architecture	8	3. Optimizer performance benchmarking	16
C. Quantum programming language integration via Python	9	D. Time-domain simulation tools for realistic hardware error processes	16
D. Quantum computer hardware integration	9	1. Technical details of simulation functionality	18
IV. Technical functionality overview	11	2. Simulation example	20
A. General quantum-control setting	11	E. Characterizing hardware noise	20
1. Optimal quantum control	11	V. Quantum control case studies	22
2. Robust quantum control	12	A. Open-loop control benefits demonstrated in trapped-ion QCs	23
		B. Simultaneous leakage and noise-robust controls for superconducting circuits	25
		C. Robust control for parametrically-driven superconducting entangling gates	25

\* Also ARC Centre for Engineered Quantum Systems, The University of Sydney, NSW Australia

D. Experimental noise characterization of multiqubit circuits on an IBM cloud QC	29	References	49
E. Crosstalk-resistant circuit compilation	31		
VI. Conclusion and outlook	33		
Acknowledgements	33		
A. Appendix: Technical Definitions	34	I. INTRODUCTION	33
1. Fourier transform	34	The emergence of NISQ-era [1] quantum computing hardware at the scale of a few tens of qubits has led to an explosion of interest from end-users and software developers. Today's boom in quantum software is predominantly focused on application mapping and algorithmic development. A cultural shift in the community away from exclusively seeking algorithms which provide provable asymptotic scaling advantages to identifying applications providing any commercially relevant computational advantage [2] has also served as an accelerant for the nascent quantum software industry. But as in conventional software engineering there is much that lies beneath the most visible layers of the software stack [3] in providing the ultimate functionality and computational advantages the quantum information community is seeking (Fig. 1).	34
2. Frobenius inner product	34		34
3. Frobenius norm	34		34
4. Approximations	34		34
5. Power spectral density	35		35
B. Control Hamiltonian	35		
1. Generalized formalism	36	The key challenge we consider is the efficient manipulation of quantum computing hardware with the objective of extracting optimal performance at the device, circuit, and algorithmic levels. The central impediment is the influence of noise and error in quantum computing hardware; electromagnetic noise in its various forms is responsible for both diminished coherent lifetimes through the process of decoherence and reduction in the fidelity of quantum logic operations when quantum devices are manipulated by faulty classical hardware. Both, taken together, ultimately limit the range of achievable computations on quantum coherent hardware, measured via metrics such as circuit depth or quantum volume [4].	36
2. Control solutions	36		36
3. Control segments	36		36
4. Control coordinates	37		37
C. Multidimensional filter function derivations	38		
1. Magnus expansion	38		
2. Spectral representation of Magnus term	38		
3. Leading order robustness infidelity	39		
4. Leading-order filter functions	39		
D. Technical details on implementation of the SVD noise reconstruction	40		
1. Measurement uncertainties for SVD reconstruction	40		
2. Filter function normalization	40		
3. Calculating weights due to sensitivity	40		
4. Singular value truncation to prevent numeric instability	41		
E. Methods for experimental demonstrations of quantum control benefits	41		
1. Quasi-static error robustness	41	Susceptibility to noise and error remains the Achilles heel of quantum computers, and stabilizing hardware against noise via <i>e.g.</i> quantum error correction (QEC) [5], has been a major driver of research in the field. The complexity of QEC, however, motivates consideration of alternative techniques in the near-term which do not rely on full fault-tolerant encoding. Even beyond the current era, QEC, for its virtues in underpinning the asymptotic scaling of quantum computers, appears a resource intensive tool for error mitigation in isolation. Realizing practical, functional machines in the NISQ-era and beyond thus requires continued development of techniques to augment the noise and error robustness of quantum computing hardware, outside of QEC.	41
2. Suppression of time-varying noise	42		42
3. Error homogenization characterized via 10-qubit parallel randomized benchmarking	42		42
4. Molmer-Sorensen drift measurements	42		42
F. Product Features Summary	43		
1. BLACK OPAL	43		
2. BOULDER OPAL	43		
3. OpenControls	43		
4. Devkit	44		
G. BLACK OPAL Visualizations of noise and control in quantum circuits	44		
H. Details on cloud architecture	45		
1. Presentation tier	46	In the classical domain, working to stabilize an unstable system against disturbance from its environment is frequently the domain of control engineering [6, 7]. Control engineering, as a modern discipline, is fundamental to nearly all of our technological industries. Control allowed the Wright brothers to achieve manned, powered, controlled flight at a time when others could not [8]. The concepts they introduced to the crowded aviation field—notably three-axis control and deformable airfoils—would be considered control engineering contri-	45
2. Logic tier	46		46
3. Data tier	48		48
4. Infrastructure	48		48

butions today. Similar stories have played out in autonomous vehicles, walking robots, and even the operation of computer memory [9]. Control has built industries before, and in our view quantum control will be just as essential in the development of the emerging quantum computing industry.

Considerable effort has already been taken to adapt the concepts of control engineering to the strictures of quantum coherent devices in research and in practice [10–19]. Adoption of many of the physical concepts underlying quantum control is already ubiquitous across the field; every team that employs a spin-echo to eliminate unwanted couplings between qubits or to mitigate slowly fluctuating ambient magnetic fields is leveraging the physics of coherent averaging [20]. Similarly, optimal control has been begun to emerge as a powerful technique to manipulate complex Hilbert spaces [21–23], or optimize quantum hardware performance [24–26].

Increasing the uptake and utility of these techniques as the quantum computing community grows and diversifies requires access to effective, user-friendly, professionally engineered support software. Users with limited expertise in the research discipline of quantum control must be able to use these tools to apply and integrate quantum control techniques into quantum computing research. Moreover, much like critical security software for conventional cloud computing, it is essential that professionally engineered solutions are available from specialist providers; the functionality provided is essential for business continuity, risk mitigation, and maintainability.

Such tools, however, have been lacking in the community, with most academic teams writing their own specialized code or hacking existing software packages derived from other fields such as NMR. This approach is cost-inefficient, leads to inconsistent results between teams, fails to deliver on the most up-to-date knowledge from research community, and has substantial negative consequences as students and staff inevitably move on from current roles. Professionally engineered quantum control software will become as important to the emerging quantum computing industry as security software is to modern cloud computing; current *DIY* approaches are unsustainable.

In this manuscript we introduce a set of professionally engineered infrastructure software tools aimed at building and integrating error-robust quantum control strategies in the quantum computing stack. One key objective is the deterministic suppression of the influence of noise in quantum logic operations and quantum algorithms, providing greater functionality from fixed computational resources (measured in qubits, gates, and compute runtime). In our presentation we describe how quantum control suppresses errors in hardware, but also how it can enable simplification of compilation at higher levels of the stack by mitigation of performance variations in space and time, and builds compatibility with quantum error correction in the long term.

In support of the integration of these capabilities in the

design and operation of quantum computers, we introduce a suite of classical software tools which allow users to create and deploy quantum control solutions across the software stack—from the physical layer through to algorithmic design. These tools, engineered leveraging a modern cloud-compute architecture, ensure that computationally complex tasks such as the optimization of multi-dimensional unitary transformations are handled efficiently while ensuring compatibility with other parts of the computational stack and long-term maintainability. We describe how these tools may be integrated with conventional programming workflows in Python, cloud-based quantum computers, and custom quantum computing hardware. Our presentation includes a detailed technical discussion of new algorithmic approaches to control design and optimization, performance evaluation and validation, and control hardware characterization. These functions are validated and demonstrated through a series of case studies tied to real problems in quantum computing hardware.

The remainder of this manuscript is organized as follows. In Sec. II we introduce the fundamental concepts and utility of quantum control as it pertains to the challenges building useful quantum computers. This is followed by an overview of Q-CTRL’s classical software products for the development and deployment of quantum control in Sec. III. We then move on to present a technical, mathematical treatment of novel functionality we have developed in Sec. IV before presenting a series of technical case studies deploying these tools and capabilities to solve real problems in Sec. V. We then conclude with a brief summary and future outlook of forthcoming product and feature development.

## II. QUANTUM CONTROL FOR QUANTUM COMPUTING

Control engineering provides powerful tools permitting the abstraction of complex physical systems away from microscopic models, and permitting efficient and stable manipulation of hardware. In the quantum domain many of the familiar concepts at work for control of classical technologies must be amended, and a simple one-to-one translation of textbook control engineering concepts rarely succeeds. For instance, quantum systems of interest to quantum computing are in general nonlinear (control over qubits is formally bilinear), noise-processes of interest in the laboratory are generally colored, and measurement has strong back-action on the plant (we will focus exclusively on the control of qubits rather than linear degrees of freedom such as harmonic oscillators). In this section we will describe how quantum control can bring benefits to quantum computing via integration at the physical layer as well as higher layers in the QC stack.

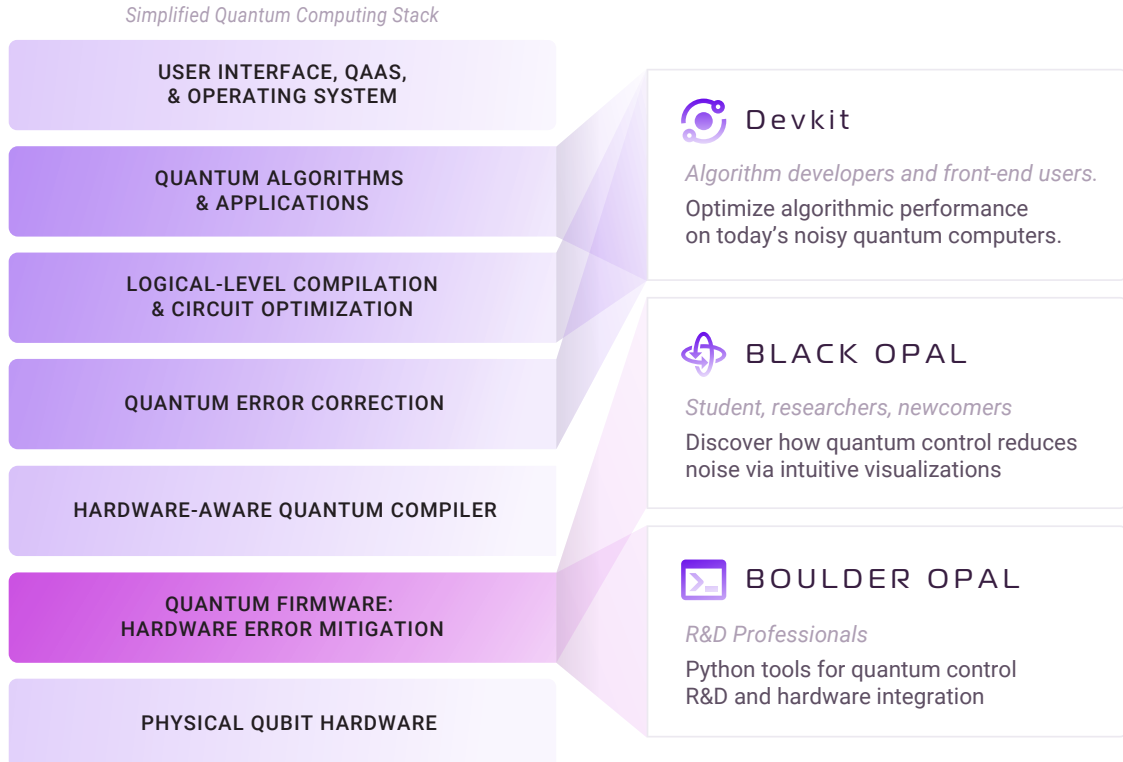


FIG. 1. The integration of Q-CTRL software products in the quantum computing stack. Left: A notional depiction of the key elements of the software stack in a quantum computer or *Quantum as a Service* (QAAS) cloud offering. Most quantum software development today spans the top two layers of the stack, with an emphasis on applications, algorithms, and programming languages. Infrastructure software spans all aspects of the middle of the stack from circuit compilation through to quantum firmware which exists at the classical-quantum interface. Right: Q-CTRL’s core products span the quantum compute stack. Most contribute capabilities at the quantum firmware layer; however, in addition to providing higher level benefits, products like the Q-CTRL Devkit help deploy control-theoretic insights and capabilities in error suppression to users such as application developers.

### A. Quantum firmware: embedding control at the physical layer

The stabilization of quantum devices or quantum logic operations against external perturbations is primarily designed to suppress hardware faults which contribute to computational errors. Decoherence during idle operations, for instance, results in loss or randomization of information stored in a qubit. Similarly, external instabilities in *e.g.* radiofrequency fields used to mediate multiqubit entanglement can result in reduced operational fidelity. Appropriate deployment of various forms of quantum control *at the physical layer* can therefore mitigate the deleterious effects of these perturbations and improve the logical error rate for quantum hardware. Because these techniques generally involve direct actuation on the devices used in performing computations, they interact with the physical layer in a generic quantum computing software stack [27], prior to any form of logical encoding used in fault-tolerant quantum error correction (Fig. 1). We refer to this class of protocols loosely as *firmware* as

they are usually software-defined but embedded at the physical layer and invisible to higher layers of abstraction (Quantum Error Correction is treated in the next subsection). Moreover, these techniques bear resemblance to other forms of firmware in computer engineering, such as DRAM refresh protocols [9] employed to stabilize classical memory hardware against charge leakage.

When considering quantum control in the context of hardware stabilization for qubits in quantum computers, we are generally presented with three interrelated control-engineering-inspired approaches:

- Measurement-free open-loop control
- Destructive closed-loop feedback via projective measurements
- Indirect closed-loop feedback which preserves quantum coherence via weak measurements or the use of ancillae.

Open-loop control refers to feedback-free actuation on a system, as in the case of a timed irrigation system which

can maintain a lawn without information on soil moisture or rainfall. It provides the substantial benefit that it is resource efficient and in the quantum domain has proven to be remarkably effective in stabilizing quantum devices both during free evolution and during nontrivial logic operations. In this framework, quantum logic operations are redefined to provide the same mathematical transformation within the computational space, but in a way that provides robustness against various error-inducing noise processes. The implementation of open-loop quantum control involves temporal modulation of incident control fields employed to enact manipulation of physical devices. Considerable literature exists in the NMR and EPR community concerned with geometric interpretations of how control design can be used to cancel errors or *decouple* unwanted Hamiltonian terms through dynamic decoupling sequences or composite pulse techniques [20, 28]. Due to its simplicity, ubiquity, and laboratory-validated performance we will focus substantially on this set of techniques in our technical discussion.

The use of feedback control, in which actuation is determined based on measurements of the system, is highly constrained [29] by the destructive nature of projective measurement in quantum mechanics [30]. While novel control strategies can be developed for predictive control [18, 31] during unsupervised periods, direct destructive measurements on data qubits are not commonly used within quantum computing architectures. These challenges may be mitigated through the use of indirect measurements on embedded sensor ancilla qubits [19, 32, 33]. Such techniques use physically proximal qubits as transducers to detect local noise in the device with actuation on unsupervised data qubits. Weak measurements also provide a means to stabilize data with minimal perturbation to the encoded quantum information, and have seen adoption in superconducting circuits [34] and NV diamond [35].

## B. The benefits of quantum control across the quantum computing stack

There has been much effort driven both from experimental hardware and software engineering teams to build tools addressing the multitude of practical problems inherent to running a functional quantum computer in the NISQ era and beyond. Nonetheless, the abstraction layers that have emerged in the quantum computing stack have remained reasonably isolated, each being developed largely independent of its neighbors. This is relevant for quantum-computer-science studies, but may present missed opportunities in the context of practical quantum-computer engineering. Ultimately, enabling practical, commercially relevant systems that provide computational advantages even in the presence of imperfect hardware requires consideration of broader benefits of quantum control, and the interface between abstraction layers across the QC software stack. Quantum control impacts

quantum computer system design and higher-level software abstractions through a variety of benefits (Fig. 2), and insights from this field have the potential to shape the *practical* implementation of many higher-level abstractions such as compilation and QEC.

As we have seen above, the generally accepted target for the deployment of physical-layer quantum control is the reduction of error rates in individual quantum logic operations and devices. The error suppression afforded by quantum control is, however, complemented by error homogenization in *space* and *time*. In publicly available cloud devices, for instance, it is common to observe more than an order of magnitude deviation between best-case and worst-case qubit error rates across a device [36]. These can arise from fabrication variances as well as variations in coupling to the ambient electromagnetic environment. Likewise, cloud devices typically go out of calibration over a timescale that is typically much less than six hours, and device performance can vary substantially from day to day [36].

The use of appropriate robust-control solutions ensures end-users attain stable and repeatable algorithmic performance with minimal overhead. First, it minimizes hardware performance variations across a device, driving error rates towards the best-case performance, even in cases when the best case performance in a device is not improved (due *e.g.* to  $T_1$  limits). In addition, the same control solutions ensure that performance remains approximately constant throughout an inter-calibration window, rather than permitting performance to degrade near the end of the calibration cycle. Together, these benefits help to mitigate the need for complex error-aware compilation needed to route around poorly performing devices [36, 37]. See Sec. V A for a case-study demonstrating these benefits in real quantum computing hardware.

In the long-term these concepts also have critical impacts on the functioning of logical encoding for quantum error correction. To start, while not commonly expressed in this way, it becomes apparent that the entire concept of Quantum Error Correction can also be expressed as a form of feedback stabilization using a specialized and highly constrained sensor model. Thus importing insights from quantum control engineering can improve the practical implementation of quantum error correction.

At the interface of QEC and quantum firmware, error suppression has the potential to improve the efficiency of quantum error correction. The physics of both feedback stabilization and open-loop control at the physical layer exploit quantum coherence and spatio-temporal correlations in noise in order to offer robustness to quantum logic [38]. For instance, coherent averaging allows a net Unitary transformation to be performed with reduced sensitivity to error. Truly stochastic processes such as  $T_1$  energy relaxation are not typically correctable using these strategies. Immediately we see that physical-layer quantum control serves as a complement to higher-level logical encoding, maximally depressing hardware error

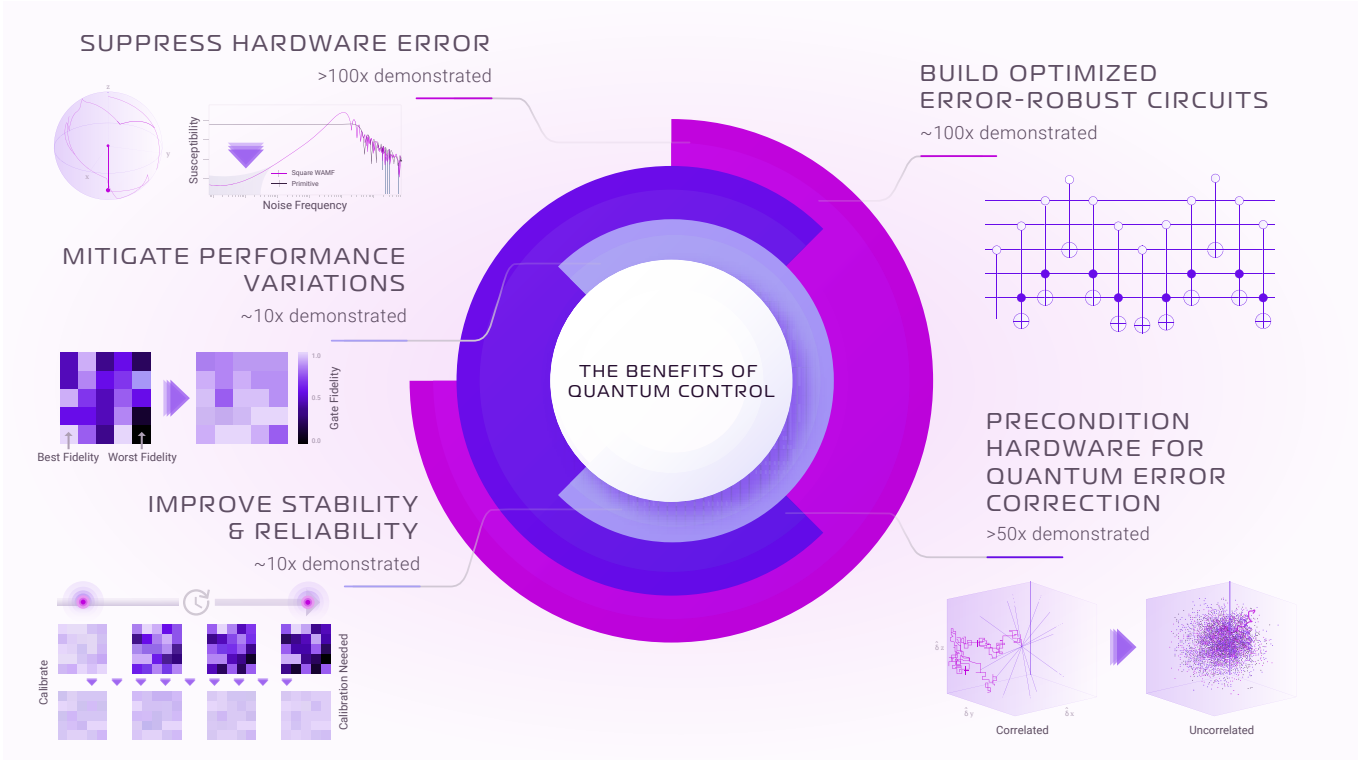


FIG. 2. The benefits of quantum control for quantum computing. Benefits ranging from  $10 \times - 100 \times$  improvement have been experimentally demonstrated. Technical details on these capabilities and associated experimental demonstrations are provided throughout this manuscript with a special focus on Sec. V.

rates to stochastic limits below fault-tolerant thresholds. QEC can then be deployed to identify and correct residual errors.

Next, the homogenization of error rates in space and time closes the gap between best and worst-case device performance, again ensuring fault-tolerant error rates are maintained across a logical block. Finally, the action of quantum control as a low-frequency *noise filter* reduces spatio-temporal correlations between residual errors [38], improving the resource-efficiency and efficacy of quantum error correction. This holds for both open-loop control (see Sec. IV B), and also closed-loop stabilization. In the latter, the innovations property [6] states that an ideal feedback loop extracts maximum information from the process being stabilized, leaving uncorrelated measurement-residuals; this has been experimentally demonstrated using trapped-ion qubits and a machine-learning-derived feedback correction [31]. Extracting all useful information from a correlated noise process ideally conditions errors for QEC [39].

### III. Q-CTRL PRODUCT ARCHITECTURE AND INTEGRATIONS

The Q-CTRL product suite is the first commercially available software specifically designed to improve

hardware performance in the quantum computing stack through access to quantum control. Q-CTRL tools incorporate the most advanced capabilities relevant to stabilizing quantum systems against hardware errors:

- Error-robust control selection, creation, and optimization for quantum logic, quantum circuits, and quantum algorithms
- Predictive error-budgeting and simulation of hardware and circuit performance in realistic laboratory environments
- Hardware characterization and calibration at the microscopic level to identify sources of noise and imperfection.

Q-CTRL delivers a comprehensive toolset via a modern cloud-compute architecture; unlike traditional software that takes the form of locally installed and executed code, Q-CTRL's cloud-based solutions enable customers to take advantage of extremely high performance with the flexibility to draw computational resources as needed. All tools are architected around an application programming interface (API), coded in Python. In certain circumstances we also employ special-purpose programming frameworks such as TensorFlow and Cython as appropriate in order to provide performance enhancements in the core codebase. Processing and memory resources used

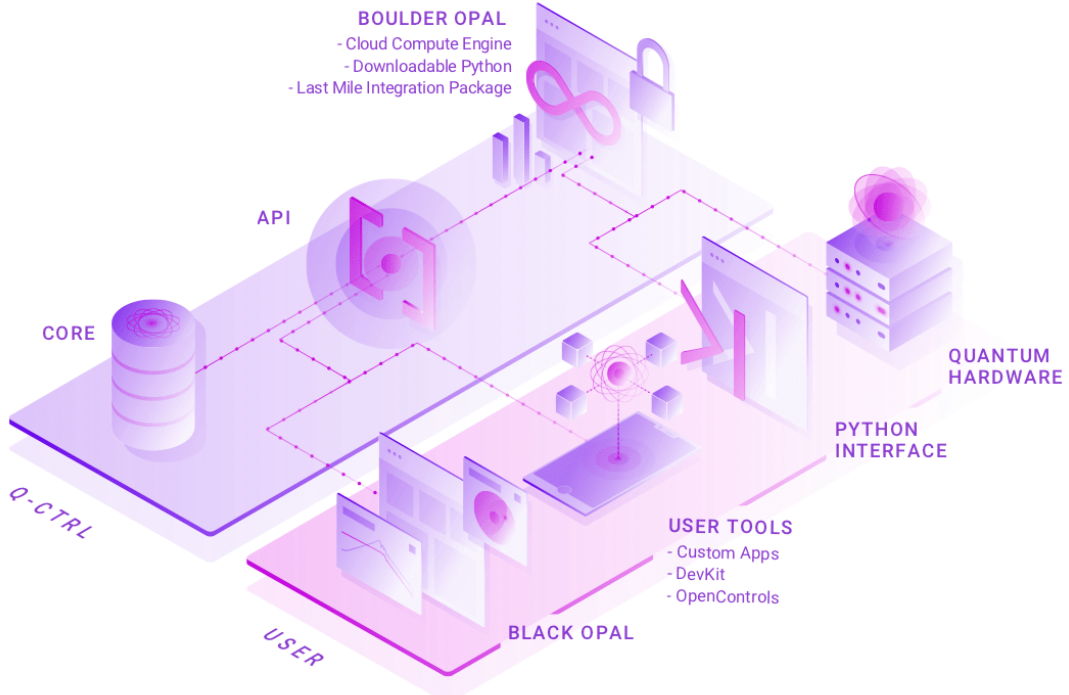


FIG. 3. Relationships between Q-CTRL products, connectivity via API to the core cloud-compute engine, and demonstration of various means of user interaction with Q-CTRL software. For instance, BOULDER OPAL is commonly accessed through a Python interface, or in combination with the last-mile-integration package may be built directly into user quantum hardware. Meanwhile core functionality may be accessed by users building custom tools via the Q-CTRL API.

in the execution of a computation are scaled automatically by the software, and specialized accelerators such as GPUs are accessed on demand for *e.g.* optimizations executed using our TensorFlow-based tools (see Sec. IV C). In addition users enjoy the benefits of access to new features as they become available—without the need to update software locally.

### A. Product overview

Here we describe the central software products designed by Q-CTRL, specifically BOULDER OPAL, BLACK OPAL, OpenControls, and the Q-CTRL Devkit, each of which delivers the capabilities and advantages of quantum control to users with different backgrounds, interests, and objectives. While our core focus is on the lowest level of the QC software stack, control provides benefits at higher levels as well (Fig. 1). These infrastructure-software tools, their relationship to each other, and the way users interact with them is represented in Fig. 3. A more detailed summary of features for individual products is provided in App. F.

*BOULDER OPAL* offers an advanced Python-based professional-grade toolkit for R&D teams to develop and deploy quantum control in their hardware or theoretical research. All technical features and core capabilities of

Q-CTRL products described in Sec. IV are accessible via BOULDER OPAL, making this the core toolkit in our offering. In order to facilitate integration into conventional programming environments, BOULDER OPAL includes a light Python package wrapper that is downloaded locally and orchestrates calls to the web API. All computationally intensive tasks remain the responsibility of the core computational engine in the cloud.

*BLACK OPAL* helps students, new users, and researchers to learn about quantum control by taking advantage of a graphical interface with interactive visualizations. It is designed to assist in building intuition for complex concepts in quantum control, such as the meaning of entanglement in quantum circuits (Fig. 4). The product is delivered as a web-based API service providing users with a graphical front-end interface complete with guided tours, configuration wizards, and integrated help; an example of an interactive visualization is shown in Fig. 4. The front-end prepopulates common system configurations for superconducting and trapped-ion processors, or custom configurations may be input, and contains predefined libraries of known control solutions. The functions selected for inclusion in the front-end interface are designed to assist in the process of learning about the role and capabilities of control, and to determine relevant control solutions for a given hardware problem.

*OpenControls* is an open-source Python package that

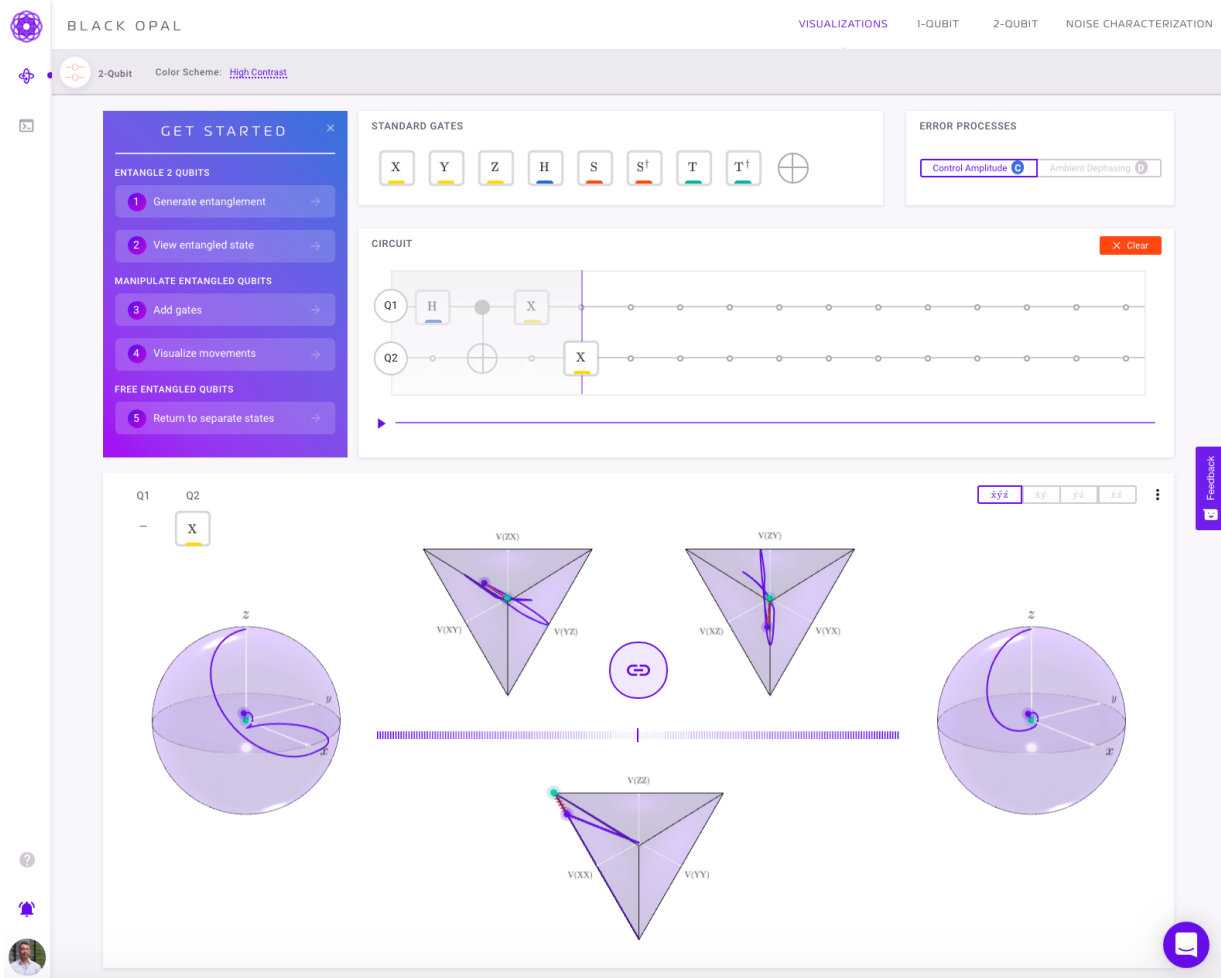


FIG. 4. Screenshot of BLACK OPAL interface demonstrating visualization of a circuit performed on two qubits. The trajectories of individual qubit observables depicting separable states are represented on an interactive 3D Bloch sphere. The bloch vector goes to zero as qubits become entangled through the action of the CNOT gate. Three interactive entanglement tetrahedra track correlations between the nine pairs of observables enabling visual representation of complete two-qubit state evolution. Details of the visualization packages within BLACK OPAL are presented in App. G.

includes established error-robust quantum control protocols from the open literature. The aim of the package is to be a comprehensive library of published and tested quantum control techniques developed by the community, with easy-to-use export functions allowing users to deploy these controls on custom quantum hardware, publicly available cloud quantum computers, or other parts of the Q-CTRL product suite.

The *Q-CTRL Devkit* allows quantum algorithm designers and end-users of quantum computers to derive enhanced performance for their applications. The Devkit enables developers to both analyze algorithmic performance in the presence of realistic time-varying noise, and to build in robustness through the structure of the compiled circuit. This toolkit is compatible with other compilers and can provide deterministic error robustness without the need for additional overhead such as repetition when adding engineered error in zero-noise

extrapolation schemes. Due to its cross-compatibility it can augment circuit performance when used in combination with higher-level circuit compilation or Pauli-frame randomization schemes. Because error robustness comes not only from circuit construction but also the specific timing of operations within a circuit, Devkit protocols must be used as the last stage of circuit compilation, following translation to hardware architectural constraints or circuit compression. See Sec. V E for an example case study.

## B. Cloud-compute architecture

These products and the back-end infrastructure supporting them encapsulate a fully-engineered, tested, and secured cloud-based platform for efficiently implementing the tasks set out in Sec. IV. Once the client has entered

relevant inputs, this information is sent to the back-end and processed through the API. The client’s data is taken through to the Python module, which performs the relevant computations and outputs objects based on the system inputs. The interface with the API varies based on the product in use as described below (Fig. 3), and even allows for custom application development by the user.

Our back-end software architecture employs established and lightweight web interfaces (OpenAPI specifications, REST APIs and JSON), as well as performant and scalable architectural designs such as a three-tiered application with dedicated worker pools and work queues. Q-CTRLs use of open standards enables our entire application stack to be deployed on any cloud—public, private, hybrid or on-premises—ensuring users are able to choose the right balance between price, performance and privacy. For instance, a remotely managed on-premises cloud instance can be provided to users seeking to maintain full control over all sensitive data, while still ensuring the advantages of a cloud-compute architecture.

Our choice of Python for the API incorporates simplicity, speed of development, and support for collaboration, *e.g.* with external developers. Both quantum scientists and programmers are typically familiar with Python, having used its libraries for tasks ranging from instrument control and advanced computation to web design. Building in Python also leverages compatibility with huge global resources of open-source code, and web-based frameworks like Django, bringing embedded security features to safeguard against attacks such as SQL injection, request forgery or cross-site scripting, crucially important for companies entrusting third parties with critical hardware tasks. Further technical details on the cloud-compute architecture are available in App. H.

### C. Quantum programming language integration via Python

A core mode of accessing Q-CTRL products comes from a lightweight Python wrapper or SDK which enables access to the API from within a standard Python interface. This approach brings the added advantage of compatibility with a wide variety of programming languages commonly employed in the quantum computing research community. As a complement, Q-CTRL provides Python adaptors for all open-source Python-based quantum computing languages, allowing integration of advanced control solutions into conventional programming workflows and execution on cloud hardware platforms.

The *qctrl-qiskit* package provides export functions of Q-CTRL-derived control solutions or protocols to qiskit. Q-CTRL dynamical decoupling sequences (used for implementing the identity operator in preservation of quantum memory) can be converted into qiskit quantum circuits using these methods, accounting for approximations

made in qiskit circuit compilation and ensuring circuits are not compactified in such a way that undermines performance. Furthermore, Q-CTRL pulses can be exported from both BLACK OPAL and BOULDER OPAL in the OpenPulse format [40] which provides analog-level programming of microwave operations performed on hardware. As a complement, Q-CTRL has also developed calibration routines for IBM hardware to account for the truly open nature of the OpenPulse API. Such appropriately formatted controls and calibration routines can then be immediately run on IBM’s quantum computing hardware with an IBM Q account.

The *qctrl-pyquil* package provides export functions to Rigetti’s pyQuil, and *qctrl-cirq* allows export to Google Cirq. At present, the absence of analog-level control access limits export functionality to timed sequences of standard control operations handled natively in these platforms. In both cases the translation layer ensures that the integrity of the sequence structure and timing is preserved within approximations made in sequencing in these two languages. pyQuil integration currently permits the execution of Q-CTRL sequences using Rigetti’s Quantum Cloud Service on real quantum hardware.

### D. Quantum computer hardware integration

Q-CTRL products have been designed to integrate with a wide variety of hardware systems—from local laboratory-based quantum hardware to quantum-compute cloud engines. This requires an architecture which is flexible and platform agnostic, and also mandates compatibility and integrability with various hardware and software packages.

The Last-Mile Integration (LMI) toolset integrates the full suite of Q-CTRL cloud-based products with a user’s existing experimental hardware control system and software stack. The LMI is delivered via a customized, local-instance Python package that runs in parallel with the user’s experimental control stack to automate and schedule key tasks in control definition, calibration, and optimization. A schematic overview of the relationship between BOULDER OPAL, the Last-Mile Integration Package, and the experimental hardware/software stack is presented in Fig. 5.

Hardware integration is most tightly coupled to the determination of appropriate outputs from hardware signal generators such as arbitrary waveform generators, direct digital synthesizers, and vector signal generators. In the LMI package, all controls are written in a format tailored to hardware constraints such as sample rates, amplitude resolution, and data formats. Custom control pulses are exported into a format (*e.g.* CSV or JSON [40]) easily read by the experimental control stack. Q-CTRL has already partnered with a number of original equipment manufacturers serving the quantum-computing market, providing pre-built formatting scripts to translate control output into machine-compatible formats.

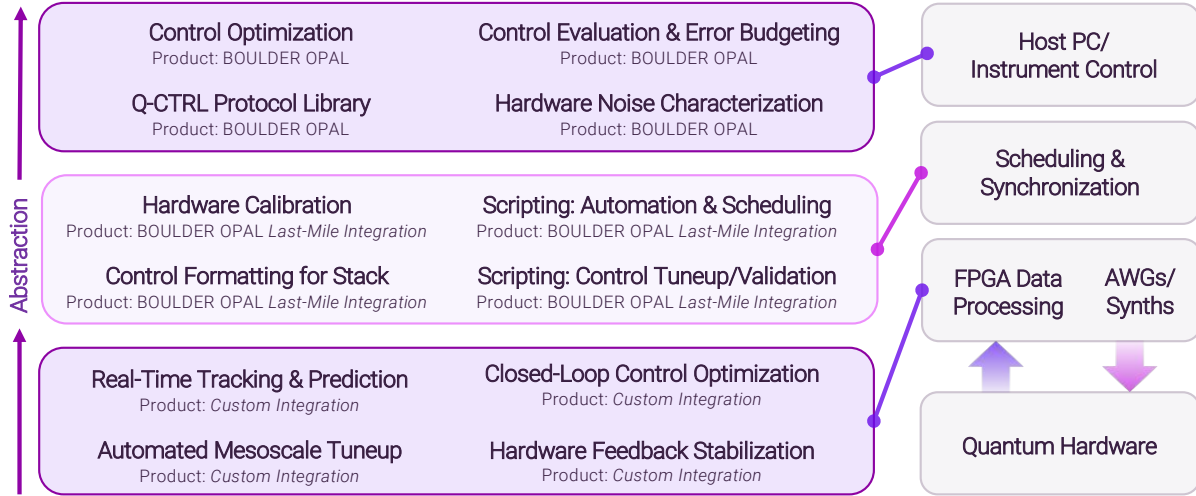


FIG. 5. Schematic overview of quantum control functions, accessibility via Q-CTRL products, and integration into a user's custom classical experimental control hardware. As tasks are abstracted further away from the details of experimental hardware, the point of integration similarly rises in the experimental control stack.

As an example, Q-CTRL has partnered with Quantum Machines, providing a direct interface between Q-CTRL protocols and QM's Quantum Orchestration Platform stack. The Quantum Orchestration Platform is a software-hardware solution whose software interface is Quantum Machines programming language called "QUA", and an advanced hardware system allowing orchestration of QUA programs in real-time (*e.g.* waveform generation, waveform acquisition, classical data processing and real-time control-flow). This integration naturally permits control formatting matched to QUA, but also exploits parametric encoding to enable rapid hardware tuneup and calibration. For instance, by parameterizing the duration of an experiment or a DDS phase value it becomes trivial to calibrate control amplitudes and phases. Similarly, scripting in QUA allows exploitation of low-latency FPGA-based computation for the execution of real-time machine-learning routines or Bayesian updates via tools offered jointly by Q-CTRL and QM. Using this framework we have recently demonstrated dephasing-robust single-qubit operations in a tuneable transmon device, indicating that the combination of Q-CTRL software with the Quantum Machines quantum orchestration platform stack permits faithful output of complex modulated control protocols. Beyond official Q-CTRL partners, custom scripts cover commonly encountered hardware solutions, leveraging the flexibility of Python programming.

An essential aspect of this integration is efficient hardware calibration permitting determination of the analog voltages or digital commands required to achieve output signals with appropriate phase and amplitude values. This helps account not only for residual amplitude modulation in the presence of other forms of modulation (*e.g.* PM), but also cross-coupling and signal distortions

encountered due to room-temperature hardware such as mixers. The LMI allows efficient tuneup of control hardware and produces a local lookup table allowing rapid translation of target phase and amplitude values for an optimized control to control-hardware instructions.

Hardware calibration can also leverage quantum control in order to gain access to information about signal distortions and transmission-line nonlinearities within experimental systems that are not easily characterized through conventional means. This approach is widely employed in most laboratories through basic protocols for qubit frequency determination such as Ramsey spectroscopy, drive-amplitude calibration through Rabi measurements, and more advanced protocols to estimate microwave phases [41] or identify quadrature cross-couplings [42, 43]. Further, we offer time-domain impulse response characterization [44] in order to determine the nonlinear response of transmission lines and passive elements in the signal propagation pathway.

In addition to characterization of classical hardware, the LMI package maximizes automation via a suite of automated Python scripts for the efficient tuneup of qubit hardware. These scripts permit extraction of standard parameters ( $T_1$ ,  $T_{1\rho}$ ,  $T_2$ ,  $T_2^{(\text{echo})}$ ,  $\Omega^{(\text{Rabi})}$ ) as well as calibration of key parameters relevant to high-fidelity control implementation. The package permits scheduled noise sensing and reconstruction in order to detect changes in dominant noise power spectra (*e.g.* control noise or dephasing). Again, all computationally intensive calculations are handled by the distributed cloud-compute engine with only scripting and experimental-control-software integration handled locally. Experimental calibration and noise characterization results are also logged on the cloud server and accessible to users.

Moving further down the experimental control hard-

ware stack it becomes possible to implement a variety of low-latency real-time processing tasks via custom hardware integration. Capabilities are based on core routines and techniques developed by Q-CTRL and customized for a user's or vendor's hardware system (*e.g.* QUA development with Quantum Machines). An example is closed-loop optimization of control solutions in order to reoptimize error-robust controls as system noise sources drift. Numerically optimized controls may be used as a seed for optimization based on experimental measurements based on user-defined cost functions such as randomized benchmarking survival probabilities.

#### IV. TECHNICAL FUNCTIONALITY OVERVIEW

In this section we provide an overview of key technical capabilities afforded by quantum control as accessed through the products introduced in [Sec. III](#). Our presentation focuses on tasks relevant to building error robustness into quantum computer hardware, though many other applications exist in quantum sensing, data fusion, and advanced medical imaging. In [Sec. V](#) we provide detailed case studies to illustrate how these features are employed in real research settings.

##### A. General quantum-control setting

Here we establish the general control-theoretic setting for both the optimal and robust optimization of control solutions in multi-dimensional quantum systems. We write the total Hamiltonian as the sum of dynamical contributions from both control and noise interactions

$$H_{\text{tot}}(t) = H_{\text{ctrl}}(t) + H_{\text{err}}(t). \quad (1)$$

We assume that  $H_{\text{ctrl}}(t)$  is a deterministic component of  $H_{\text{tot}}(t)$  containing both an intrinsic *drift* term (*e.g.* the frequencies of the qubits) and *controllable* parts of the system (*e.g.* microwave *drives* or clock *shifts*). See [App. B](#) for generalized definitions of these terms. The error Hamiltonian  $H_{\text{err}}(t)$  captures the influence of noise, is assumed to be small, and may also be a function of control Hamiltonian  $H_{\text{ctrl}}(t)$ . The typical control problem may be split into two distinct tasks:

1. Design a control solution for a  $D$ -dimensional Hilbert space such that  $H_{\text{ctrl}}(t)$  implements a target unitary  $U_{\text{target}}$  at time  $\tau$ .
2. Design a control solution such that  $H_{\text{ctrl}}(t)$  is *robust* against noise interactions  $H_{\text{err}}(t)$  over duration  $[0, \tau]$ .

The first task is typically referred to as an *optimal* control problem while the second is called *robust* control; Q-CTRL provides tools for both.

##### 1. Optimal quantum control

The *optimal* control setting reduces the following problem. Given the Schrödinger equation

$$i\dot{U}_{\text{ctrl}}(t) = H_{\text{ctrl}}(t)U_{\text{ctrl}}(t) \quad (2)$$

the aim is to find  $H_{\text{ctrl}}(t)$  such that

$$U_{\text{target}} = U_{\text{ctrl}}(\tau) \quad (3)$$

where  $U_{\text{ctrl}}(\tau)$  is the evolved unitary at time  $\tau$  and  $U_{\text{target}}$  is the target operation. This control problem, generally, can be considered a bilinear control problem as the controllable element of the equation of motion ( $H_{\text{ctrl}}(t)$ ) linearly *multiples* the state. This is in contrast to the much more common linear control problems from classical control where the controllable element is linearly *added* to the state. Bilinear control problems typically do not have analytically tractable solutions, and instead must be solved numerically.

We define a measure of optimal control using a Frobenius inner product [Eq. \(A3\)](#) to evaluate the operator-distance between  $U_{\text{ctrl}}(\tau)$  and  $U_{\text{target}}$ . Specifically

$$\mathcal{F}_{\text{optimal}}(\tau) = \left| \frac{1}{D} \left\langle U_{\text{target}}, U_{\text{ctrl}}(\tau) \right\rangle_F \right|^2. \quad (4)$$

This measure is bounded between  $[0, 1]$ , with perfect implementation of the target [Eq. \(3\)](#) corresponding to  $\mathcal{F}_{\text{optimal}}(\tau) = 1$ . We define a corresponding infidelity measure as

$$\mathcal{I}_{\text{optimal}}(\tau) = 1 - \mathcal{F}_{\text{optimal}}(\tau). \quad (5)$$

A simple modification of this fidelity measure enables the optimal condition to be evaluated on a subspace of interest. Specifically

$$\mathcal{F}_{\text{optimal}}^P(\tau) = \left| \frac{1}{\text{Tr}(P)} \left\langle PU_{\text{target}}, U_{\text{ctrl}}(\tau) \right\rangle_F \right|^2 \quad (6)$$

where  $P$  defines a projection matrix, enabling optimal control to be evaluated on a target subspace. Similarly, achieving high-fidelity state-transfer  $|\psi_{\text{initial}}\rangle \rightarrow |\psi_{\text{final}}\rangle$  is equivalent to maximizing the state fidelity defined as

$$\mathcal{F}_{\text{optimal}}^\psi(\tau) = |\langle \psi_{\text{initial}} | U_{\text{ctrl}}(\tau) | \psi_{\text{final}} \rangle|. \quad (7)$$

As discussed in detail in [Sec. IV C](#), crafting numeric solutions for these control problems may be conveniently cast as cost-minimization; we provide specific numeric tools addressing this challenge. These measures strictly describe whether the ideal Hamiltonian  $H_{\text{ctrl}}$  implements the target evolution. They do not incorporate errors arising from stochastic noise processes. This is the subject of robust control, described below.

## 2. Robust quantum control

The *robust* control setting presents the multi-objective problem of achieving both tasks 1 and 2. In this case we consider the stochastic evolution of the total Hamiltonian  $H_{\text{tot}}(t)$

$$i\dot{U}_{\text{tot}}(t) = H_{\text{tot}}(t)U_{\text{tot}}(t) \quad (8)$$

$$(9)$$

Noisy dynamics contributed by  $H_{\text{err}}(t)$ , therefore distort the final operation  $U_{\text{tot}}(\tau)$  away from the ideal  $U_{\text{ctrl}}(\tau)$ . This effect may be isolated by expressing the total propagator as

$$\tilde{U}_{\text{err}}(\tau) = U_{\text{tot}}(\tau)U_{\text{ctrl}}(\tau)^{\dagger}. \quad (10)$$

The residual operator  $\tilde{U}_{\text{err}}(\tau)$  defined in Eq. (10) is referred to as the *error action operator*. This unitary satisfies the Schrödinger equation in an interaction picture co-rotating with the control, which we call the *control frame*. Specifically,

$$\tilde{U}_{\text{err}}(\tau) = \mathcal{T} \exp \left[ -i \int_0^{\tau} \tilde{H}_{\text{err}}(t) dt \right] \quad (11)$$

where  $\mathcal{T}$  is the time-ordering operator, and

$$\tilde{H}_{\text{err}}(t) \equiv U_{\text{ctrl}}(t)^{\dagger} H_{\text{err}}(t) U_{\text{ctrl}}(t) \quad (12)$$

defines the *control-frame Hamiltonian*. An analogous concept originally appeared in average Hamiltonian theory developed for NMR [45], but was called a *toggling frame* in that context because it considered only instantaneous operations.

Using the definition of  $\tilde{U}_{\text{err}}(\tau)$  in Eq. (10), the robust control problem may be formalized in terms of the dual conditions

$$U_{\text{target}} = U_{\text{ctrl}} \quad (13)$$

$$\tilde{U}_{\text{err}} = \mathbb{I} \quad (14)$$

where  $\mathbb{I}$  is the identity operation on the control system. The *robust* control problem therefore consists of augmenting the *optimal* control problem with the additional condition Eq. (14), describing how susceptible the system is to noise interactions under a given control Hamiltonian. We define the corresponding measure

$$\mathcal{F}_{\text{robust}}(\tau) = \left\langle \left| \frac{1}{D} \langle \tilde{U}_{\text{err}}(\tau), \mathbb{I} \rangle_F \right|^2 \right\rangle, \quad (15)$$

where the angle brackets  $\langle \cdot \rangle$  denote an ensemble average over realizations of the noise processes, and  $\langle \cdot, \cdot \rangle_F$  denotes a Frobenius inner product Eq. (A3). Robustness is therefore evaluated as the noise-averaged operator distance between the error action operator Eq. (10) and the identity. This measure is bounded between  $[0, 1]$ , with the robustness condition Eq. (14) perfect implemented

when  $\mathcal{F}_{\text{robust}}(\tau) = 1$ . We define a corresponding infidelity measure as

$$\mathcal{I}_{\text{robust}}(\tau) = 1 - \mathcal{F}_{\text{robust}}(\tau) \quad (16)$$

As above, a simple modification of this measure enables the robustness condition to be evaluated on a subspace of interest. Specifically

$$\mathcal{F}_{\text{robust}}^P(\tau) = \left\langle \left| \frac{1}{\text{Tr}(P)} \langle P \tilde{U}_{\text{err}}(\tau), \mathbb{I} \rangle_F \right|^2 \right\rangle \quad (17)$$

where  $P$  defines a projection matrix, enabling robust control to be evaluated on a target subspace. And again, finding a robust control for a state transfer problem may be expressed

$$\mathcal{F}_{\text{robust}}^{\psi}(\tau) = \langle \langle \psi_{\text{initial}} | \tilde{U}_{\text{err}} | \psi_{\text{initial}} \rangle \rangle. \quad (18)$$

Note Eq. (15) does not include any information about whether  $U_{\text{ctrl}}(\tau)$  implements a *particular* target gate  $U_{\text{target}}$ . In this sense, the robustness criterion is target-independent. Once again, solving these conditions requires a numerical approach subject to a multiobjective optimization routine. In practice, with sufficient control, it is always possible to satisfy both of these conditions and find a *robust* control that achieves the desired target operation with high fidelity. We tackle this problem using a number of novel approaches developed in Sec. V B, and demonstrated in real case studies in Sec. IVC.

## B. Performance evaluation for arbitrary controls

The evaluation of any measure for the fidelity of a robust-control operation as in Eq. (15) requires the computation of Eq. (11), which is generally challenging as control and noise Hamiltonians need not commute at different times. Characterizing control robustness and performance in realistic laboratory settings—especially for operations performed within large interacting systems—therefore requires simple, easily computed heuristics that aid a user in gaining intuition into control performance.

Here we introduce generalized multi-dimensional filter functions which serve as an engineering-inspired heuristic to determine noise susceptibility for arbitrary unitaries within high-dimensional Hilbert spaces. These objects express the noise-admittance of a control as a function of noise frequency, and reduce control selection to the examination of an easily visualized object similar to the Bode plot in classical engineering. Noise may be considered over a wide range of parameter regimes, from quasistatic (noise slow compared to  $H_{\text{ctrl}}(t)$ ) to the limit in which the noise fluctuates on timescales comparable to or faster than  $H_{\text{ctrl}}(t)$ . We build on past single-qubit studies [16, 17, 46–48], assuming quasi-classical noise channels, to produce an explicit *basis independent* computational form incorporating all leading-order filter functions and extensible to higher-dimensional quantum systems [49] with enhanced computational efficiency.

### 1. Modelling noise and error in D-dimensional systems

The error action operator  $\tilde{U}_{\text{err}}(\tau)$  for non-dissipative system-bath dynamics is treated as the unitary generated by an effective Hamiltonian  $H^{(\text{eff})} = \Phi(\tau)/\tau$ , such that

$$\tilde{U}_{\text{err}}(\tau) \equiv e^{-i\Phi(\tau)}, \quad \Phi(\tau) \equiv \sum_{\alpha=1}^{\infty} \Phi_{\alpha}(\tau). \quad (19)$$

We obtain an arbitrarily accurate approximation for the unitary evolution using a Magnus series expansion [50, 51], where the  $\alpha$ th Magnus term,  $\Phi_{\alpha}(\tau)$ , is computed as the sum of time-ordered integrals over permutations of  $\alpha$ th-order nested commutators of  $\tilde{H}_{\text{err}}(t_j)$ , for  $j \in \{1, \dots, \alpha\}$  (see App. C 1).

Consider an arbitrary  $D$ -dimensional quantum system defined on the Hilbert space  $\mathcal{H}$ , and let the total control Hamiltonian in Eq. (1) have control and error terms of the form

$$H_{\text{ctrl}}(t) = \sum_{j=1}^n \alpha_j(t) C_j, \quad (20)$$

$$H_{\text{err}}(t) = \sum_{k=1}^p \beta_k(t) N_k(t). \quad (21)$$

The control Hamiltonian,  $H_{\text{ctrl}}(t)$ , captures a target evolution generated by  $n$  participating control operators,  $C_j \in \mathcal{H}$ . The noise Hamiltonian,  $H_{\text{err}}(t)$ , captures interactions with  $p$  independent noise channels. Distortions in the target evolution are generated by the noise operators  $N_k(t) \in \mathcal{H}$ , formally time-dependent such that  $N_k(t) = 0$  for  $t \notin [0, \tau]$ . The noise fields  $\beta_k(t)$  are assumed to be a classical zero-mean wide-sense stationary processes with associated noise power spectral densities  $S_k(\omega)$ . The toggling-frame [16, 49] Hamiltonian takes the form

$$\tilde{H}_{\text{err}}(t) = \sum_{k=1}^p \beta_k(t) \tilde{N}_k(t) \quad (22)$$

where

$$\tilde{N}_k(t) \equiv U_{\text{ctrl}}^{\dagger}(t) N_k(t) U_{\text{ctrl}}(t) \quad (23)$$

defines the noise operators in this toggling-frame. Using a Magnus expansion as in Eq. (19), the noise action operator may then be approximated to the desired order.

For the purpose of calculating the error action operator Eq. (11) we are free to choose any gauge transformation of the form  $\tilde{H}'_{\text{err}} = \tilde{H}_{\text{err}} + g\mathbb{I}$  which, up to a global phase, leaves the the dynamical evolution unchanged. With this freedom it is convenient to define the transformed Hamiltonian with the property that  $\text{Tr}(P\tilde{H}'_{\text{err}}) = 0$ , namely tracelessness on the subspace associated with the projection matrix  $P$ , by choosing  $g = -\text{Tr}(P\tilde{H}_{\text{err}})/\text{Tr}(P)$ . From Eq. (22), using the linearity of the trace and observing the noise variables  $\beta_k(t)$

are scalar-valued for classical noise, we obtain

$$\tilde{H}'_{\text{err}}(t) = \sum_{k=1}^p \beta_k(t) \tilde{N}'_k(t) \quad (24)$$

where we define the *traceless* noise operators in the toggling frame as

$$\tilde{N}'_k(t) \equiv \tilde{N}_k(t) - \frac{\text{Tr}(P\tilde{N}_k(t))}{\text{Tr}(P)} \mathbb{I}. \quad (25)$$

Assuming the noise fields  $\beta_k(t)$  are sufficiently weak, we truncate the Magnus expansion Eq. (19) at leading order and approximate the error action operator as

$$\tilde{U}_{\text{err}}(\tau) \approx \exp[-i\Phi_1(\tau)]. \quad (26)$$

Substituting into Eq. (17) the leading-order infidelity measure for robust control is approximated as

$$\mathcal{I}_{\text{robust}}(\tau) \approx \frac{1}{\text{Tr}(P)} \text{Tr} \left( P \left\langle \Phi_1(\tau) \Phi_1^{\dagger}(\tau) \right\rangle \right). \quad (27)$$

To obtain this expression we perform a Taylor expansion on Eq. (26), retain terms consistent with the leading-order approximation, and use the inherited property from Eq. (25) that  $\text{Tr}(P\Phi_1) = 0$  (see App. C 3).

To compute the first order Magnus term we substitute Eq. (24) into Eq. (C1), yielding

$$\Phi_1(\tau) = \sum_{k=1}^p \int_{-\infty}^{\infty} dt \beta_k(t) \tilde{N}'_k(t) \quad (28)$$

where we formally extend the limits of integration to  $\pm\infty$ , noting that  $N'_k(t) = 0$  for  $t \notin [0, \tau]$ .

### 2. Multi-dimensional filter functions in the frequency domain

In order to efficiently compute Magnus contributions to the infidelity we move to the Fourier domain, and re-express contributions to error in a D-dimensional system

$$\Phi_1(\tau) = \sum_{k=1}^p \int_{-\infty}^{\infty} \frac{d\omega}{2\pi} G_k(\omega) \beta_k(\omega) \quad (29)$$

where the Fourier-domain functions

$$G_k(\omega) \equiv \mathcal{F} \{ N'_k(t) \} (-\omega) \quad (30)$$

$$\beta_k(\omega) \equiv \mathcal{F} \{ \beta_k(t) \} (\omega) \quad (31)$$

are defined according to the conventions set out in App. A 1.

Substituting Eq. (29) into Eq. (27) then yields a compact expression for the leading-order robustness infidelity in the frequency-domain

$$\mathcal{I}_{\text{robust}}(\tau) \approx \frac{1}{2\pi} \sum_{k=1}^p \int_{-\infty}^{\infty} d\omega F_k(\omega) S_k(\omega) \quad (32)$$

Here, each noise channel  $k$  contributes a term computed as an overlap integral between the noise power spectrum  $S_k(\omega)$  and a corresponding filter function,  $F_k(\omega)$ . An approximation to the inclusion of higher-order Magnus terms for the infidelity may be obtained by exponentiating this expression, due to the similarity of the power-series expansion for an exponential function and the structure of the Magnus series [17].

The critical element for capturing the action of the control is the filter function,  $F_k(\omega)$ , relative to the  $k$ th noise channel. The explicit form of the filter function with respect to the projection matrix  $P$  is defined (see App. C 4 for details) as

$$F_k(\omega) = \frac{1}{\text{Tr}(P)} \text{Tr} \left( PG_k(\omega) G_k^\dagger(\omega) \right). \quad (33)$$

This expression may be simply recast in a form that is easily computed numerically, an essential task in software implementations. Let  $p_l$  be the  $l$ th diagonal element of

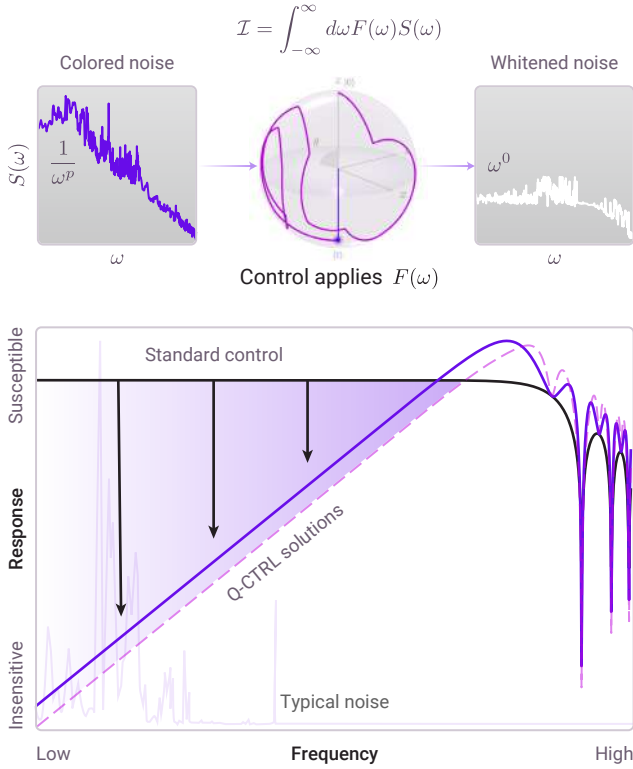


FIG. 6. Overview of the action of control as a noise filter at the operator level. Upper: An example of how colored noise enters expressions for the infidelity of a control operation as the overlap integral of the noise power spectrum and filter function for the control. A colored spectrum is thus whitened by the control through the physics of coherent averaging. Lower: Example filter function for an appropriately constructed noise-suppressing/filtering control. Such filters are low-frequency-noise suppressing; by reducing the filter function magnitude in a spectral range where the noise power spectrum is large, the fidelity of the operation is improved.

$P$ , then the filter function may be expressed

$$F_k(\omega) = \frac{1}{\text{Tr}(P)} \sum_{l=1}^D p_l \sum_{q=1}^D \left| \left\{ G_k(\omega) \right\}_{lq} \right|^2. \quad (34)$$

That is, take the Fourier transform of each matrix element of the time-dependent operator  $\tilde{N}'_k(t)$ , sum the complex modulus square of every element, weighted by the diagonal elements  $p_l$ , and divide through by  $\text{Tr}(P)$ , the dimension of the quantum system subspace. With this computationally simple definition, we enable the efficient calculation of filter functions for single and multi-qubit gates, arbitrary high-dimensional systems, and complete circuits composed of multiple qubits and many operations. Thus we have a new computational device allowing the calculation of noise susceptibility for a wide range of elements relevant to quantum computation.

Given a noise power spectral density which represents realistic time-varying noise for a target noise operator (e.g. dephasing  $\propto \sigma_z$ ), one may use the filter function to simply estimate operational fidelity; the net fidelity is given by the overlap integral of these two quantities as a function of frequency (Fig. 6). A high-fidelity control will minimize the filter function's spectral weight in frequency ranges where the noise power spectral density for a particular error channel is large. The predictive capabilities of this technique to control performance evaluation are experimentally validated for both single-qubit operations [17] and higher-dimensional systems (e.g. Molmer Sorensen gates [52]). An example of the predictive power of the filter function is presented in Fig. 10d-e for a variety of single-qubit controls.

### C. Optimization tools to maximize control performance

Precise manipulation of quantum systems via shaped control pulses has emerged as a key area of development for quantum physics and chemistry. In near-term quantum computers, for example, substitution of primitive operations with optimized noise-robust controls can yield improved fidelities for single- and multi-qubit gates without hardware modification, and offers a range of additional benefits, generally also providing reduced overhead in operation time. As discussed in Sec. IV A, for all but the simplest systems identifying such controls is analytically intractable, and adapting these methods to higher-dimensional systems relies on powerful numerical optimization techniques.

Q-CTRL has developed a versatile optimization engine based on a GPU-compatible graph architecture, and leveraging where appropriate the efficient computational heuristics introduced in Sec. IV B. This engine is purpose-built for rapidly creating high-fidelity controls spanning both *optimal* and *robust control* in high-dimensional Hilbert spaces. Creation of an optimized control solution may be undertaken for individual gates,

small interacting subcircuits, or complete algorithms. All such circumstances are efficiently incorporated using the system definition introduced above without the need for a change in the underlying toolkit. Following system and target unitary definition, control optimization effectively requires only a single command.

A technical description of the essential framework is presented below, covering the core optimization engine, parameterization of control variables, definition of cost functions, and incorporation of constraints. In Sec. V we demonstrate these capabilities using higher-dimensional superconducting systems as important case studies.

### 1. Optimizer framework

Mathematically we define the optimization problem as follows. Let  $C(\mathbf{v})$  denote the cost function for optimization, where  $\mathbf{v} = (v_1, v_2, \dots)$  denotes an array of generalized control variables parameterizing the control Hamiltonian  $H_{\text{ctrl}}(\mathbf{v})$ . The evolved unitary after time  $\tau$  is therefore parameterized as  $U_{\text{ctrl}}(\mathbf{v}, \tau)$ , and the cost function obeys the functional dependency  $C(\mathbf{v}) = C(U_{\text{ctrl}}(\mathbf{v}, \tau))$ . To benefit from gradient ascent methods it is necessary to calculate all partial derivatives of the gradient function

$$\vec{\nabla}_{\mathbf{v}} C = \left( \frac{\partial C}{\partial v_1}, \frac{\partial C}{\partial v_2}, \dots \right). \quad (35)$$

In general this is a complex computation requiring many applications of the chain rule, and depends on the specific form of the cost function. These challenges are, however, naturally overcome using TensorFlow as the optimizer framework. This benefits from an in-built gradient calculator based on the underlying tensor map, and machine-learning algorithms for minimizing the cost-function. Moreover, TensorFlow permits the calculation of nonlinear gradients, which is particularly relevant in circumstances such as the parametrically driven gate for interacting transmons where there the modulation applied to a signal generator in the lab frame produces an effective operator experienced by the quantum system transformed by a Bessel function. We offer various methods for performing the optimization in order to meet system constraints, including optimization over the piecewise-constant control segments defined below, Runge-Kutta optimization, and CRAB optimization [53] (see Sec. IVC2 for further information).

In order to perform the optimization, the specific control parameterization and cost functions must be defined. As described in App. B3 the composition of the control Hamiltonian is formalized in terms of drive and shift control pulses. For efficient optimizations, control pulses are typically parameterized as piecewise-constant functions divided into  $m$  segments of uniform duration

$$\tau_i = \tau/m, \quad i \in \{1, \dots, m\}. \quad (36)$$

In this case the full control operation is determined by specifying only the segment magnitudes on each of the  $m$

Opt. Type	$C_\mu(\mathbf{v})$ : functional form	Description
Optimal	$\mathcal{I}_{\text{optimal}}$	Noise-free target unitary over $D$ -dimensions
Robust	$\frac{1}{2\pi} F_k(0)$	Quasi-static noise/constant-offset
Robust	$\frac{1}{2\pi} F_k(\omega)$	Fixed frequency noise suppression at $\omega$
Robust	$\int_{\omega_1}^{\omega_2} S_k(\omega) F_k(\omega) \frac{d\omega}{2\pi}$	Broadband noise suppression over $[\omega_1, \omega_2]$

TABLE I. Component cost functions to be included as desired in Eq. (45) for an optimization task. Here  $F_k(\omega)$  and  $S_k(\omega)$  are the filter function and noise power spectral density respectively, associated with the  $k$ th noise channel.

segments. For a system accommodating  $d$  drive pulses, and  $s$  shift pulses, we define vector arrays

$$\boldsymbol{\Omega}_j = [\Omega_{1,j}, \Omega_{2,j}, \dots, \Omega_{m,j}], \quad j \in \{1, \dots, d\} \quad (37)$$

$$\boldsymbol{\phi}_j = [\phi_{1,j}, \phi_{2,j}, \dots, \phi_{m,j}], \quad j \in \{1, \dots, d\} \quad (38)$$

$$\boldsymbol{\alpha}_l = [\alpha_{1,l}, \alpha_{2,l}, \dots, \alpha_{m,l}], \quad l \in \{1, \dots, s\} \quad (39)$$

where  $\Omega_{i,j}$  and  $\phi_{i,j}$  are the modulus and phase of the  $j$ th drive pulse, and  $\alpha_{i,l}$  is the amplitude of the  $l$ th shift pulse, on the  $i$ th segment. For efficient optimization it is convenient to work with normalized, non-dimensional variables. We therefore define

$$\boldsymbol{\Omega}'_j \equiv \boldsymbol{\Omega}_j / \Omega_{\text{max},j} \quad j \in \{1, \dots, d\} \quad (40)$$

$$\boldsymbol{\phi}'_j \equiv (\phi_j / \pi + 1) / 2 \quad j \in \{1, \dots, d\} \quad (41)$$

$$\boldsymbol{\alpha}'_l \equiv (\alpha_l / \alpha_{\text{max},l} + 1) / 2 \quad l \in \{1, \dots, s\} \quad (42)$$

where  $\Omega_{\text{max},j}$  and  $\alpha_{\text{max},l}$  are the upper bounds permitted for the  $j$ th drive modulus and  $l$ th shift amplitude respectively. These transformed variables satisfy

$$v \in [0, 1], \quad \forall v \in \{\Omega'_i, \phi'_i, \alpha'_i\}, \quad (43) \\ j \in \{1, \dots, d\}, \quad l \in \{1, \dots, s\}, \quad i \in \{1, \dots, m\}.$$

With these definitions, we compactly express the full array of variables in the  $(2d + s)m$ -length vector of generalized control variables

$$\mathbf{v} = [\boldsymbol{\Omega}'_1, \dots, \boldsymbol{\Omega}'_d, \boldsymbol{\phi}'_1, \dots, \boldsymbol{\phi}'_d, \boldsymbol{\alpha}'_1, \dots, \boldsymbol{\alpha}'_s]. \quad (44)$$

For a given total duration  $\tau$ , the control Hamiltonian is therefore functionally expressed as  $H_{\text{ctrl}}(\mathbf{v})$ , and optimization tasks are implemented on the search space spanned by  $\mathbf{v}$ .

## 2. Constrained Optimizations

In general an unbounded optimization can lead to either unphysical or impractical control solutions. Limiting the search space via implementation of appropriately constructed constraints can assist in ensuring that controls meet hardware limitations, and also dramatically improve the general efficiency of the optimization problem. To generate optimized controls subject to multiple competing constraints, we generalize the cost function as a linear combination

$$C(\mathbf{v}) = \sum_{\mu} w_{\mu} C_{\mu}(\mathbf{v}) \quad (45)$$

where each component  $C_{\mu}(\mathbf{v})$  measures a distinct aspects of the target performance as a function of the generalized control variables  $\mathbf{v}$  defined in Eq. (44), and the constants  $w_{\mu}$  weight the relative importance of these contributions in the optimized result. The optimizer iteratively searches over suitably represented control parameters  $\mathbf{v}$  in order to minimize the cost function defined above. The functional forms of some important cost function components are outlined in Table I.

This framework allows physically motivated constraints to be incorporated into the optimization problem which dramatically expands the range of problems which can be addressed. In particular we have focused on meeting the demands imposed by physical hardware limitations, as detailed in Table II.

One of the most important constraints to be considered is smoothing of pulse waveforms to accommodate bandwidth limits and finite response times from hardware. In general smoothed solutions can be achieved by increasing the segment number in an optimization, constraining the effective time-derivative (bounding the magnitude of the control's changes between segments), or ensuring that all optimized waveforms include linear-time-invariant filters such as RC filters or filters defined by a tanh function. Such filtered optimization ensures that a distorted waveform passed through *e.g.* a transmission line, will still exhibit near-optimal performance at the qubit. An example RC-filtered pulse waveform is highlighted in Fig. 13d. Additionally, the Q-CTRL optimization package supports optimization of evenly-sampled smooth functions. In this mode, optimized pulses are represented as evenly-spaced samples from a smooth function and propagated using a Runge-Kutta integrator, which leads to a model of system dynamics with greater accuracy in the presence of physical hardware limitations.

Finally, we also offer a CRAB-type [53, 54] optimization in which a waveform is selected from a superposition in the Fourier basis and discretized in time. This truncates the effective search space by limiting it to the associated Fourier coefficients, and is therefore independent of the granularity of the piecewise-constant discretization. The Q-CTRL optimization package contains a flexible CRAB implementation that allows a variety of

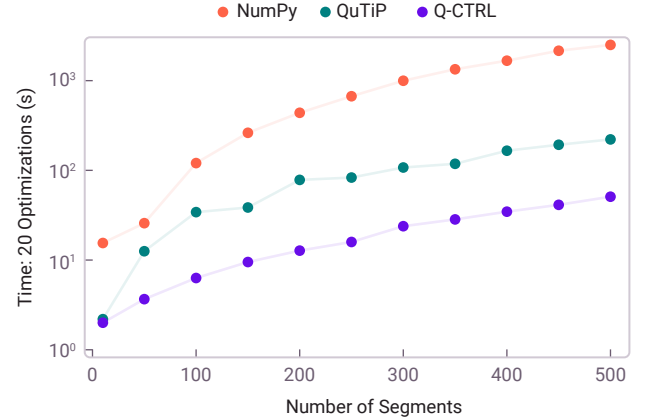


FIG. 7. Head-to-head local-instance performance benchmarking of Q-CTRL optimization tools vs optimization complexity (measured by number of segments). Time-to-solution is presented on a logarithmic scale, demonstrating an approximately order-of-magnitude enhancement in performance over QuTiP, and  $\sim 100\times$  improvement over local-instance NumPy. Additional performance benefits are achieved via parallel processing in a cloud architecture that are not captured here.

CRAB techniques (*e.g.* bases with randomized frequencies, fixed frequencies or optimizable frequencies) to be incorporated alongside other constraint options.

## 3. Optimizer performance benchmarking

The Q-CTRL optimization engine provides performance which outstrips competitive packages in both flexibility and time to solution. In head-to-head performance benchmarking in a local-instance implementation we find greater than order-of-magnitude performance improvements over NumPy optimization tools and approximately  $5\times$  advantage relative to optimization tools in QuTiP. We note, however, that the general flexibility to perform constrained optimization is often not possible at all with other tools. Moreover, the cloud-architecture of Q-CTRL products provides an additional parallelization advantage which translates to approximately  $9\times$  improvement in time-to-solution over a local-instance implementation on a modern PC. This ultimately translates to nearly  $\sim 50\times$  speedup in optimizer performance over the broadly available competitive packages.

## D. Time-domain simulation tools for realistic hardware error processes

An independent approach for analysing the dynamics of an algorithm or gate in the presence of noise is via time-domain simulation. Provided the noise-free evolution of the system is well-understood, simulation may be

Optimizer Constraint Description	Technical Details
<p><b>Smooth Controls:</b> The temporal variation in a control waveform is bounded to ensure smooth transitions and limit discontinuous transitions requiring high bandwidths.</p>	<p>A “smooth” waveform may be obtained via one of multiple methods:</p> <ul style="list-style-type: none"> <li>(i) Limiting the effective time-derivative for any drives or shifts, <i>e.g.</i> <math> \Omega(\tau_i) - \Omega(\tau_{i-1})  &lt; (\delta\Omega)_{\text{Max}}</math>.</li> <li>(ii) Composing candidate control waveforms as superpositions in the Fourier basis before discretized sampling in time.</li> <li>(iii) Employing a novel smooth-function sampling routine based on Runge-Kutta integration.</li> </ul> <p>These approaches ensure that for any targeted channel the rate of change of controls between segments is bounded, and are equivalent, by the properties of the Fourier transform, to imposing a maximum frequency cutoff on the control.</p>
<p><b>Filtered Controls:</b> Control pulses are transformed by a linear-time-invariant filter</p>	<p>To account for hardware bandwidth limitations, ideal pulse segments may be transformed into filtered waveforms using arbitrary linear-time-invariant filters such as RC filters with specified high-frequency cutoff, <math>\omega_{\text{max}}</math>, tanh, or equivalent filters capturing transmission-line dynamics.</p>
<p><b>Bounded-Strength Controls:</b> For any control pulse, the magnitude of the pulse waveform may be bounded. This ensures the optimization does not exceed physically motivated bounds on control parameters.</p>	<p>For any drive pulse <math>j \in \{1, \dots, d\}</math>, or shift pulse <math>l \in \{1, \dots, s\}</math>, upper bounds on pulse waveforms may be enforced, such that</p> $\begin{aligned}\Omega_j(t) &\leq \Omega_{\text{max},j} \\  \alpha_l(t)  &\leq \alpha_{\text{max},l}\end{aligned}$ <p>where <math>\Omega_{\text{max},j}</math> and <math>\alpha_{\text{max},j}</math> define the maximum (positive) permissible value of drive modulus or shift amplitude waveforms respectively.</p>
<p><b>Fixed-Control Waveforms:</b> For any individual control, the pulse waveform may be held fixed and effectively frozen out of the variational search.</p>	<p>For any drive pulse <math>j \in \{1, \dots, d\}</math>, or shift pulse <math>l \in \{1, \dots, s\}</math>, set</p> $\begin{aligned}\Omega_j(t) &= f_j(t) \\ \phi_j(t) &= g_j(t) \\ \alpha_l(t) &= h_l(t)\end{aligned}$ <p>where <math>f_j(t)</math>, <math>g_j(t)</math>, <math>h_l(t)</math> are specific functions of time. For the segmentation described in App. B, this corresponds to setting</p> $\{\Omega_j, \phi_j, \alpha_l\} \rightarrow \text{constant vector}$
<p><b>Concurrent vs Interleaved Controls:</b> Control pulses on different drives and shifts are executed sequentially or simultaneously.</p>	<p>In certain physical systems it is not possible to implement all controls simultaneously. In this case the control Hamiltonian must be constructed from appropriately sequenced drive/shift operations. This is achieved by transforming the optimization variables in Eq. (44) as <math>\mathbf{v} \rightarrow \mathbf{v} \cdot \mathbf{b}</math>, where <math>\mathbf{b}</math> is a binary mask enforcing the required structure of interleaved operations. For <math>\mathbf{b}</math> set to unity, controls may be applied concurrently.</p>

TABLE II. Constraint options for Q-CTRL’s numerical optimization toolkit.

used to investigate system dynamics in the presence of different noise sources.

Simulation packages based on Schrödinger integration and matrix multiplication are commonly found in many software packages, including free repositories such as

Qiskit [55] and GST [56]. However, the integration of noise to simulate realistic environments is typically restricted to a small set of quasi-static offsets or the incorporation of fully stochastic depolarizing noise.

Q-CTRL provides several unique tools for simulating

quantum systems exhibiting correlated and colored noise channels as typically encountered in realistic laboratory environments. These capabilities significantly expand a user's ability to understand and predict the impact of noise and hardware imperfection on algorithmic performance. These tools are designed to be efficient and to give access to information which is not typically available through conventional simulation packages.

The core Q-CTRL simulation module accepts a control Hamiltonian (expressed as drives, shifts and drifts, as described in App. B), together with any number of arbitrary piecewise-constant time-domain noise processes. These noise processes can multiplicatively perturb the moduli of the drive or shift controls, or contribute additively to the system Hamiltonian. From this information, the simulation module produces an overall piecewise-constant system Hamiltonian, and solves the Schrödinger equation via matrix exponentials to compute the unitary time evolution operator for the system at arbitrary times.

This package provides several key functions that enable efficient and useful simulation in noisy environments:

- Creation of a time-domain noise process from an input user-defined noise power spectral density
- Incorporation of a user-defined time-series into a simulation, including data-series interpolation
- Automated homogenization of time-segmentation of all input and software-defined time series in order to permit Schrödinger integration from data sets expressing different temporal discretization
- Forward propagation of an initial input state subject to calculated time-evolution operators including noise
- Calculation of ensemble-averaged density matrices over independent but statistically identical noise realizations.

In the remainder of this subsection we provide a technical exposition on each of these capabilities.

### 1. Technical details of simulation functionality

The first objective in this simulation framework is to convert a noise process which is conveniently expressed as a power spectral density (*e.g.* oscillator phase noise or magnetic field noise) to a time-domain representation. Consider a (one-sided) user-defined noise power spectral density  $S(\omega)$ , sampled at discrete frequencies  $S_k = S(k\Delta\omega)$  (for  $0 \leq k \leq N - 1$  and spacing  $\Delta\omega$ ).

Samples from the corresponding two-sided spectrum are defined by symmetrizing and rescaling the one-sided spectrum:

$$S_k^{(2)} := \begin{cases} S_0 & k = 0 \\ 0.5S_k & 1 \leq k \leq N - 1 \\ 0.5S_{2N-1-k} & N \leq k \leq N - 2. \end{cases} \quad (46)$$

Next, a discrete amplitude spectral density,  $\{\hat{x}_k\}$ , is generated from the two-sided power spectral density using  $S_k^{(2)} = |\hat{x}_k|^2$ , meaning the phases of the  $\hat{x}_k$  may be chosen arbitrarily. Accordingly, the amplitude spectral density is defined as

$$\hat{x}_k := e^{i\phi_k} \sqrt{S_k^{(2)}}, \quad (47)$$

where  $\phi_k$  is chosen uniformly at random for  $1 \leq k \leq N - 1$ , and we fix  $\phi_0 := 0$  and  $\phi_k := \phi_{2N-1-k}$  for  $N \leq k \leq 2N - 2$  (which ensures Hermitian symmetry of  $\{\hat{x}_k\}$ ). Finally, the real time series corresponding to the generated amplitude spectral density is produced via a suitably-normalized discrete inverse Fourier transform:

$$x_k = \sqrt{\Delta\omega} \sum_{l=0}^{N-1} \hat{x}_l e^{2\pi i \frac{kl}{N}}. \quad (48)$$

This process yields a single random realization of a real time-domain signal with a power spectrum matching the input spectrum  $S(\omega)$ .

Given this form of a discrete, real, time series generated from a noise power spectral density (created as above or provided directly by the user), it may be desirable to perform simulation using a higher sampling rate than that native to the data (for example if only low-frequency noise is specified). The Q-CTRL simulation package enables this upsampling via Whittaker-Shannon interpolation. This produces a continuous-time function  $\{x_k\}$  that interpolates the initial time series, with a band limit set by the Nyquist frequency of the series

$$x(t) = \sum_{k=-\infty}^{\infty} x_k \text{sinc}\left(\frac{t - k\Delta t}{\Delta t}\right), \quad (49)$$

where  $\Delta t$  is the time spacing between samples. To approximate the infinite sum, the simulation package automatically performs periodic extension of the input series and truncation of the sum to accuracy within the domain of the original time series.

With discretized time-series data in hand it becomes possible to simulate the time evolution of a system via integration of the Schrödinger equation. However, in many cases the natural temporal discretizations will vary between different fields within the system. For example, rapidly-fluctuating noise sources may be defined on significantly shorter time scales than control fields, while quasi-static noise processes could be defined on longer time scales.

To enable simulation in such cases, all discretizations are automatically resampled on a shared grid prior to integration. This enables a user to simply input data series as-is and the package will handle all homogenization issues. For example, if a drive control pulse is defined on two segments of duration  $\tau/2$  by  $[\Omega_1, \Omega_2]$ , but a noise process is defined on three segments of duration  $\tau/3$  by  $[\beta_1, \beta_2, \beta_3]$ , the shared discretization has six segments of

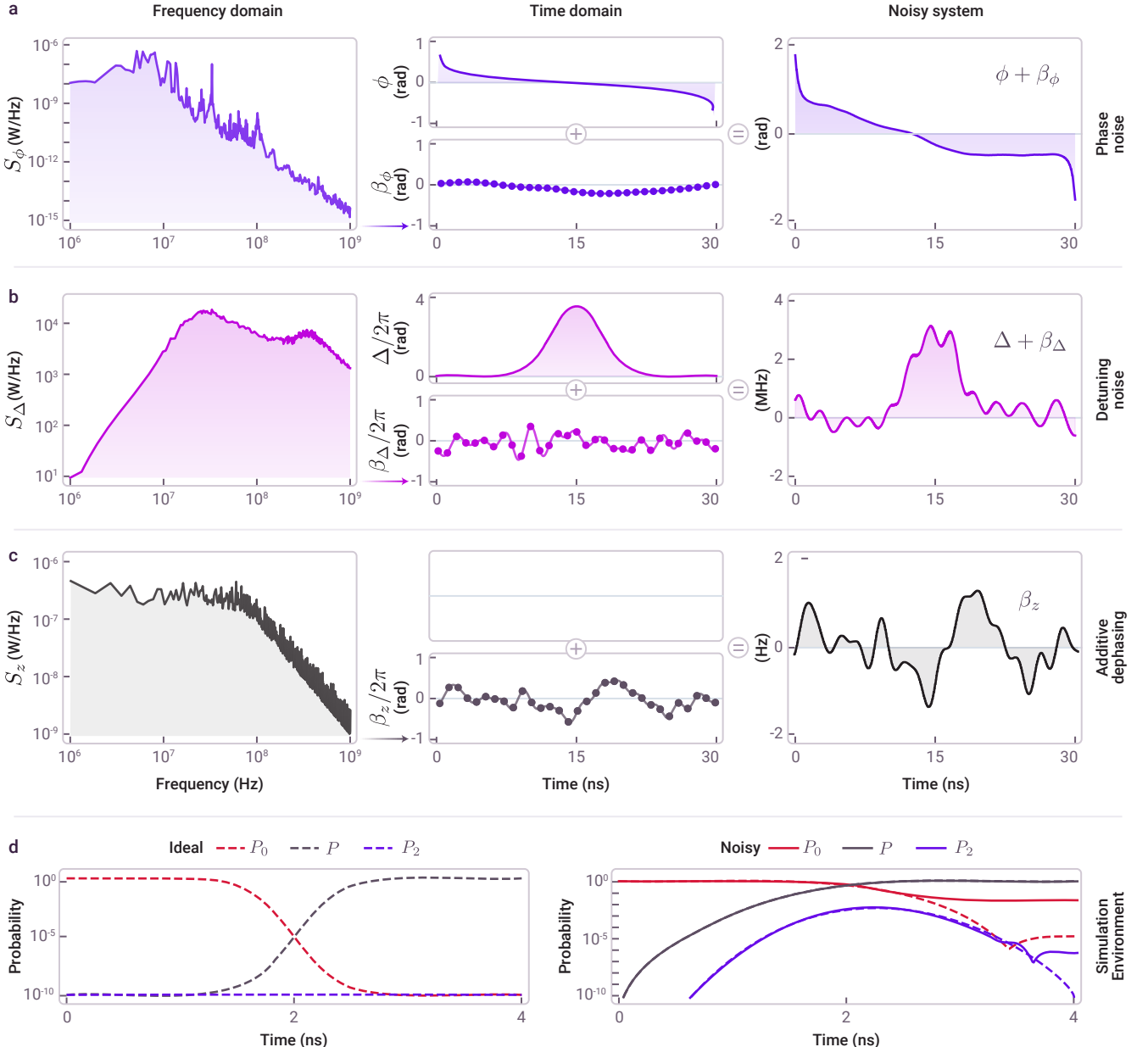


FIG. 8. Demonstration of time-series simulation for a Gaussian DRAG pulse implementing an  $X$  gate on a qutrit subject to leakage. The control corresponds to a Gaussian DRAG pulse including a Gaussian envelope on the  $X$  quadrature, its time derivative on  $Y$ , and a Gaussian-squared pulse on  $Z$ . (a-c) Left column: frequency-domain noise power spectra input into simulation tool. Middle column: interpolated single-instance time-series derived from noise channels and associated control channels (where appropriate). Right column: Noisy control operators combining time-domain noise process and controls. Three different noise processes are included relevant to implementation of DRAG: (a) phase noise on  $Y$  quadrature of microwave control, (b) microwave detuning, (c) ambient dephasing. (d) time-domain evolution under ideal and noisy evolutions, representing populations as a function of time for states  $|0\rangle$ ,  $|1\rangle$ , and  $|2\rangle$ . This simulation assumes perfect control on the  $X$ -quadrature with noise as indicated above.

duration  $\tau/6$  with drive pulse  $[\Omega_1, \Omega_1, \Omega_1, \Omega_2, \Omega_2, \Omega_2]$  and noise  $[\beta_1, \beta_1, \beta_2, \beta_2, \beta_3, \beta_3]$ .

Following resampling, and letting the endpoints of the  $N$  piecewise-constant time segments be  $\tau_k$  for  $1 \leq k \leq N$ ,

the Hamiltonian can be written

$$H(t) = \begin{cases} H_1 & 0 \leq t \leq \tau_1 \\ \dots \\ H_N & \tau_{N-1} < t \leq \tau_N. \end{cases} \quad (50)$$

With this representation in place, calculation of the unitary time evolution operator  $U(t)$  is achieved by integrating the Schrödinger equation via the matrix exponential:

$$U(t) = e^{-iH_k(t-\tau_{k-1})} e^{-iH_{k-1}(\tau_{k-1}-\tau_{k-2})} \dots e^{-iH_1\tau_1},$$

where  $k$  is chosen such that  $\tau_{k-1} < t \leq \tau_k$ .

The Q-CTRL simulation package provides a function to propagate an initial state using the unitary time evolution operator (calculated via the integration process described above). Specifically, for samples of the unitary time evolution operator  $U_l = U(t_l)$  (evaluated at arbitrary times  $\{t_l\}$ ), propagation of an initial state  $|\psi_0\rangle$  to the state  $|\psi_l\rangle$  at time  $t_l$  is given by

$$|\psi_l\rangle = U_l|\psi_0\rangle.$$

In general, however, calculating a single instance of the temporal evolution of the state is insufficient to understand the target dynamics, and an ensemble average over different noise realizations is required. The Q-CTRL simulation package provides a function to compute the mean density matrix associated with an ensemble of propagated state vectors. Given a set of state vectors  $\{|\psi^m\rangle\}$  (for  $1 \leq m \leq M$ ) produced from an ensemble of simulations corresponding to different noise realizations, the mean density matrix  $\rho$  is given by

$$\rho = \frac{1}{M} \sum_{m=1}^M |\psi^m\rangle\langle\psi^m|.$$

## 2. Simulation example

In [Fig. 8](#) we demonstrate this capability in order to simulate the impact of noise on a Gaussian DRAG pulse used to perform a leakage-suppressed single-qubit operation in a superconducting circuit [\[57\]](#). This particular example focuses on the execution of a single quantum logic operation subject to high-frequency noise; however with this package it is easy to extend this simulation to complex multi-operation circuits experiencing noise on a variety of timescales.

This simulation includes time-varying  $Y$ -quadrature phase noise on a microwave drive, a time-varying microwave detuning and an additive ambient dephasing field applied to the qubit. In each case an input power spectral density (left column) is converted to a time-series and combined with the relevant control channel (middle column), resulting in a noisy system representation (right column). The simulated performance in the ideal case is shown in [Fig. 8d](#), indicating high fidelity state transfer from  $|0\rangle \rightarrow |1\rangle$  with negligible population of the leakage level  $|2\rangle$ . However, in the presence of noise the fidelity of state transfer is reduced by approximately three orders of magnitude and a leakage error emerges.

## E. Characterizing hardware noise

Identifying opportunities for hardware improvement and deploying high-performance robust quantum controls benefits from access to microscopic information about the noise in user hardware, beyond that captured in more generic error characterization routines [\[58\]](#). In the filter function framework this is captured through the noise power spectral density, a statistical frequency-domain representation of noise processes such as ambient dephasing or control noise. Having access to this information is a key requirement for both the evaluation of control performance and control optimization, both described above, and serves as a complement to Hamiltonian learning procedures [\[59, 60\]](#).

In general detailed information about noise power spectral density is not easily determined when sources may be local to a device and inaccessible to traditional measurement protocols. This limit may be overcome by using a qubit as a measurement device to directly probe the noisy environment and pursuing non-parameterized spectral estimation. Consider a noise Hamiltonian  $H_{\text{err}}$  as in [Eq. \(21\)](#), comprised of multiple independent noise sources, each described by a corresponding PSD. Application of appropriate time-domain modulation to the qubit can change the noise sensitivity (by tuning the filter function for the control), as well as the noise operator to which the qubit is most sensitive. The problem treated here is how to reconstruct these PSDs from measurable quantities.

The process of noise characterization follows a simple workflow, highlighted schematically in [Fig. 9](#):

- Create controls based on the target noise operator and hardware limits such as maximum experimental duration and timing resolution
- Output controls and perform measurements using the prescribed protocols
- Perform data fusion on measurement results to reconstruct a noise power spectrum.

There is a tight integration between the type of noise to be characterized, the available control protocols, and the data fusion routine employed for spectrum reconstruction. A range of routines is available for the characterization of both multiplicative and additive Hamiltonian noise channels, corresponding, *e.g.* to control-amplitude noise and ambient dephasing, respectively. Users may ultimately trade experimental simplicity against the complexity and (in)stability of numerical data-fusion routines.

In cases where experimental simplicity is prioritized, dephasing-noise information can be obtained using timed sequences of simple driven rotations, often referred to as pulsed dynamical decoupling sequences. Here quantum bit flips are sequenced in order to produce a filter function with a dominant peak at the frequency defined by

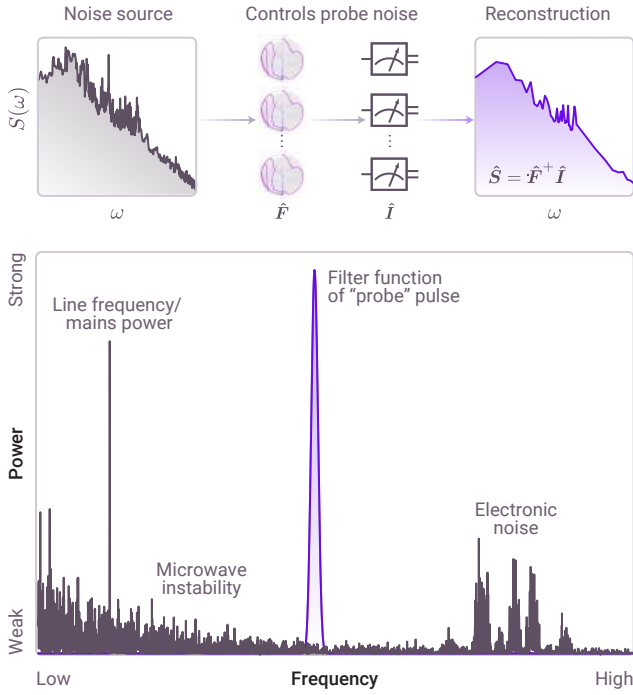


FIG. 9. Overview of the noise characterization process using multi-dimensional filter functions and SVD spectral inversion technique. Upper: A noise source is probed by a sequence of control solutions each providing sensitivity to a different spectral range, as determined by the multi-dimensional filter function. Measurement results are then used to produce a reconstruction of the actual spectrum experienced by the qubit, with degradation in fidelity determined by the available controls and numeric routine. Lower: Concept demonstrating how an appropriately constructed filter function can serve as a narrowband probe of underlying noise processes, giving access to different technical components of the noise spectrum. Selecting an alternate control can shift the peak in the filter function in order to allow broadband sampling of the noise spectrum.

the inverse interpulse delay. These controls unfortunately require a numerically intensive data fusion procedures based on a large matrix inversion in order to appropriately account for the many harmonics appearing in the filter function. Moreover, performing inversion mandates very strict requirements on sequence structure which can ultimately induce limits on achievable frequency resolution.

Shaped controls based on so-called Slepian waveforms are highly effective for the characterization of both control noise and dephasing. These controls are provably optimal in terms of spectral concentration, *i.e.* how much spectral weight resides within a target band. Accordingly they mitigate issues of spectral leakage which cause unwanted out-of-band signals to contribute to the measurement as a form of *interference*. They can be thought of as mathematically optimal window functions applied directly to the qubit itself, restricting the qubit's sensitivity to noise. These approaches are powerful in their ability to suppress out of band interference and require very simple post-measurement processing, but require arbitrary pulse shaping.

We have focused on producing a novel spectrum reconstruction protocol which allows a user to employ well conditioned control sequences while relaxing both common performance limits and the computational intensity of spectrum reconstruction. Any relevant set of measurements may be employed to characterize a target noise channel, with an overall frequency-dependent sensitivity function. Data fusion is conducted using a machine-learning technique based on an efficient implementation of pseudo-inverse by singular value decomposition (SVD). This enables parameter-free estimation needed to perform reconstructions without a priori knowledge of the underlying structure of the noise. This approach is easily generalized beyond single qubits based on the multi-dimensional filter-function formalism summarized in Sec. IV B, and as demonstrated experimentally in Sec. V D.

Consider a quantum system consisting of  $p$  independent noise sources

$$H_{\text{err}}(t) = \sum_{k=1}^p \beta_k(t) N_k(t) \quad (51)$$

where the  $\beta_k(t)$  are stochastic scalar-valued noise fields with corresponding PSDs,  $S_k(\omega)$ . The structure of  $H_{\text{err}}(t)$  may be probed by defining a set of  $c$  distinct control protocols

$$\{H_{\text{ctrl},j}(t)\}, \quad j \in \{1, \dots, c\} \quad (52)$$

and measuring the corresponding infidelities. From Sec. IV B, and assuming the noise is sufficiently weak, the infidelities may be approximated as

$$\sum_{k=1}^p \int_{-\infty}^{\infty} \frac{d\omega}{2\pi} F_k^j(\omega) S_k(\omega) \approx \mathcal{I}^{(j)}, \quad j \in \{1, \dots, c\} \quad (53)$$

where  $F_k^j(\omega)$  is the leading-order filter function associated with the  $j$ th control protocol and  $k$ th noise source. The filter functions may be computed using Eq. (34) given knowledge of the control Hamiltonians and dynamical noise generators, while the infidelities may be obtained from experiment.

Let  $[\omega_{\min,k}, \omega_{\max,k}]$  denote the frequency domain spanned by the low- and high-frequency cutoffs, assuming they exist, for each PSDs in Eq. (53). We may then define the sample frequencies

$$\omega_{k,\ell} = \omega_{\min,k} + (\ell - 1)\Delta\omega_k, \quad (54)$$

for samples  $\ell \in \{1, \dots, s(k)\}$ , incremented by frequency steps

$$\Delta\omega_k = \frac{\omega_{\max,k} - \omega_{\min,k}}{s(k) - 1} \quad (55)$$

on each domain  $k \in \{1, \dots, p\}$ . Assuming sufficiently large sample numbers,  $s(k)$ , Eq. (53) may be recast as a discrete sum, with the integrals approximated using the trapezoidal rule. Specifically

$$\hat{I}^j = \frac{\Delta\omega_k}{2\pi} \hat{F}_{k,\ell}^j \hat{S}^{k,\ell} \left(1 - \frac{\delta_{\ell,1}}{2}\right) \left(1 - \frac{\delta_{\ell,s(k)}}{2}\right) \quad (56)$$

where  $\delta_{ij}$  is the Kronecker delta[61], and the sum runs implicitly over repeated tensor indices. Here we have introduced the following tensor notation for the various sampled quantities

$$F_k^j(\omega_{k,\ell}) \approx \hat{F}_{k,\ell}^j \pm \Delta\hat{F}_{k,\ell}^j \quad (57)$$

$$S_k(\omega_{k,\ell}) \approx \hat{S}^{k,\ell} \pm \Delta\hat{S}^{k,\ell} \quad (58)$$

$$\mathcal{I}^{(j)} \approx \hat{I}^j \pm \Delta\hat{I}^j \quad (59)$$

where at  $\hat{Q}$  denotes the estimated value for the quantity  $Q$ , and  $\Delta\hat{Q}$  denotes its uncertainty. See App. D1 for a discussion of estimates and uncertainties for the respective measured and calculated quantities.

The challenge, then, is to obtain estimates,  $\hat{S}^{k,\ell} \pm \Delta\hat{S}^{k,\ell}$  for the power spectral densities by inverting the relationship defined by Eq. (56), given knowledge of the measured quantites  $\hat{I}^j \pm \Delta\hat{I}^j$  and computed values  $F_k^j \pm \Delta F_k^j$ . To facilitate efficient numerical solutions we move to a matrix representation. Namely,

$$\hat{\mathbf{F}}\hat{\mathbf{S}} = \hat{\mathbf{I}}, \quad (60)$$

where  $\hat{\mathbf{F}} = [\hat{\mathbf{F}}_1 \ \hat{\mathbf{F}}_2 \ \dots \ \hat{\mathbf{F}}_p]$  is a horizontal concatenation of matrices of the form

$$\hat{\mathbf{F}}_k = \frac{\Delta\omega_k}{2\pi} \begin{bmatrix} \frac{1}{2}\hat{F}_{k,1}^1 & \hat{F}_{k,2}^1 & \dots & \hat{F}_{k,s(k)-1}^1 & \frac{1}{2}\hat{F}_{k,s(k)}^1 \\ \frac{1}{2}\hat{F}_{k,1}^2 & \hat{F}_{k,2}^2 & \dots & \hat{F}_{k,s(k)-1}^2 & \frac{1}{2}\hat{F}_{k,s(k)}^2 \\ \vdots & \vdots & \ddots & \vdots & \vdots \\ \frac{1}{2}\hat{F}_{k,1}^c & \hat{F}_{k,2}^c & \dots & \hat{F}_{k,s(k)-1}^c & \frac{1}{2}\hat{F}_{k,s(k)}^c \end{bmatrix}, \quad (61)$$

the estimated PSDs are concatenated vertically as

$$\hat{\mathbf{S}} = \begin{bmatrix} \hat{S}_1 \\ \hat{S}_2 \\ \vdots \\ \hat{S}_p \end{bmatrix}, \quad \hat{S}_k = \begin{bmatrix} \hat{S}^{k,1} \\ \hat{S}^{k,2} \\ \vdots \\ \hat{S}^{k,s(k)} \end{bmatrix}, \quad (62)$$

and the estimated infidelities are arranged as

$$\hat{\mathbf{I}} = \begin{bmatrix} \hat{I}^1 \\ \hat{I}^2 \\ \vdots \\ \hat{I}^c \end{bmatrix}. \quad (63)$$

The matrix dimensions therefore satisfy

$$\dim(\hat{\mathbf{F}}) = c \times n \quad (64)$$

$$\dim(\hat{\mathbf{S}}) = n \times 1 \quad (65)$$

$$\dim(\hat{\mathbf{I}}) = c \times 1 \quad (66)$$

where  $n = \sum_{k=1}^p s(k)$ . From Eq. (60), performing noise reconstruction thus reduces to solving the matrix inverse problem  $\hat{\mathbf{S}} = \hat{\mathbf{F}}^{-1} \hat{\mathbf{I}}$ , solutions to which are discussed in the next section.

Depending on the particular set of controls and noise sources, and on the dimensions  $c$ ,  $p$ , and  $n$ , the exact matrix inverse  $\hat{\mathbf{F}}^{-1}$  may not exist. Generally, the system may be underdetermined or overdetermined, and the matrix  $\hat{\mathbf{F}}$  may be singular. An approximate solution may, however, be obtained via singular-value decomposition (SVD). This may be used to obtain a pseudo-inverse if the problem is undetermined, to perform regression if it is over-determined, or to calculate the exact inverse if it is in fact determined. *Usefully, in all cases, the singular value decomposition of  $\hat{\mathbf{F}}$  takes the same general form:*

$$\hat{\mathbf{F}} = \mathbf{U} \mathbf{D} \mathbf{V}^\dagger, \quad (67)$$

Here,  $\mathbf{U}$  is a  $(c \times c)$  unitary matrix,  $\mathbf{V}^\dagger$  is a  $(n \times n)$  unitary matrix, and  $\mathbf{D}$  is a  $(c \times n)$  rectangular diagonal matrix with non-negative real numbers on the diagonal. The columns of  $\mathbf{U}$  and  $\mathbf{V}$  are the left- and right-singular vectors of  $\hat{\mathbf{F}}$ , and the diagonal elements of  $\mathbf{D}$ , denoted  $s_i$ , are known as the singular values. The final representation is then given by

$$\hat{\mathbf{S}} = \mathbf{V} \mathbf{D}^+ \mathbf{U}^\dagger \hat{\mathbf{I}}, \quad (68)$$

where  $\mathbf{D}^+$  is a diagonal matrix with entries  $1/s_i$  for all non-zero singular values, and zero otherwise. Further details on the SVD method, techniques to include measurement uncertainties, and our approaches to truncating singular values are presented in App. D.

## V. QUANTUM CONTROL CASE STUDIES

In the sections above we described the role of quantum control in combating hardware error, and introduced new technical capabilities for the characterization and optimization of quantum hardware performance. In this section we provide case studies to demonstrate the application of these capabilities in contemporary quantum computing hardware. First, we provide experimental demonstrations of performance of open-loop control solutions in trapped-ion hardware, demonstrating error-robustness as well as error-rate homogenization in space and time. Second, we apply the numerical optimization package described in Sec. IV C to generate single and multi-qutrit gates optimized for robustness against leakage and dephasing errors in a coupled-transmon system. Third, we apply the SVD spectral reconstruction software outlined in Sec. IV E to the IBM Q cloud-based quantum processor to characterize noise affecting two-qubit cross-resonance gates. Finally, we present an example of optimizing the structure of a quantum circuit, producing a logically-equivalent compiled circuit exhibiting suppression of cross-talk errors arising from a constant  $ZZ$  interaction. We emphasize that these examples

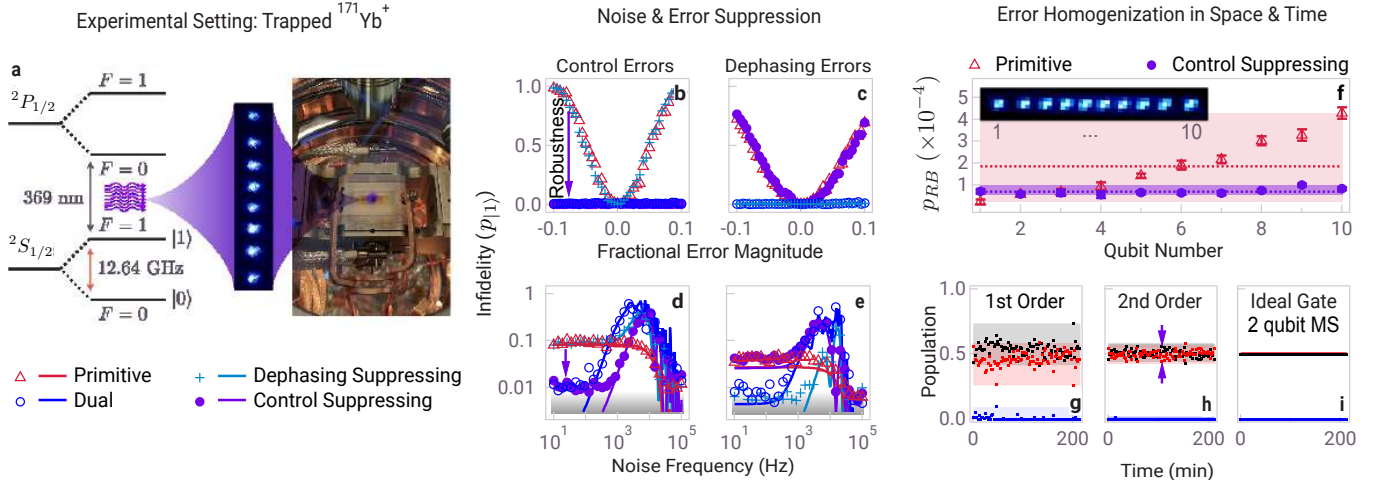


FIG. 10. Experimental validation of key capabilities in quantum firmware. (a) Schematic of experimental platform in use, based on trapped Ytterbium ions as described in detail in [38, 52]. (b-c) Experimental demonstration of robustness to quasistatic errors using known open-loop dynamically corrected gates. The *control suppressing* gate is BB1, *dephasing suppressing* is CORPSE, and *dual suppressing* gate is CinBB. BB1 and CORPSE are single-axis error suppressing DCGs, designed to suppress over-rotation control errors and off-resonance dephasing errors respectively, and reduced CinBB is designed to suppress errors in both quadratures. The control-noise-suppressing gate appears most robust to control errors, as indicated by a low measured infidelity as a function of applied overrotation error. Similarly, the dephasing suppressing gate shows similar performance in the presence of dephasing errors, and the dual suppressing gate shows comparable performance in the presence of both forms of error. (d-e) Demonstration of robustness to time-varying noise for the same DCGs, matched to filter-function predictions. Again, low values of measured infidelity indicate robustness; all gates show an onset of error susceptibility at high frequencies near the inverse gate time, while error-suppressing gates show robustness at low noise frequencies (left of the graph). (f) Demonstration of error homogenization in space across a ten-qubit device using open-loop control, measured by randomized benchmarking. In this system, ions are simultaneously addressed by a global microwave control field to drive global single-qubit rotations. However, due to a gradient in the strength of the microwave field due to interference patterns, the qubits rotate with a spatially varying Rabi rate. Shading indicates the range of experimental outcomes while the mean error across the device is indicated by lines. Using DCGs the mean error is reduced  $\sim 5\times$  while the range (measured either by the standard deviation or the difference between minimum and maximum values) is reduced  $\sim 10\times$ . (g-h) Demonstration of improved stability of a two-qubit Molmer-Sorensen gate using control solutions. As the order of error-suppression is increased by control construction, the range of measured values of ion populations is narrowed while the system operates continuously over approximately 3.5 hours. Here black is  $P_0$ , the measured probability of zero ions measured in  $|1\rangle$ , blue is  $P_1$ , the probability of one ion in  $|1\rangle$ , and red is  $P_2$ , the probability of two ions in  $|1\rangle$ . The ideal gate configuration is shown in panel (i) with  $P_0 = P_2 = 0.5$  and  $P_1 = 0$ . Colored shading represents the range of the associated data set over the measurement window. Further experimental details are available in Appendix E.

are not exhaustive representations of product capability, and that additional demonstrations for *e.g.* optimizing parallel Molmer-Sorensen gate implementation, or characterizing simultaneous noise processes in spin qubits will be presented in separate manuscripts.

### A. Open-loop control benefits demonstrated in trapped-ion QCs

Trapped-ion quantum computers already exist at medium scales and provide an ideal platform for studies of quantum control efficiency due to long intrinsic lifetimes, high-fidelity operations, and access to multiqubit devices. We have used a trapped-ion quantum computer composed of individual  $^{171}\text{Yb}^+$  ions in order to explore the efficacy of quantum control and quantum control optimization in real hardware.

We begin with demonstrations of error-robustness using open-loop control solutions available in the *OpenControls* package of driven single-qubit operations. In Fig. 10 we probe the robustness of various composite control operations which induce a net bit flip  $X$  (equivalently a  $\pi$  pulse) to systematic quasistatic errors in the pulse area and dephasing due to a detuning from the qubit frequency (Fig. 10b-c). Protocols designed to provide robustness to the associated error channel reveal little deviation from the baseline error rate achieved in the center of the graph (zero induced error) while the measured infidelity ( $\mathcal{I}$ ) increases rapidly in the presence of systematic errors for non-robust controls. This difference is a key signature of error-robust control solutions.

Similarly, using a so-called ‘system-identification’ technique to probe control robustness to a time-varying perturbation [17] we demonstrate that appropriately crafted controls suppress noise at frequencies slow compared with

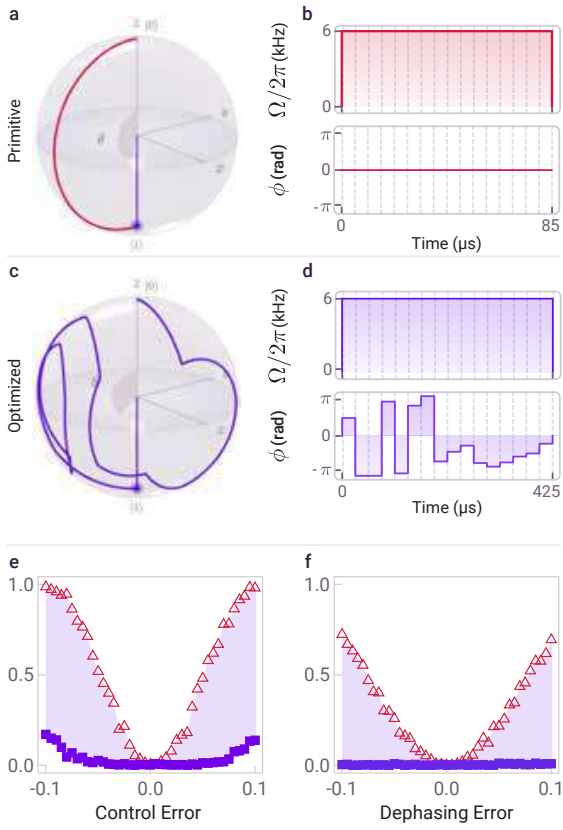


FIG. 11. Demonstration of optimized controls in a trapped-ion quantum computer. (a) and (c) Bloch sphere representation of primitive and numerically optimized robust controls, respectively. Robust control was constrained to ensure a fixed pulse amplitude and optimized to provide dual suppression of both detuning and amplitude errors. (b) and (d) Polar coordinate representation of waveforms used to implement a net  $X$  rotation. The optimized control implemented in (d) is constrained to have a fixed amplitude and only undergoes phase modulation. (e) and (f) demonstration of robustness against quasistatic overrotation and detuning errors; low values correspond to small measured errors. The x-axis is expressed fractionally relative to the Rabi rate or qubit frequency respectively. Shading represents the net improvement in error robustness afforded by the optimized solution. Further details of the implementation are provided in App. E.

the control rate (Fig. 10d-e). Experimental measurements compare well with calculation of the control filter function (solid lines), which is available through both BLACK OPAL and BOULDER OPAL. In particular, these experiments demonstrate that it is possible to construct single-qubit logic operations robust to noise in both the control amplitude and qubit-frequency detuning.

Moving beyond physical-layer benefits we can also probe the manner in which these control operations intersect with higher levels of the quantum computing stack as described in Sec. II B. For instance, in Fig. 10 f we demon-

strate homogenization of Parallel Randomized Benchmarking (RB) error rates across a 10-qubit quantum computer using error-suppressing open-loop gate constructions validated in Fig. 10 b-e. Here the dominant error source is a spatial gradient in the coupling of the qubit drive field to the individual ions, due to reflections and interference of the 12.6 GHz microwaves inside the ion-trap vacuum enclosure. We therefore select an control-noise suppressing solution and replace all gates in the randomized benchmarking procedure with their logically equivalent error-robust constructions [38].

In this experiment the best-performing qubit does not exhibit a net improvement in the measured RB error rate,  $p_{RB}$ —a proxy measure for gate error—beyond measurement uncertainty due to other limiting error sources such as laser-light leakage. However, all other qubits exhibit RB error rates that now approximately match the best reported values and show a narrowing of the spread of outcomes across the device. Quantitatively, the standard deviation of RB error rates across the 10-qubit array is reduced  $10.2\times$  using the appropriate open-loop control solution.

Moving beyond the application of control solutions for single-qubit gates, we examine the stability of two-qubit gates realized via the Mølmer-Sørensen interaction on a pair of trapped ions as the system experiences drifts in time. In this experiment we are targeting the creation of a Bell state  $(|00\rangle - i|11\rangle)/\sqrt{2}$ ; ideally in this experiment there is an equal probability of measuring two ions in  $|0\rangle$  or  $|1\rangle$ , and one should never observe any experiments with one ion each in these two states. Therefore our key proxy measure for gate performance is the measured population of zero, one, and two ions in state  $|1\rangle$ . The expected performance of these metrics is shown in Fig. 10 i.

We compare two different gate constructions, one being relatively susceptible to drifts and the other designed to reduce sensitivity via a modulation protocol available in both BLACK OPAL and BOULDER OPAL, and experimentally demonstrated first in [52, 62]. Repeatedly performing the same gate shows variations in the measured ion-state populations, corresponding to reductions in gate fidelity. However, by using the error-suppressing gate construction we observe a  $\sim 3-4\times$  reduced susceptibility to system drifts, indicated by arrows in Fig. 10 h, showing the reduced range of outcomes.

Finally, we demonstrate the efficacy of numerically optimized single-qubit gates against various noise processes in trapped-ion qubits in Fig. 11. Specifically, we have focused on the use of the optimization toolkit described in Sec. IV C to produce gates that are simultaneously robust against control noise and dephasing. Typically this requires a concatenated analytic construction which dramatically extends the control duration by up to  $24\times$  relative to the primitive gate. For an  $X$  gate the optimizer returns solutions showing simultaneous robustness to error with a gate duration reduced  $\sim 5\times$  relative to this analytic approach. In the presence of quasistatic

errors the numerically optimized solutions provide show robustness to error in the presence of up to 10% miscalibrations in qubit frequency and Rabi rate, similar to the results of [Fig. 10b-c](#). Similar results (not shown) have been obtained using superconducting circuits on IBM Q. The particular solution employed for the superconducting circuit was implemented using IBM’s OpenPulse format [\[40\]](#) through Qiskit, and was slew-rate-limited in order to comply with band-limits in transmission lines (such constraints are generally not germane in trapped-ion systems due to the relatively long pulse durations and use of microwave antennae rather than transmission lines). Further details on the execution of these experiments is included in [App. E](#).

## B. Simultaneous leakage and noise-robust controls for superconducting circuits

For superconducting qubits, a two-level system is typically singled out from the many levels of an anharmonic oscillator. When driven by naive single-qubit controls, the system is subject to off-resonant coupling to leakage levels outside the qubit manifold, resulting in substantial *leakage errors*. In addition, these qubits face the common challenges of decoherence from ambient dephasing, control-phase and control-amplitude noise.

Suppression of leakage errors has been the focus of considerable research in the superconducting community and has been demonstrated to improve gate performance. The standard approach at present employs an analytic optimal control technique to implement target quantum operations via so-called DRAG pulses [\[57\]](#), or variants thereof. For example, half-DRAG is designed to suppress leakage out of the qubit subspace via dual-quadrature control, typically involving a Gaussian pulse on  $\sigma_x$ , and its time derivative simultaneously applied on  $\sigma_y$ .

Unfortunately this technique does not combine successfully with other open-loop error-suppression strategies needed to combat decoherence from additional noise channels, *e.g.* NMR-inspired composite pulses [\[28\]](#). For example, concatenation of pulse segments defined by DRAG into an overall CORPSE structure, known to suppress detuning noise (see [Sec. V A](#)), fails as the dual-axis DRAG control breaks the geometric construction required to provide noise robustness.

Advancing on previous work, we present optimal and robust controls that simultaneously reduce sensitivity to both leakage and dephasing errors by orders of magnitude, using BOULDER OPAL optimization tools. Our starting point is the Hamiltonian for an anharmonic three-level qutrit subject to dephasing noise and leakage to the lowest-lying excited state in the system ([Fig. 12a](#)):

$$H(t) = \frac{\chi}{2}(a^\dagger)^2(a^2) + \gamma(t)a + \gamma^*(t)a^\dagger + \frac{\Delta(t)}{2}a^\dagger a + \beta_z(t)\sigma_z \quad (69)$$

where  $a = |0\rangle\langle 1| + \sqrt{2}|1\rangle\langle 2|$ . We encode this anharmonic oscillator using a *drift* control with operator  $\frac{\chi}{2}(a^\dagger)^2a^2$ ; a microwave *drive* control with operator  $a$  and complex pulse envelope  $\gamma(t) = \Omega(t)e^{-i\phi(t)}$ ; a *clock shift* control with operator  $a^\dagger a/2$  with a real pulse envelope  $\Delta(t)$ ; and an additive noise operator with Pauli operator  $\sigma_z$  (see [App. B](#) for further details on this representation).

We perform two robust-control optimizations subject to different constraints ([Table II](#)). First, we implement a concurrent optimization allowing dual-quadrature controls similar in required controls to half DRAG (*e.g.* IQ modulation). Next we perform a fixed-waveform optimization that holds the amplitude of the control pulse associated with the microwave drive fixed while allowing its phase to vary, as in phase-modulation. The resulting waveforms are displayed in [Fig. 12](#).

We compare performance in three distinct ways which illustrate the simultaneous robustness to both leakage and dephasing errors in a pulse whose duration is the same as the half-drag solution. First, we represent the dephasing-noise operator associated filter function. We see that the filter functions for the two optimized controls show a low-frequency-noise suppressing character similar to that illustrated in [Fig. 6](#), while all other controls indicate broadband noise admittance. Next, we use the numerical simulation tools described in [Sec. IV D](#) to determine control robustness to quasistatic dephasing errors. In this circumstance the two optimized solutions demonstrate a broad *plateau* of fixed detunings over which the infidelity remains low, again following the experimental results of [Fig. 10b-c](#). Finally, we simulate the full evolution of the three states of the qutrit under application of the net  $X$  rotation and applied noise. Here we see that despite the complex dynamics at times less than the gate time, at the conclusion of the gate the optimized solutions show the appropriate net state transfer. Other optimization approaches such as RC-filtered and slew-rate-bounded controls have been used to demonstrate similar performance. Overall these solutions represent totally new controls that – for the first time – allow simultaneous leakage-error and dephasing-noise suppression.

## C. Robust control for parametrically-driven superconducting entangling gates

In this subsection we present novel parametrically-driven iSWAP gates optimized for error robustness. Parametric activation of entangling gates presents an alternative paradigm enabling tunable, high-fidelity two-qubit gates [\[63, 64\]](#). This overcomes the scaling penalty imposed by frequency crowding in conventionally coupled

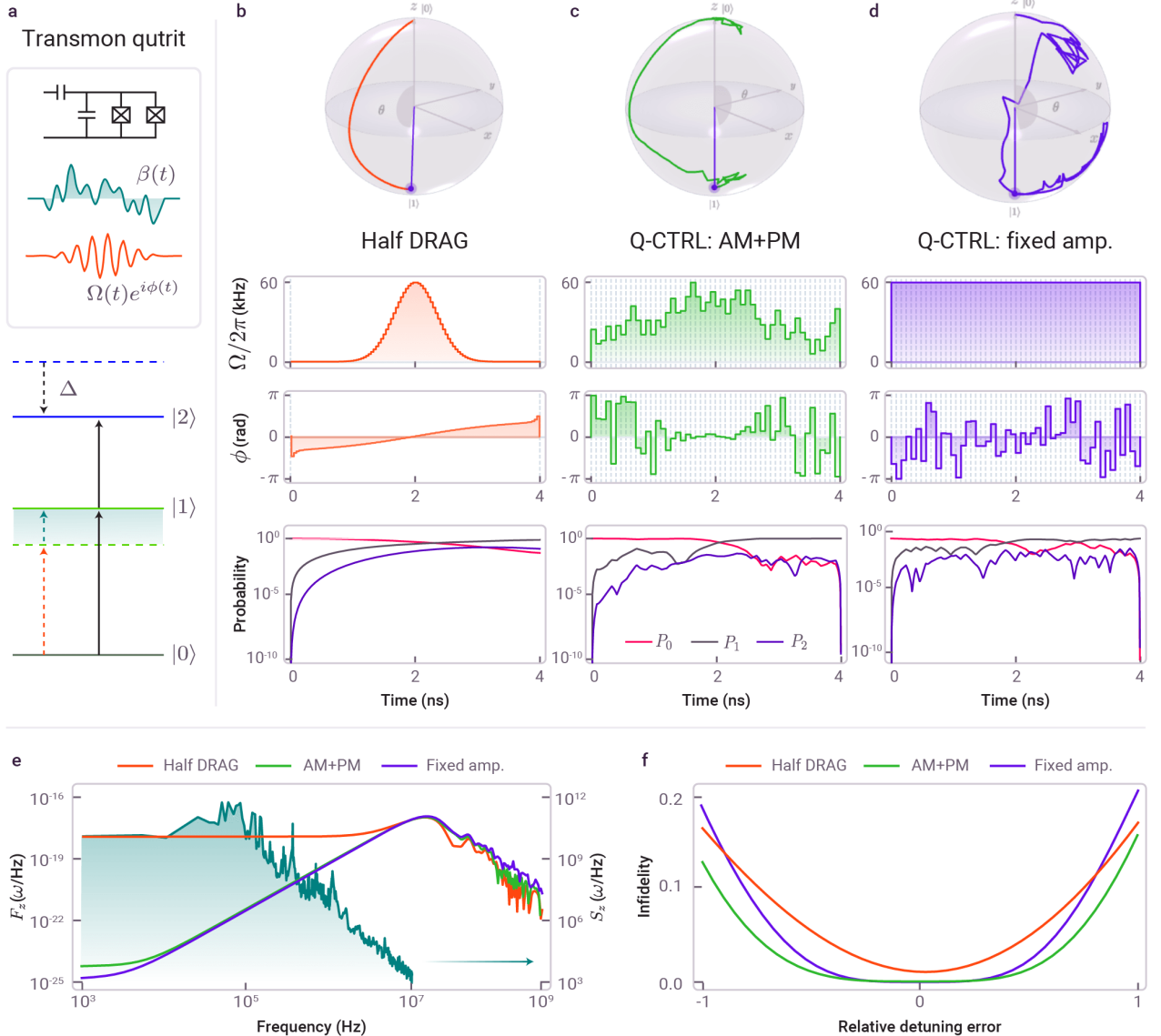


FIG. 12. Comparison of standard and Q-CTRL optimized control solutions for simultaneous dephasing and leakage error suppression. (a) Level and control diagram for the transmon circuit under consideration. The driving field is applied concurrently with a time-varying noise process  $\beta(t)$ . This time-varying field causes a shift in the qubit level spacing which results in an effective detuning between the drive field and the qubit levels, resulting in dephasing. (b-d) Control solutions on the Bloch sphere, in polar coordinates, and demonstrations of simulated probabilities of state occupancy during the gate application. An ideal gate results in perfect state transfer from  $|0\rangle \rightarrow |1\rangle$ , meaning the probabilities state populations should take values  $P_0 \rightarrow 0$ ,  $P_1 \rightarrow 1$ , and  $P_2 \rightarrow 0$  (leakage channel). In this presence of noise the Q-CTRL solutions suppress  $P_0$  and  $P_2$  at the end of the gate by orders of magnitude relative to Half DRAG. (e) Filter function representation of different controls for dephasing field  $\beta(t)$  represented in the Fourier domain as  $S_z(\omega)$ . The Q-CTRL Filter functions, which are small at low frequencies, suppress noise and provide robustness. (f) Quasistatic error robustness of controls as a function of a fixed detuning between the qubit frequency and microwave drive. Robustness is demonstrated by controls which stay near zero away from the center of the graph, indicating improved performance of both optimized Q-CTRL solutions. Even if  $\beta(t) \rightarrow 0$ , the flat plateau for the Q-CTRL solutions shows superior robustness relative to Half DRAG.

transmons [65], though it suffers from decoherence channels arising from control noise in the parametric drive. We perform first-principles analyses of dominant error channels and introduce novel gate structures incorporating numeric optimization via BOULDER OPAL in order

to suppress the influence of these control errors.

Two-qubit parametrically-driven gates may be implemented between one fixed- and one tunable-frequency transmon. A control flux drive  $\hat{\Phi}(t)$ , with frequency  $\omega_p$  and phase offset  $\theta_p$ , is applied to the tunable-frequency

control solution	$C_{\text{optimal}}$	$C_{\text{robust}}$	$\mathcal{I}_{\text{tot}}$
Primitive	$2.2 \times 10^{-1}$	$2.6 \times 10^{-2}$	$2.2 \times 10^{-1}$
Half-DRAG	$9.1 \times 10^{-3}$	$4.1 \times 10^{-2}$	$1.1 \times 10^{-2}$
Q-CTRL: AM+ $\Phi$ M	$9.1 \times 10^{-9}$	$1.6 \times 10^{-8}$	$2.5 \times 10^{-7}$
Q-CTRL: fixed amp.	$2.7 \times 10^{-9}$	$4.9 \times 10^{-9}$	$2.6 \times 10^{-7}$

TABLE III. Performance metrics for control solutions presented in Fig. 12(d-g). Here  $C_{\text{optimal}}$  and  $C_{\text{robust}}$  are defined as in Table I. The total infidelity  $\mathcal{I}_{\text{tot}}$  is computed as the sum of two contributions:  $\mathcal{I}_{\text{optimal}}$ , and  $\mathcal{I}_{\text{robust}}$ , with the integral computed with respect to the dephasing PSD plotted Fig. 12(b).

transmon resulting in a modulated transition frequency of the form

$$\omega_T(t) = \bar{\omega}_T + \tilde{\omega}_T \cos(2\omega_p t + 2\theta_p) \quad (70)$$

where  $\bar{\omega}_T$  is the average shift in qubit frequency and  $\tilde{\omega}_T$  is the amplitude of the modulation caused by the applied flux drive. The Hamiltonian for the system under this modulation, transforming to an interaction picture, takes the form

$$\begin{aligned} H_{\text{int}}(t) = & g(t) \sum_{n=-\infty}^{\infty} J_n \left( \frac{\tilde{\omega}_T}{2\omega_p} \right) e^{+i(2\omega_p t + 2\theta_p)n} \\ & \times \left\{ e^{-it\Delta} |10\rangle\langle 01| \right. \\ & + \sqrt{2} e^{-i(\Delta + |\eta_F|)t} |20\rangle\langle 11| \\ & + \sqrt{2} e^{-i(\Delta - |\eta_T|)t} |11\rangle\langle 02| \\ & \left. + 2e^{-i(\Delta + |\eta_F| - |\eta_T|)t} |21\rangle\langle 12| + \text{H.C.} \right\}. \end{aligned} \quad (71)$$

Here  $g(t)$  describes the capacitive coupling between the transmon qubits;  $\eta_T(\eta_F)$  are the positively-defined anharmonicities for the tunable-frequency (fixed-frequency) transmons;  $\Delta = \bar{\omega}_T - \omega_F$  is the detuning between the average transition frequency of the tunable-frequency qubit and the fixed transition frequency of the fixed-frequency qubit; and  $J_n(x)$  is the  $n$ th-order Bessel function of the first kind. A detailed description of the underlying physical system and the derivation of the associated Hamiltonians can be found in [63, 64, 66, 67].

Target entangling gates are activated by matching the modulation frequency  $\omega_p$  to the detuning between relevant energy levels of the capacitively-coupled transmons. For typical experimental parameters, the time-dependent phase factors on the Hamiltonian operators above lead to rapidly-oscillating terms in the system evolution that effectively suppress the coupling rate to the associated transitions. Activation of a target transition is achieved by resonantly tuning the drive frequency to cancel the associated phase factor. In particular:

$$\text{iSWAP: } |10\rangle \leftrightarrow |01\rangle \quad 2n\omega_p = \Delta \quad (72)$$

$$\text{CZ}_{20}: \quad |11\rangle \leftrightarrow |20\rangle \quad 2n\omega_p = \Delta + \eta_F \quad (73)$$

$$\text{CZ}_{02}: \quad |11\rangle \leftrightarrow |02\rangle \quad 2n\omega_p = \Delta - \eta_T \quad (74)$$

The use of a parametric drive with a user-defined amplitude, phase, and frequency introduces a new control-induced channel for errors in the gate. To account for these control errors we assume the flux drive, and consequently the parametric drive in Eq. (70), experience three distinct error processes

$$\text{modulation offset error: } \bar{\omega}_T \rightarrow \bar{\omega}_T + \bar{\epsilon}_T \quad (75)$$

$$\text{modulation amplitude error: } \tilde{\omega}_T \rightarrow \tilde{\omega}_T + \tilde{\epsilon}_T \quad (76)$$

$$\text{modulation frequency error: } \omega_p \rightarrow \omega_p + \epsilon_p \quad (77)$$

where the  $\epsilon$  are assumed to be small errors. These generate additional Hamiltonian terms which, performing a Taylor expansion in the small offset parameters and moving to the interaction picture, result in the noise Hamiltonian  $H_{\text{err}}(t) = \beta(t)N$ , where  $\beta(t)$  captures the effective noise strength. We introduce a noise-operator of the form

$$N = \mathbb{I}_F \otimes (\Pi_1 + 2\Pi_2). \quad (78)$$

Here  $\Pi_i = |i\rangle\langle i|$  defines the projection operator onto the  $i$ th eigenstate of the tunable-frequency transmon, and  $\mathbb{I}_F$  is the identity on the fixed-frequency transmon.

The iSWAP interaction is activated by resonantly driving the  $|10\rangle\langle 01|$  term, for example by setting the 1st-order ( $n = 1$ ) resonance condition  $\omega_p = \Delta/2$ . Assuming this configuration we may therefore restrict attention to the relevant  $(4 \times 4)$  iSWAP subspace, spanned by the eigenstates

$$|00\rangle, \quad |10\rangle, \quad |01\rangle, \quad |11\rangle. \quad (79)$$

In this case the remaining rapidly-oscillating terms may be ignored, and Eq. (71) reduces to

$$H_{\text{iSWAP}}(t) \approx \frac{1}{2}\Lambda(t)e^{+i\xi(t)} |10\rangle\langle 01| + \text{H.C.} \quad (80)$$

where the parametric coupling rate  $\Lambda = 2g(t)J_1\left(\frac{\bar{\omega}_T}{2\omega_p}\right)$  and the parametric drive phase  $\xi = 2\theta_p$ .

On the iSWAP subspace the noise operator defined in Eq. (78) reduces to

$$N = \frac{1}{2}\mathbb{I}_F \otimes \sigma_z = \begin{pmatrix} -\frac{1}{2} & 0 & 0 & 0 \\ 0 & \frac{1}{2} & 0 & 0 \\ 0 & 0 & -\frac{1}{2} & 0 \\ 0 & 0 & 0 & \frac{1}{2} \end{pmatrix} \quad (81)$$

resembling dephasing on the subspace of the tunable-frequency qubit. This new analysis thus shows that the three different channels for the introduction of noise via the parametric drive are manifested at the Hamiltonian level as an effective dephasing process.

Our objective is now to craft control solutions which are able to suppress this effective dephasing channel using the control available to us. Incorporating the fixed-frequency transmon term

$$H_{\text{qubit-F}}(t) = \left( \frac{1}{2}\Omega(t)e^{+i\phi(t)} |0\rangle\langle 1| + \text{H.C.} \right) \otimes \mathbb{I}_T \quad (82)$$

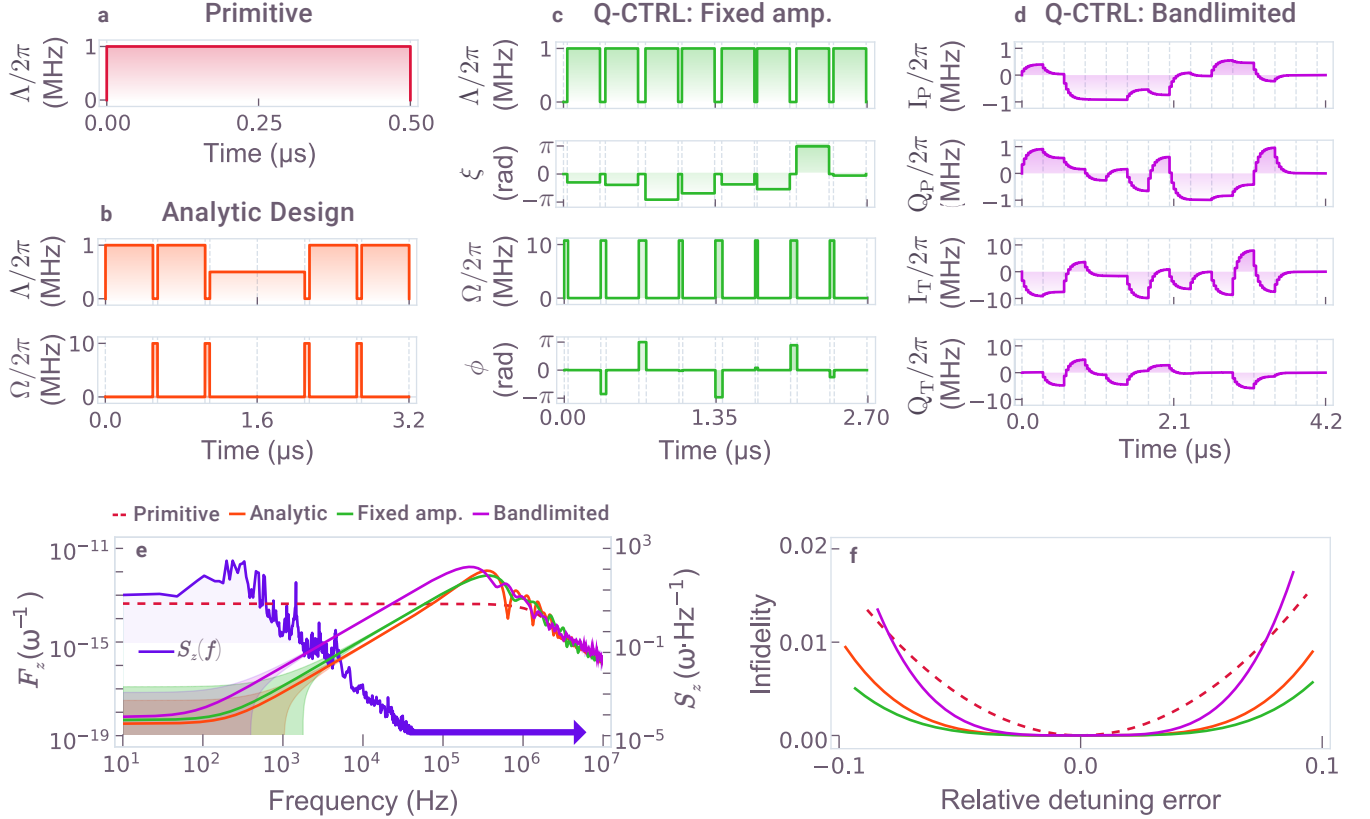


FIG. 13. Optimized error-robust control solutions for two-qubit parametrically driven entangling gates in superconducting circuits. (a) Primitive coupling gate (b) analytically designed Walsh-modulated gate, (c) Numerically optimized interleaved gate construction with fixed-amplitude constraints (phase modulation only) (d) Numerically optimized concurrent gate with band-limited 5 MHz RC filter integrated into optimization. (e) Filter functions for control solutions overlaid with an example noise power spectrum for ambient dephasing, showing noise-suppressing capabilities of Q-CTRL solutions. (f) quasi-static error susceptibility as a function of relative detuning error (measured relative to  $\Lambda$ ).

the full control Hamiltonian is then written

$$H_{\text{ctrl}}(t) = H_{\text{iSWAP}}(t) + H_{\text{qubit-F}}(t). \quad (83)$$

This Hamiltonian is then parameterized according to the prescription in App. B,  $H_{\text{ctrl}}(t) = \gamma(t)\mathbf{C} + \text{H.C.}$  in terms of the drive pulses and operators

$$\gamma(t) = [\Lambda(t)e^{+i\xi(t)}, \Omega(t)e^{+i\phi(t)}],$$

$$\mathbf{C} = \left[ \begin{smallmatrix} \frac{1}{2}|10\rangle\langle 01| \\ \frac{1}{2}|01\rangle\langle 10| \otimes \mathbb{I} \end{smallmatrix} \right].$$

We introduce three novel solutions providing robustness against control errors in the parametrically activated gate. All combine an iSWAP coupling drive  $\Lambda(t)$  with single-qubit rotations which yields full control over the relevant subspace. This may be examined by observing that sandwiching an iSWAP operation between a pair of single-qubit  $X$  gates permits the realization of the (Hermitian) operator

$$A_{\text{eff}} \propto \begin{pmatrix} 0 & 0 & 0 & 1 \\ 0 & 0 & 0 & 0 \\ 0 & 0 & 0 & 0 \\ 1 & 0 & 0 & 0 \end{pmatrix}, \quad (84)$$

similar in structure to a general NOT gate. Solutions need not employ this particular gate, but leverage the full controllability afforded by the *combination* of single-qubit and iSWAP control modulation.

The first solution we present is fully defined analytically (Fig. 13b), recognizing that dephasing noise can be mitigated by the action of the spin echo and Walsh-modulation on a driven operation. We combine single-qubit  $X$  operations with an iSWAP control envelope defined using a superposition of Walsh functions. This approach has previously been used to craft dephasing-robust single-qubit driven operations [17, 68] and provide a simple means to realize error robustness. In this case the gate construction strongly suppresses both quasi-static and time-varying control errors as expressed us-

ing our multi-dimensional filter functions and numeric simulation (Fig. 13e-f).

In Fig. 13c-d we also present two representative numerically optimized solutions subject to constraints outlined in Table II. First, we produce a fixed-amplitude solution which combines a phase-modulated coupling drive with an *interleaved* single-qubit control, compatible with situations in which both controls cannot be applied simultaneously. The single-qubit operations are enacted with fixed amplitude, but variable durations (hence variable rotation angles) and variable phase. Similarly we present a *band-limited, concurrent* solution incorporating these two drives. Here we have enforced, as an example, an RC-filter on the controls to match potential band limits as may be experienced in a system with finite transmission-line bandwidth. Again in these cases we observe enhanced robustness to quasistatic errors, validated by time-domain simulation, as well as time-varying noise, as captured through filter functions (Fig. 13e-f).

Overall these examples demonstrate how high-performance solutions may be achieved under a wide range of constraints for entangling gates in superconducting circuits. We have achieved similar results for the CZ gate and non-parametric cross-resonance gates.

control solution	$C_{\text{optimal}}$	$C_{\text{robust}}$	$\mathcal{I}_{\text{tot}}$
Primitive	0.0	1.73	$2.6 \times 10^{-4}$
Analytic	0.0	0.0	$1.5 \times 10^{-6}$
Q-CTRL: fixed amp.	$1.6 \times 10^{-8}$	$2.0 \times 10^{-12}$	$2.0 \times 10^{-6}$
Q-CTRL: bandlimited	$2.0 \times 10^{-9}$	$7.3 \times 10^{-9}$	$4.9 \times 10^{-6}$

TABLE IV. Performance metrics for control solutions presented in Fig. 13(i-l). Here  $C_{\text{optimal}}$  and  $C_{\text{robust}}$  are defined as in Table I. The total infidelity  $\mathcal{I}_{\text{tot}}$  is computed as the sum of two contributions:  $\mathcal{I}_{\text{optimal}}$ , and  $\mathcal{I}_{\text{robust}}$ , with the integral computed with respect to the noise PSD plotted Fig. 13(g).

#### D. Experimental noise characterization of multiqubit circuits on an IBM cloud QC

Microscopic noise characterization is widely employed in the development of optimized control solutions for a range of devices including superconducting qubits [69]. However, existing protocols have focused on the characterization of global fields measured at the single-qubit level [70–72]. Q-CTRL’s multi-dimensional filter functions (Sec. IV B) and flexible noise reconstruction algorithms (Sec. IV E) permit new insights to be gleaned from real experimental quantum computing hardware.

We have focused on the characterization of previously unidentified microscopic noise sources present in entangling gates executed on cloud-based superconducting quantum computers [55]. At present access to such systems is highly restricted, making the arbitrary application of complex modulated controls on subspaces

within the machines impossible. Accordingly, we have developed and deployed a simplified probing sequence consisting of sequences of entangling gates for two-qubit noise characterization. This probing sequence is readily implementable on the current IBM quantum computing platform.

Our probing sequence is designed to characterize two-qubit dephasing noise defined by the noise operator  $N = \frac{1}{2}(Z_a - Z_b)$ , where  $Z_a$  and  $Z_b$  are the Pauli  $Z$  operator on qubits  $a$  and  $b$ , respectively. This probing sequence consists of a fixed number  $M$  of single-qubit and two-qubit quantum gates, in which each quantum gate has a fixed gate duration of  $T_g$ . Fixing  $M$  - and in particular the number of two-qubit gates used - ensures that signatures arising from imperfect execution of the entangling gates do not vary between sequences and swamp the noise signals to be measured. In general,  $M$  can be chosen suitably based on the hardware specification and  $T_g$ ; here, we choose  $M = 66$  to ensure the total duration of the experiment is within the coherence time of the IBM NISQ computers and  $T_g = 110\text{ns}$ .

We first prepare the Bell state  $(|01\rangle + |10\rangle)/\sqrt{2}$  by applying a sequence of 3 quantum gates defined by

$$U_E = H_a \text{CNOT}_{ab} X_b, \quad (85)$$

where  $\text{CNOT}_{ab}$  is the controlled-not gate on control qubit  $a$  and target qubit  $b$ ,  $H_a$  is the Hadamard operator on qubit  $a$  and  $X_b$  is the Pauli  $X$  operator on qubit  $b$ . Then  $i$  identity gates are applied to both qubits followed by a swap operation defined as

$$SW = \text{CNOT}_{ab} H_{ab} \text{CNOT}_{ab} H_{ab} \\ \text{CNOT}_{ab} H_{ab} \text{CNOT}_{ab}, \quad (86)$$

where  $H_{ab} = H_a \otimes H_b$ . A second  $SW$  operation is applied after an additional  $j$  identity gates. Then  $M - 16 - i - j = 50 - i - j$  identity gates are employed before reverting the quantum state via the  $U_E^\dagger$  operation. The schematic of the probing sequence is shown in Fig. 14b. This probing sequence effectively implements a series of  $\pi$  pulses for the two-qubit system, mimicking the behaviour of CPMG sequences executed on a single-qubit system.

A set of generalized filter functions and the composite spectral sensitivity function for the set of control sequences can be constructed for each sequence as  $i, j$  vary (Fig. 14d). Subsequently, when the two-qubit system is subject to noise, a corresponding set of infidelity measurements can be obtained and used to infer the noise power spectral density via the SVD noise reconstruction method described in Sec. IV E. We note that the fact that the sequences are highly constrained in structure (based on the limits of the IBM hardware) makes standard matrix inversion approaches to spectrum reconstruction impossible.

We implement the new probing sequence on the IBM Q 5 Tenerife (*ibmqx4*) quantum computer [73]. Fig. 14a depicts the device chip layout and qubit couplings; here, we choose the qubit pair  $Q_0$  and  $Q_2$  for the experimental

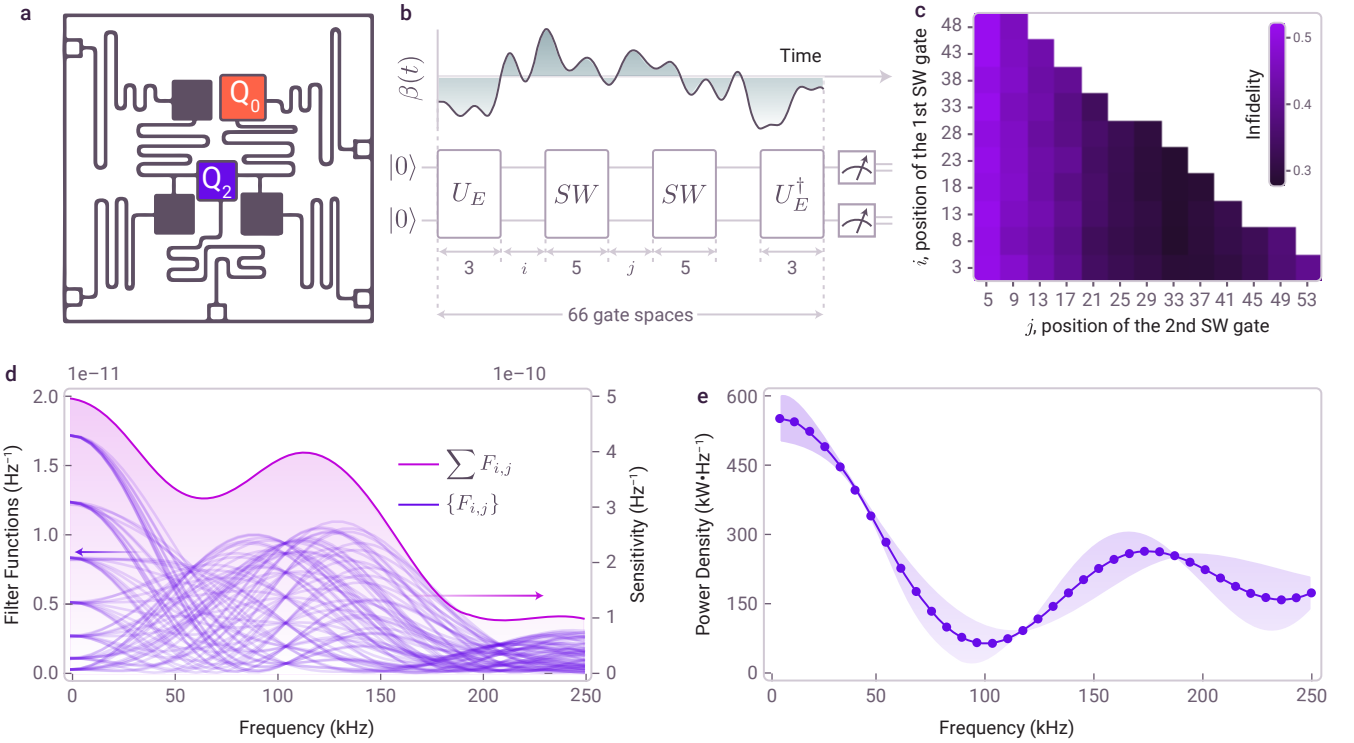


FIG. 14. Noise characterization in the IBM Q 5 Tenerife (ibmqqx4) device. (a) Chip layout is shown identifying the two qubits for which data are presented. (b) A Schematic of the probing sequence structure with time-varying dephasing noise; the convolution of these two processes in the time domain gives a product in the Fourier domain as captured via the multi-dimensional filter function. (c) Measured infidelity from all probing sequences specified by the index pair  $i, j$  denoting the location of the two swap gates employed in the sequence. (d) multi-dimensional filter functions for the target noise channel are shown for all sequences tested, as well as the net sensitivity function. (e) Reconstructed dephasing noise power spectral using the SVD reconstruction method with a  $10^{-13}$  threshold for singular value truncation.

results displayed, but all pairs have been characterized in detail yielding qualitatively similar results. For this device, CNOT<sub>20</sub> can be natively implemented between these two qubits.

The values of  $i$  and  $j$  for the probing sequences are varied to construct a set of filter functions with high sensitivity for a broad range of frequencies of interest, up to 250 kHz. For each chosen values of  $i, j$ , the corresponding quantum circuit was executed over 8192 shots, yielding the average infidelity depicted in Fig. 14c as a colorscale heatmap. For a fixed  $i$ , as  $j$  increases until the second  $SW$  operation is placed roughly half-way between the first  $SW$  and the  $U_E^\dagger$  operations, the average infidelity becomes small, resembling an echo-effect similar to that of CPMG sequences. However there is additional structure present which breaks the symmetry of these graphs, indicating other noise contributions away from DC.

Utilizing the SVD method (Sec. IV E), a reconstructed noise power spectral density based on these results is shown in Fig. 14e. Our result shows that with high confidence, the two-qubit dephasing noise exhibits a low-frequency noise component and a repeatable higher-frequency noise contribution in the range 150 – 200 kHz. The breadth of spectral features observed is due

to the Fourier limits of the individual measurements employed in the reconstruction routine, as confirmed by numerical simulations. We have observed similar performance across multiple qubit pairs, with variations in the strength of the quasi-dc component. Numerical simulations have been used to demonstrate that similar results to those shown in Fig. 14e arise for a simple spectrum composed of a quasi-dc noise component and a single fixed-frequency spur at higher frequencies. Similarly we have confirmed by engineering numerically synthesized data used in the reconstruction that the presence of the feature in the range 150 – 200 kHz does not appear to be an artefact of either the measurement routine or the reconstruction method.

Our experimental results represent an early demonstration of microscopic noise characterization within two-qubit gates. The identification of a high-frequency noise component in a range commonly associated with electronic noise provides guidance on system improvement and noise suppression strategies for these machines.

### E. Crosstalk-resistant circuit compilation

In this subsection we demonstrate the use of optimal control for algorithmic design and compilation. We consider a complex circuit composed of multiple interacting transmons and subject to unwanted cross-coupling. We use Q-CTRL optimization tools in order to implement a target circuit, subject to constraints on control and circuit time, and optimized to combat always-on cross-talk errors through the structure of the circuit itself (no gate-level optimization).

Due to the low anharmonicity of transmons, quantum computations can be designed to exploit the three lowest-energy levels. The relative detunings between the various energy levels in an ensemble of transmons gives rise to an always-on effective ZZ-type coupling Hamiltonian that can be exploited for generating entangling operations. However, this coupling also leads to residual cross-talk errors that degrade algorithmic performance. Below we describe an example physical system and create an optimized circuit compilation which suppresses these residual couplings.

We consider a linear arrangement of 5 qutrits, labelled  $q \in \{1, \dots, 5\}$ . For a given qutrit pair  $p = (q, q+1)$ , characteristic detunings between respective energy levels generate relative phases on states  $|11\rangle, |12\rangle, |21\rangle$ , and  $|22\rangle$ . In this case the total coupling Hamiltonian is written

$$\begin{aligned} H_{zz} = & H_{zz}^{(1,2)} \otimes \mathbb{I} \otimes \mathbb{I} \otimes \mathbb{I} \\ & + \mathbb{I} \otimes H_{zz}^{(2,3)} \otimes \mathbb{I} \otimes \mathbb{I} \\ & + \mathbb{I} \otimes \mathbb{I} \otimes H_{zz}^{(3,4)} \otimes \mathbb{I} \\ & + \mathbb{I} \otimes \mathbb{I} \otimes \mathbb{I} \otimes H_{zz}^{(4,5)} \end{aligned} \quad (87)$$

where nearest-neighbour interactions between pair  $p$  are described by

$$\begin{aligned} H_{zz}^p = & \alpha_{11}^p |11\rangle\langle 11| + \alpha_{12}^p |12\rangle\langle 12| \\ & + \alpha_{21}^p |21\rangle\langle 21| + \alpha_{22}^p |22\rangle\langle 22| \end{aligned} \quad (88)$$

and the  $\alpha_{ij}^p$  are effective coupling strengths, tabulated in Table V for all pairs. Here  $\mathbb{I}$  is the identity on a 3-dimensional single-qutrit Hilbert space,  $H_{zz}^p$  operates on a  $3^2$ -dimensional Hilbert space associated with the  $p$ th qutrit pair, and  $H_{zz}$  operates on the  $3^5$ -dimensional Hilbert space associated total 5-qutrit system.

qutrit pairs $p = (q, q+1)$	$\alpha_{11}^p$ ( $2\pi \cdot \text{MHz}$ )	$\alpha_{12}^p$ ( $2\pi \cdot \text{MHz}$ )	$\alpha_{21}^p$ ( $2\pi \cdot \text{MHz}$ )	$\alpha_{22}^p$ ( $2\pi \cdot \text{MHz}$ )
(1, 2)	-0.27935	0.1599	-0.52793	-0.74297
(2, 3)	-0.1382	0.15827	-0.33507	-0.3418
(3, 4)	-0.276	-0.6313	0.24327	-0.74777
(4, 5)	-0.26175	-0.49503	0.14497	-0.70843

TABLE V. Example ZZ-type coupling strengths between nearest-neighbor qutrit pairs within a circuit.

As an example algorithm, we consider a circuit on this 5-qutrit system which seeks to simultaneously execute controlled-sum (CSUM) gates on qutrit pairs (1, 2) and (3, 4), while leaving the 5th qutrit unaffected. This may be expressed formally as

$$U_{\text{target}} = U_{C\phi} \otimes U_{C\phi} \otimes \mathbb{I} \quad (89)$$

where  $U_{C\phi}$  is a 2-qutrit phase gate, locally equivalent to a CSUM, defined as

$$U_{C\phi} = \begin{pmatrix} 1 & & & & & \\ & 1 & & & & \\ & & 1 & & & \\ & & & 1 & & \\ & & & & \omega^* & \\ & & & & & \omega \\ & & & & & & 1 \\ & & & & & & & \omega \\ & & & & & & & & \omega^* \end{pmatrix} \quad (90)$$

and  $\omega \equiv e^{2\pi i/3}$ .

We consider a physically motivated restricted control basis spanning only single-qutrit operations coupling the levels  $|0\rangle \leftrightarrow |1\rangle$  and  $|1\rangle \leftrightarrow |2\rangle$ . We assume that these may be implemented instantaneously and in parallel across all qutrits within the circuit.

The total control Hamiltonian may be written

$$H_{\text{ctrl}}(\Omega, \phi) = \sum_{q=1}^5 \sum_{\nu \in \{01, 12\}} H_{\nu}^q(\Omega_{\nu}^q, \phi_{\nu}^q) \quad (91)$$

where

$$\Omega = (\Omega_{01}^1, \dots, \Omega_{01}^5, \Omega_{12}^1, \dots, \Omega_{12}^5), \quad (92)$$

$$\phi = (\phi_{01}^1, \dots, \phi_{01}^5, \phi_{12}^1, \dots, \phi_{12}^5). \quad (93)$$

The assumption of instantaneous single-qutrit operations allows us to absorb the duration  $\Delta t$  over which the corresponding unitary is implemented, yielding a total evolution operator

$$U_{\text{ctrl}}(\theta, \phi) = \exp[-iL(\theta, \phi)], \quad \theta = \Delta t \Omega \quad (94)$$

where

$$L(\theta, \phi) = \sum_{q=1}^5 \sum_{\nu \in \{01, 12\}} \theta_{\nu}^q \exp[i\phi_{\nu}^q] C_{\nu}^q + \text{H.C.} \quad (95)$$

Here we refer to driven operations on the  $q$ th qutrit and  $\nu$ th transition, with Rabi rate  $\Omega_{\nu}^q$  and phase  $\phi_{\nu}^q$ .

Within this formulation we have defined single-qutrit drive operators

$$C_{10} = \frac{1}{2} |1\rangle\langle 0| = \frac{1}{2} \begin{bmatrix} 0 & 0 & 0 \\ 1 & 0 & 0 \\ 0 & 0 & 0 \end{bmatrix} \quad (96)$$

$$C_{21} = \frac{1}{2} |2\rangle\langle 1| = \frac{1}{2} \begin{bmatrix} 0 & 0 & 0 \\ 0 & 0 & 0 \\ 0 & 1 & 0 \end{bmatrix} \quad (97)$$

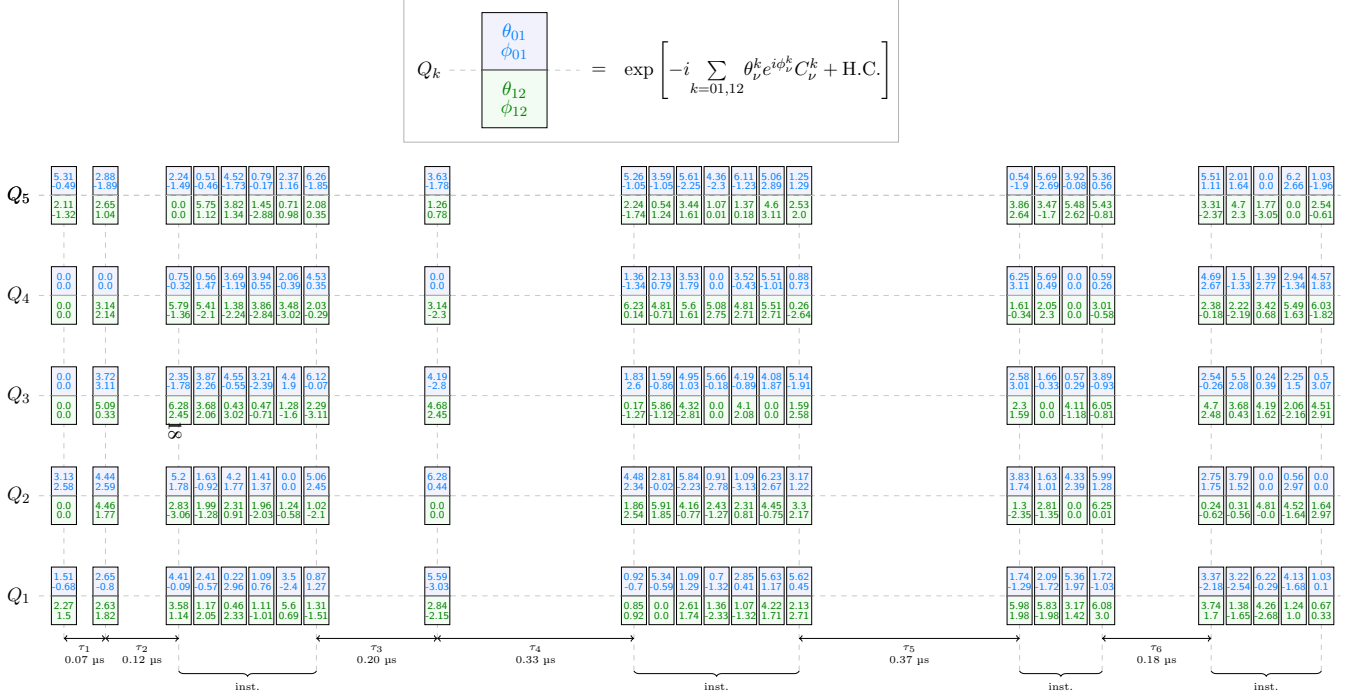


FIG. 15. Optimized 5-qutrit circuit. Each qutrit is controlled via  $|0\rangle \leftrightarrow |1\rangle$  and  $|1\rangle \leftrightarrow |2\rangle$  transitions. Control on each transition is captured via the phasor  $\gamma_\nu = \theta_\nu e^{i\phi_\nu}$ , comprising rotation,  $\theta_\nu$ , and phase angles,  $\phi_\nu$ , where  $\nu \in \{01, 12\}$ . As shown in the inset, each single-qutrit operation is indicated via the block of angles  $[\theta_{01}, \phi_{01}; \theta_{12}, \phi_{12}]$ , with corresponding colours. Consecutive sequences of block arrays indicate product operations of the form  $P_j$  defined in Eq. (99). Blocks of unitary operations are separated by durations  $\tau_j$ . All selected phasor components on the control operations and values of  $\tau_j$  are returned via the circuit optimization procedure. The optimal cost for this circuit compilation is  $\mathcal{I}_{\text{optimal}} = 5.678e^{-3}$ .

which are generalized for the  $q$ th qutrit within the multi-qutrit system

$$C_\nu^q = \mathbb{I}^{\otimes(q-1)} \otimes C_\nu \otimes \mathbb{I}^{\otimes(n-q-1)}, \quad \nu \in \{01, 12\}. \quad (98)$$

Our approach to circuit-level optimization for residual-cross-talk suppression is through the integration of deterministic dynamic decoupling. We partition the circuit implementing Eq. (89) into  $m$  periods of free evolution under the always-on coupling Hamiltonian in Eq. (87), segregated by products of  $k$  distinct control unitaries of the form defined by Eq. (94)

$$P_j = \prod_{\ell=1}^k U_{\text{ctrl}}(\theta_{j,\ell}, \phi_{j,\ell}). \quad (99)$$

starts and Here, the  $j$ th period, of duration  $\tau_j$ , starts and ends with instantaneous unitaries  $P_{j-1}$  and  $P_j$  respectively. This structure corresponds to a generalized dynamic decoupling sequence and augments the controllability of the 5-qutrit system due to the non-commuting terms in the operator products.

This generalized dynamic decoupling sequence structure must now be optimized in order to return the target circuit functionality expressed in Eq. (89), which necessarily entails cancellation of the unwanted  $ZZ$  cross-coupling terms. Optimization of the control structure

is performed on the search space spanned by the timing variables  $\tau = (\tau_1, \dots, \tau_m)$ , rotation variables  $\theta_{\ell,j}$ , and phase variables  $\phi_{\ell,j}$  for  $\ell \in \{1, \dots, k\}$  and  $j \in \{1, \dots, m+1\}$ .

Following the procedure described in Sec. IV C 1, these then form the basis for defining the array of generalized control variables  $\mathbf{v}$ , appropriately normalized for efficient TensorFlow optimization. We also introduce an experimentally motivated constraint in that the circuit must not exceed the qutrit coherence time, set by  $T_1$ . We therefore compose the cost function in Eq. (45) as

$$C(\mathbf{v}) = \mathcal{I}_{\text{optimal}}(\mathbf{v}) + C_{\text{duration}}(\tau) \quad (100)$$

where  $\mathcal{I}_{\text{optimal}}(\mathbf{v})$  is defined in Sec. IV A and  $C_{\text{duration}}(\tau)$  imposes a penalty for exceeding the upper limit chosen for the circuit duration. We set a threshold of  $\sim 1.5 \mu\text{s}$ , chosen assuming a qutrit coherence time of  $\sim 20 \mu\text{s}$ .

The optimizer returns variations on the circuit structure composed of compound rotations on different qutrit levels with variable timing between these operations. The combination of driven rotations and their timing in the sequence is essential in performing the target net unitary with low infidelity; compactifying the circuit structure in order to reduce nominal dead time changes the cross-talk-suppressing nature of the circuit. In the example optimization realized in Fig. 15 we are able to improve

the cross-talk limited fidelity ( $1 - \mathcal{I}_{\text{optimal}}$ ) in the target unitary from  $\sim 2.2\%$  (under the simplest compilation, without any form of dynamic cross-talk suppression) to  $99.4\%$ .

This demonstration validates the underlying premise of circuit-level optimization in order to realize deterministic error robustness. Treating circuit compilation as a challenge in optimal control - for either deterministic error suppression or decomposition of a complex circuit into a constrained set of physical-layer controls - is a feature set incorporated in the Q-CTRL Devkit.

## VI. CONCLUSION AND OUTLOOK

In this manuscript we have provided an overview of the role of quantum control in advancing the field of quantum computing and identified quantum firmware, integrating concepts from this field, as a natural part of the quantum computing stack. We have provided an overview of various theoretical underpinnings of quantum control, with a focus on open-loop error suppression, and have outlined key tasks in quantum control which bring performance benefits to the functioning of quantum computers. This has included experimental evidence derived from real quantum computing hardware demonstrating the key benefits of hardware noise and error suppression, error homogenization in space, hardware stabilization in time, and modification of error correlations for integration with higher-levels of abstraction such as QEC.

In addition to this technical background we introduced Q-CTRL’s suite of *classical* software designed for the development and deployment of quantum control in hardware R&D and quantum algorithm development. Q-CTRL tools span users of various levels of expertise and range from intuitive web interfaces with interactive visualizations through to advanced python toolkits for integration into professional programming tasks. We concluded our presentation with a set of case studies demonstrating the utility of these software capabilities in solving challenging problems in quantum control, and revealing new information about the performance of real quantum computing hardware.

By combining technical rigor with professional software engineering and a focus on intuitive product interfaces, we believe this toolkit will prove a valuable resource for a wide range of users, including

- Hardware research and development teams
- Quantum algorithm developers & software engineers
- Students of quantum computing
- Conventional developers entering QC
- Quantum consultancies & businesses seeking to be quantum ready

Moreover, our approach to producing a specialized, highly maintainable, professionally engineered solution for quantum control will provide major benefits to the research and business communities, much like the introduction of specialist cloud security software has accelerated many aspects of cloud-service businesses.

Q-CTRL is continually rolling out new features in our product suite, responding to customer and partner requests for new capabilities tailored to their needs. Among forthcoming features will be a new framework for optimizer functionality in which a user assembles a set of predefined “building blocks” to set up their optimization problem (in code or using a visual interface); for instance this may include the incorporation of band-limits, specific constraints on control solutions, or nonlinearities.

Similarly, we are soon releasing a number of time-series analysis packages which enable the identification and extraction of system dynamics from discretized measurement records. It’s common practice in quantum computing experiments to simply average together large data sets in order to obtain probabilistic information about *e.g.* quantum-state populations in algorithms. This procedure, while common, is confounded by the presence of large-scale temporal drifts in hardware that can introduce dynamics in measurements that are not captured by simple averaging procedures. The tools we are building include features for Gaussian Process Regression and Autoregressive Kalman Filtering [18], targeting both data fitting for the removal of background dynamics and also predictive estimation for feedforward control stabilization of qubits and clocks [31]. These time-domain analytic frameworks are also useful for data fusion incorporating multiple measurement streams from sensors or measured qubits.

The most substantial development activities over the coming year will leverage the power of control engineering to produce automated and adaptive strategies for the tuneup, calibration, and optimization of mesoscale systems, moving beyond the brute-force strategy of independent calibration of all devices. In this space, advanced machine learning and robotic control concepts provide new opportunities to facilitate rapid, autonomous bring up of devices in a way that will grow in importance as system sizes increase. We already have considerable effort in this area, taking inspiration from autonomous robotic control to facilitate adaptive measurement and data inference on large qubit arrays [19, 33], and will be investing heavily in this area in the future.

## ACKNOWLEDGEMENTS

Q-CTRL efforts supported by Data Collective, Horizons Ventures, Main Sequence Ventures, Sequoia Capital (China), Sierra Ventures, and SquarePeg Capital. Development of multi-dimensional filter functions and SVD spectrum inversion technique by Q-CTRL supported by the US Army Research Office under Contract

W911NF-12-R-0012. Q-CTRL is grateful to I. Siddiqi and D. Santiago for provision of device data which inspired circuit optimization results. Experimental work using trapped ions at USYD partially supported by the ARC Centre of Excellence for Engineered Quantum Systems CE170100009, the Intelligence Advanced Research Projects Activity (IARPA) through the US Army Research Office Grant No. W911NF-16-1-0070, and a private grant from H. & A. Harley.

## Appendix A: Appendix: Technical Definitions

### 1. Fourier transform

In this paper we exclusively use the non-unitary angular-frequency convention for Fourier transform pairs, defining

$$Q(\omega) \equiv \int_{-\infty}^{\infty} dt e^{-i\omega t} Q(t) \quad (A1)$$

$$Q(t) \equiv \frac{1}{2\pi} \int_{-\infty}^{\infty} d\omega e^{i\omega t} Q(\omega) \quad (A2)$$

where  $Q(t)$  denotes any scalar-, matrix- or operator-valued function of time, and  $Q(\omega)$  is its Fourier transform, implemented element-wise for matrices. For ease of notation we reuse the same symbol and simply change the argument to distinguish time- or frequency-domain transforms. To avoid confusion we also write  $\mathcal{F}\{Q(t)\}(\omega) \equiv Q(\omega)$  and  $\mathcal{F}^{-1}\{Q(\omega)\}(t) \equiv Q(t)$ .

### 2. Frobenius inner product

For matrices  $A, B \in \mathbb{C}^{m \times n}$ , the Frobenius inner product is defined as

$$\langle A, B \rangle_F = \sum_{i,j} A_{ij}^* B_{ij} = \text{Tr}(A^\dagger B) \quad (A3)$$

### 3. Frobenius norm

The inner product in Eq. (A3) induces a matrix norm. For a matrix  $A \in \mathbb{C}^{m \times n}$ , the Frobenius norm is defined by

$$\|A\|_F = \sqrt{\langle A, A \rangle_F} = \sqrt{\sum_{i,j} |A_{ij}|^2} = \sqrt{\text{Tr}(A^\dagger A)} \quad (A4)$$

### 4. Approximations

The measure for robustness may be approximated using filter function framework. Specifically

$$\mathcal{I}_{\text{robust}} \approx \sum_{k=1}^p \mathcal{I}_{\text{robust},k} \quad (A5)$$

where

$$\mathcal{I}_{\text{robust},k} \equiv \frac{1}{2\pi} \int_{-\infty}^{\infty} S_k(\omega) F_k(\omega) d\omega \quad (A6)$$

is the contribution from the  $k$ th noise channel, expressed as an overlap integral between the noise power spectral density,  $S_k(\omega)$ , and the associated filter function  $F_k(\omega)$ .

## 5. Power spectral density

Here we develop the relationship between noise processes in the time-domain and their frequency-domain representations. Let  $\beta_k(t)$  for  $k \in \{1, \dots, n\}$  denote set of scalar-valued noise fields. Using the definition for the Fourier transform set out in App. A 1, we establish the following relationships between time- and frequency-domain variables

$$\beta_k(t) = \frac{1}{2\pi} \int_{-\infty}^{\infty} d\omega e^{i\omega t} \beta_k(\omega), \quad (\text{A7})$$

$$\beta_k(\omega) = \int_{-\infty}^{\infty} dt e^{-i\omega t} \beta_k(t). \quad (\text{A8})$$

We assume the noise fields are independent[74], zero-mean random variables. The cross-correlation functions consequently vanish, namely

$$\langle \beta_j(t_1) \beta_k^*(t_2) \rangle = 0, \quad j \neq k \in \{1, \dots, n\} \quad (\text{A9})$$

where the angle brackets denote an ensemble average over the stochastic variables. The frequency-domain variables

inherit the equivalent property, namely

$$\langle \beta_j(\omega_1) \beta_k^*(\omega_2) \rangle = 0, \quad j \neq k \in \{1, \dots, n\}, \quad (\text{A10})$$

which may be shown by substituting in Eq. (A8), and invoking Eq. (A9). We further assume the noise processes are *wide sense stationary*, implying the autocorrelation functions, defined as

$$C_k(t_2 - t_1) \equiv \langle \beta_k(t_1) \beta_k^*(t_2) \rangle, \quad i \in \{1, \dots, n\}, \quad (\text{A11})$$

depend only on the time *difference*  $\tau = t_2 - t_1$ . Under these conditions the autocorrelation function for each noise field may be related to its power spectral density  $S_i(\omega)$  using the Wiener-Khinchin Theorem [75]. Specifically,

$$C_k(t_2 - t_1) = \frac{1}{2\pi} \int_{-\infty}^{\infty} S_k(\omega) e^{i\omega(t_2 - t_1)} d\omega, \quad (\text{A12})$$

which is consistent with *defining* the power spectral density as

$$S_k(\omega) \equiv \frac{1}{2\pi} \left\langle |\beta_k(\omega)|^2 \right\rangle. \quad (\text{A13})$$

To show this observe

$$\langle \beta_k(\omega_1) \beta_k^*(\omega_2) \rangle = \left\langle \left( \int_{-\infty}^{\infty} dt_1 e^{-i\omega_1 t_1} \beta_k(t_1) \right) \left( \int_{-\infty}^{\infty} dt_2 e^{-i\omega_2 t_2} \beta_k(t_2) \right)^* \right\rangle \quad (\text{A14})$$

$$= \int_{-\infty}^{\infty} dt_1 \int_{-\infty}^{\infty} dt_2 \langle \beta_k(t_1) \beta_k^*(t_2) \rangle e^{i\omega_2 t_2} e^{-i\omega_1 t_1} \quad (\text{A15})$$

$$= \int_{-\infty}^{\infty} dt_1 \int_{-\infty}^{\infty} dt_2 \left( \frac{1}{2\pi} \int_{-\infty}^{\infty} S_k(\omega) e^{i\omega(t_2 - t_1)} d\omega \right) e^{i\omega_2 t_2} e^{-i\omega_1 t_1} \quad (\text{A16})$$

$$= \frac{1}{2\pi} \int_{-\infty}^{\infty} d\omega S_k(\omega) \int_{-\infty}^{\infty} dt_1 e^{-i(\omega + \omega_1)t_1} \int_{-\infty}^{\infty} dt_2 e^{i(\omega + \omega_2)t_2} \quad (\text{A17})$$

$$= \frac{1}{2\pi} \int_{-\infty}^{\infty} d\omega S_k(\omega) (2\pi \cdot \delta(\omega + \omega_1)) (2\pi \cdot \delta(-\omega + \omega_2)) \quad (\text{A18})$$

$$= \begin{cases} 0 & \omega_1 \neq \omega_2 \\ 2\pi S_k(\omega_1) & \omega_1 = \omega_2 \end{cases} \quad (\text{A19})$$

## Appendix B: Control Hamiltonian

As outlined in the main text, the central objectives of quantum control is to enhance the performance of a quantum system by leveraging the available controls against the influence of relevant noise sources. Delivering this for arbitrary quantum systems (qubits, qutrits, multi-qubit ensembles, etc.) requires a generalized formalism for describing the control Hamiltonian. In this appendix we introduce this formalism.

### 1. Generalized formalism

Let  $\mathcal{H}$  be a  $d$ -dimensional Hilbert space for the controlled quantum system. The control Hamiltonian is written

$$H_c(t) = \left( \sum_{j=1}^d \gamma_j(t) C_j + \text{H.C.} \right) + \sum_{l=1}^s \alpha_l(t) A_l + D \quad (\text{B1})$$

in terms of the control operators  $A_l, C_j, D \in \mathcal{H}$  and control pulses (waveforms)  $\alpha_l(t) \in \mathbb{R}$  and  $\gamma_j(t) \in \mathbb{C}$ . To unpack this notation we introduce the nomenclature of *drives*, *shifts* and *drifts*, useful for mapping generalized quantum control concepts to common physical control variables. These are detailed in [Table VI](#). In this framework, system evolution under  $H_c$  may be viewed as a combination of generalized rotations, driven by control pulses (real or complex) about effective *control axes*, defined by the associated operators.

control term	operator	pulse	
drive	$C_j$	non-Hermitian	$\gamma_j(t)$ $\mathbb{C}$ : complex
shift	$A_l$	Hermitian	$\alpha_l(t)$ $\mathbb{R}$ : real
drift	$D$	Hermitian	-
	<i>symbol</i>	<i>type</i>	<i>symbol</i> <i>type</i>

TABLE VI. Decomposition of control Hamiltonian into generalized drive, shift and drift terms. Drive terms are defined by non-Hermitian operators,  $C_j \neq C_j^\dagger$ , and complex-valued control pulses  $\gamma_j(t)$ . Shift terms are defined by Hermitian operators,  $A_l = A_l^\dagger$ , and real-valued control pulses  $\alpha_l(t)$ . The operator  $D$  is a time-independent Hermitian operator, which we refer to as the drift Hamiltonian.

### 2. Control solutions

Assuming the operator basis defined above, the control Hamiltonian may be expressed more compactly as

$$H_c(t) = (\boldsymbol{\gamma}(t)\mathbf{C} + \text{H.C.}) + \boldsymbol{\alpha}(t)\mathbf{A} + D \quad (\text{B2})$$

in terms of the vectorized objects defined by

$$\text{drive terms: } \boldsymbol{\gamma}(t) = [\gamma_1(t), \gamma_2(t), \dots, \gamma_d(t)], \quad \mathbf{C} = \begin{bmatrix} C_1 \\ C_2 \\ \vdots \\ C_d \end{bmatrix}, \quad t \in [0, \tau] \quad (\text{B3})$$

$$\text{shift terms: } \boldsymbol{\alpha}(t) = [\alpha_1(t), \alpha_2(t), \dots, \alpha_s(t)], \quad \mathbf{A} = \begin{bmatrix} A_1 \\ A_2 \\ \vdots \\ A_s \end{bmatrix}, \quad t \in [0, \tau] \quad (\text{B4})$$

with drive and shift pulses listed as complex and real row vectors respectively, and corresponding drive and shift operators listed as column vectors. Given the operator-basis defined by  $\mathbf{A}$  and  $\mathbf{C}$ , the most general description of control is therefore specified by the set of functions  $\boldsymbol{\alpha}(t)$  and  $\boldsymbol{\gamma}(t)$ , defined on the time interval  $t \in [0, \tau]$ , defining the duration over which the control is applied. We refer to this structure as a *control solution*.

### 3. Control segments

It is often more useful to specify the form of the control Hamiltonian, or functional form of the control pulses  $\boldsymbol{\gamma}(t)$  and  $\boldsymbol{\alpha}(t)$ , locally in time. In this case the time-domain  $t \in [0, \tau]$  is partitioned into a series of intervals, or segments. The functional form of the control pulses are then defined on each segment. This is illustrated below for a shift pulse  $\alpha_j(t)$ . The time domain  $t \in [0, \tau]$  has been formally partitioned into  $m$  subintervals

$$[t_{i-1}, t_i], \quad i \in \{1, \dots, m\}, \quad t_0 \equiv 0, \quad t_m \equiv \tau \quad (\text{B5})$$

where  $t_{i-1}$  and  $t_i$  are respectively the start and end times of the  $i$ th segment, and

$$\tau_i = t_i - t_{i-1} \quad (\text{B6})$$

is its duration. The shift pulse  $\alpha_j(t)$  is piecewise-constant, defined to take the constant value  $\alpha_{i,j}$  on the  $i$ th segment,  $t \in [t_{i-1}, t_i]$ .

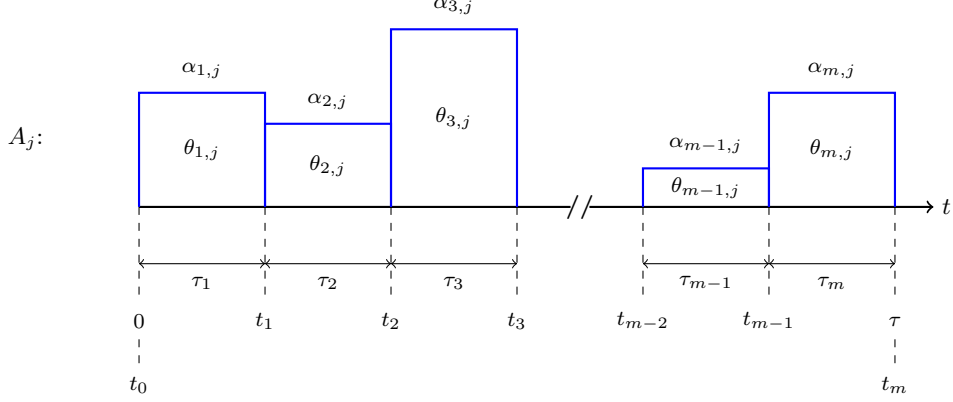


FIG. 16. Segmentation of control amplitude  $\alpha_j(t)$  for control axis  $A_j$  into  $m$  segments. The area under the  $i$ th segment is given by the variable  $\theta_{i,j} \equiv \alpha_{i,j}\tau_j$ .

#### 4. Control coordinates

Here we introduce notation conventions followed by Q-CTRL to define drive pulses, their decomposition, and their relationship to Hermitian and non-Hermitian control operators. Since the following structure applies to every pulse-operator pair  $(\gamma_j(t), C_j)$ , we drop the subscript  $j$  for simplicity. The complex-valued pulse  $\gamma(t) \in \mathbb{C}$  may be written in polar or Cartesian form. Namely,

$$\text{Polar form:} \quad \gamma(t) = \Omega(t)e^{+i\phi(t)} \quad (\text{B7})$$

$$\text{Cartesian form:} \quad \gamma(t) = I(t) + iQ(t) \quad (\text{B8})$$

allowing us establish the following control forms

$$\text{modulus:} \quad \Omega(t) = |\gamma(t)| \quad (\text{B9})$$

$$\text{phase:} \quad \phi(t) = \text{Arg}(\gamma(t)) \quad (\text{B10})$$

$$\text{in-phase:} \quad I(t) = \text{Re}(\gamma(t)) = \Omega(t) \cos(\phi(t)) \quad (\text{B11})$$

$$\text{in-quadrature:} \quad Q(t) = \text{Im}(\gamma(t)) = \Omega(t) \sin(\phi(t)) \quad (\text{B12})$$

where the drive phase  $\phi(t) = +\text{Arg}(\gamma(t))$  is defined as the *positive* argument. The drive term in the control Hamiltonian is therefore expressed

$$\gamma(t)C + \text{H.C.} = \gamma(t)C + \gamma^*(t)C^\dagger \quad (\text{B13})$$

$$= (I(t) + iQ(t))C + (I(t) - iQ(t))C^\dagger \quad (\text{B14})$$

$$= I(t)(C + C^\dagger) + Q(t)(iC - iC^\dagger) \quad (\text{B15})$$

$$= I(t)A_I + Q(t)A_Q \quad (\text{B16})$$

where we have defined the *Hermitian* operators

$$A_I = C + C^\dagger, \quad A_Q = i(C - C^\dagger). \quad (\text{B17})$$

Each drive term therefore decomposes into a pair of shift-terms  $(I(t), A_I)$  and  $(Q(t), A_Q)$  in the familiar form of quadrature controls. These are related to the non-Hermitian operator as

$$C = \frac{1}{2}(A_I - iA_Q) \quad (\text{B18})$$

The *modulus*  $\Omega(t)$  sets the rotation rate, while the *phase*  $\phi(t)$  sets the direction of rotation, oriented between the control axes defined by  $(A_I, A_Q)$ .

## Appendix C: Multidimensional filter function derivations

### 1. Magnus expansion

The first few Magnus terms are computed as [50, 51]

$$\Phi_1(\tau) = \int_0^\tau dt \tilde{H}_{\text{err}}(t) \quad (\text{C1})$$

$$\Phi_2(\tau) = -\frac{i}{2} \int_0^\tau dt_1 \int_0^{t_1} dt_2 [\tilde{H}_{\text{err}}(t_1), \tilde{H}_{\text{err}}(t_2)] \quad (\text{C2})$$

$$\Phi_3(\tau) = \frac{1}{6} \int_0^\tau dt_1 \int_0^{t_1} dt_2 \int_0^{t_2} dt_3 [\tilde{H}_{\text{err}}(t_1), [\tilde{H}_{\text{err}}(t_2), \tilde{H}_{\text{err}}(t_3)]] + [\tilde{H}_{\text{err}}(t_3), [\tilde{H}_{\text{err}}(t_2), \tilde{H}_{\text{err}}(t_1)]] \quad (\text{C3})$$

⋮

The Magnus series establishes a framework to define error *cancellation order*. Implementing a control with fidelity defined in Eq. (17) up to order  $\alpha$  means choosing controls such that  $\Phi_k(\tau) \approx 0$  for all  $k \leq \alpha$ . Below we describe a useful framework for computing the  $\Phi_\alpha(\tau)$  in the Fourier domain using filter functions.

### 2. Spectral representation of Magnus term

Here we derive the frequency-domain form for the leading-order Magnus term in Eq. (29). Using the definition for the Fourier transform set out in App. A 1, we have

$$\beta_k(t) = \frac{1}{2\pi} \int_{-\infty}^{\infty} d\omega e^{i\omega t} \beta_k(\omega), \quad (\text{C4})$$

$$N'_k(t) = \frac{1}{2\pi} \int_{-\infty}^{\infty} d\omega e^{i\omega t} N'_k(\omega). \quad (\text{C5})$$

Substituting into Eq. (28) we therefore obtain

$$\Phi_1(\tau) = \sum_{k=1}^p \int_{-\infty}^{\infty} dt \left( \frac{1}{2\pi} \int_{-\infty}^{\infty} d\omega_1 e^{i\omega_1 t} N'_k(\omega_1) \right) \left( \frac{1}{2\pi} \int_{-\infty}^{\infty} d\omega_2 e^{i\omega_2 t} \beta_k(\omega_2) \right) \quad (\text{C6})$$

$$= \left( \frac{1}{2\pi} \right)^2 \sum_{k=1}^p \int_{-\infty}^{\infty} d\omega_1 \int_{-\infty}^{\infty} d\omega_2 N'_k(\omega_1) \beta_k(\omega_2) \int_{-\infty}^{\infty} dt e^{i\omega_1 t} e^{i\omega_2 t} \quad (\text{C7})$$

$$= \left( \frac{1}{2\pi} \right)^2 \sum_{k=1}^p \int_{-\infty}^{\infty} d\omega_1 \int_{-\infty}^{\infty} d\omega_2 N'_k(\omega_1) \beta_k(\omega_2) \cdot 2\pi \delta(-\omega_2 - \omega_1) \quad (\text{C8})$$

where  $\delta(x)$  is the Dirac delta function. Consequently

$$\Phi_1(\tau) = \frac{1}{2\pi} \sum_{k=1}^p \int_{-\infty}^{\infty} d\omega_2 N'_k(-\omega_2) \beta_k(\omega_2) \quad (\text{C9})$$

$$= \frac{1}{2\pi} \sum_{k=1}^p \int_{-\infty}^{\infty} d\omega G_k(\omega) \beta_k(\omega) \quad (\text{C10})$$

where we have defined

$$G_k(\omega) \equiv N'_k(-\omega) \equiv \int_{-\infty}^{\infty} dt e^{i\omega t} N'_k(t). \quad (\text{C11})$$

### 3. Leading order robustness infidelity

The leading-order error action operator [Eq. \(26\)](#) may be Taylor expanded as

$$\tilde{U}_{\text{err}}(\tau) = \mathbb{I} - i\Phi_1 - \frac{1}{2}\Phi_1^2 + \dots \quad (\text{C12})$$

$$= \mathbb{I} - i\Phi_1 - \frac{1}{2}\Phi_1\Phi_1^\dagger + \dots \quad (\text{C13})$$

where we have used the property that the Magnus terms are Hermitian. Substituting into [Eq. \(17\)](#) the leading order contribution to the robustness fidelity takes the form

$$\mathcal{F}_{\text{robust}}(\tau) = \left\langle \left| \frac{1}{\text{Tr}(P)} \text{Tr} \left( P \left\{ \mathbb{I} - i\Phi_1 - \frac{1}{2}\Phi_1\Phi_1^\dagger + \dots \right\} \right) \right|^2 \right\rangle \quad (\text{C14})$$

$$\approx \left\langle \left| \frac{1}{\text{Tr}(P)} \left\{ \text{Tr}(P) - i\text{Tr}(P\Phi_1) - \text{Tr} \left( \frac{1}{2}P\Phi_1\Phi_1^\dagger \right) \right\} \right|^2 \right\rangle. \quad (\text{C15})$$

Due to our choice of gauge transformation in [Eq. \(25\)](#), we additionally use the property that  $\text{Tr}(P\Phi_1) = 0$ , yielding

$$\mathcal{F}_{\text{robust}}(\tau) = \left\langle \left| 1 - \frac{1}{\text{Tr}(P)} \text{Tr} \left( \frac{1}{2}P\Phi_1\Phi_1^\dagger \right) \right|^2 \right\rangle \quad (\text{C16})$$

$$= \left\langle \left[ 1 - \frac{1}{\text{Tr}(P)} \text{Tr} \left( \frac{1}{2}P\Phi_1\Phi_1^\dagger \right) \right]^* \left[ 1 - \frac{1}{\text{Tr}(P)} \text{Tr} \left( \frac{1}{2}P\Phi_1\Phi_1^\dagger \right) \right] \right\rangle \quad (\text{C17})$$

$$= \left\langle 1 - \frac{2}{\text{Tr}(P)} \text{Tr} \left( \frac{1}{2}P\Phi_1\Phi_1^\dagger \right) + \mathcal{O}(|\Phi_1|^4) \right\rangle \quad (\text{C18})$$

where the last line uses the result that  $\text{Tr}(P\Phi_1\Phi_1^\dagger)$  is real-valued, following from the Hermiticity of  $\Phi_1$ . Ignoring terms beyond  $\mathcal{O}(|\Phi_1|^2)$ , and observing the ensemble average over noise-realizations only affects terms dependent on  $\Phi_1$ , we therefore obtain

$$\mathcal{I}_{\text{robust}}(\tau) = 1 - \mathcal{F}_{\text{robust}}(\tau) \quad (\text{C19})$$

$$\approx \frac{2}{2\text{Tr}(P)} \left\langle \text{Tr} \left( P\Phi_1\Phi_1^\dagger \right) \right\rangle \quad (\text{C20})$$

$$= \frac{1}{\text{Tr}(P)} \text{Tr} \left( P \left\langle \Phi_1\Phi_1^\dagger \right\rangle \right). \quad (\text{C21})$$

### 4. Leading-order filter functions

Substituting [Eq. \(29\)](#) into [Eq. \(27\)](#) we obtain

$$\left\langle \Phi_1(\tau)\Phi_1^\dagger(\tau) \right\rangle = \sum_{i=1}^p \sum_{j=1}^p \left( \frac{1}{2\pi} \right)^2 \int_{-\infty}^{\infty} d\omega_1 \int_{-\infty}^{\infty} d\omega_2 G_i(\omega_1) G_j^\dagger(\omega_2) \langle \beta_i(\omega_1) \beta_j^*(\omega_2) \rangle \quad (\text{C22})$$

$$= \sum_{k=1}^p \left( \frac{1}{2\pi} \right)^2 \int_{-\infty}^{\infty} d\omega_1 \int_{-\infty}^{\infty} d\omega_2 G_k(\omega_1) G_k^\dagger(\omega_2) \langle \beta_k(\omega_1) \beta_k^*(\omega_2) \rangle \quad (\text{C23})$$

$$= \sum_{k=1}^p \frac{1}{2\pi} \int_{-\infty}^{\infty} d\omega G_k(\omega) G_k^\dagger(\omega) S_k(\omega) \quad (\text{C24})$$

where in the second line we invoke the independence property of the frequency-domain variables  $\beta_{i,j}(\omega)$  defined by Eq. (A10), and in the third line we use Eq. (A19). Substituting into Eq. (27) we therefore obtain

$$\mathcal{I}_{\text{robust}}(\tau) \approx \sum_{k=1}^p \int_{-\infty}^{\infty} \frac{d\omega}{2\pi} \left\{ \frac{1}{\text{Tr}(P)} \text{Tr} \left( PG_k(\omega) G_k^\dagger(\omega) \right) \right\} S_k(\omega) \quad (\text{C25})$$

## Appendix D: Technical details on implementation of the SVD noise reconstruction

In this appendix we provide additional technical details pertaining to our implementation of the SVD noise reconstruction algorithm.

### 1. Measurement uncertainties for SVD reconstruction

All quantities captured in Eq. (56) must be estimated in order to perform a computationally valid spectral estimate. Formally,  $\mathcal{I}^{(j)}$  is the expectation value over a probability density function dependent on all  $p$  noise PSDs, and the  $j$ th control protocol. An estimate may be obtained from experiment by averaging over a set of measured infidelities obtained from repeated application of the  $j$ th control protocol. We denote these estimates as  $\hat{I}^j \pm \Delta\hat{I}^j$ , where  $\Delta\hat{I}^j$  denotes the experimental uncertainty, *e.g.* estimated via the standard error.

In principle, the uncertainties  $\Delta\hat{S}^{k,\ell}$  will have contributions from the uncertainties both in  $\hat{F}_{k,\ell}^j$  and in  $\mathcal{I}^{(j)}$ . Since  $\hat{F}_{k,\ell}^j$  are calculated directly from the knowledge of the set of controls and noise operators, their uncertainties stem from numerical errors. In what follows, we neglect these contributions and consider only the dominant statistical error coming from the measured infidelities. Under this assumption, the solution for the uncertainties  $\Delta\hat{S}^{k,\ell}$  can be obtained straightforwardly from the knowledge of the covariance matrix for  $\hat{\mathbf{I}}$ , namely

$$\hat{\Sigma}_I = \text{diag}(\hat{\sigma}_{I,1}^2, \hat{\sigma}_{I,2}^2, \dots, \hat{\sigma}_{I,c}^2), \quad (\text{D1})$$

where  $\hat{\sigma}_{I,j}$  is the standard deviation for the measured infidelity subjected to the control sequence  $j$ . Using Eq. (68), we can write the covariance matrix for  $\hat{S}$  as

$$\hat{\Sigma}_S = \mathbf{V}\mathbf{D}^+\mathbf{U}^\dagger \hat{\Sigma}_I \mathbf{U}\mathbf{D}^+\mathbf{V}^\dagger, \quad (\text{D2})$$

and obtain the individual standard deviations explicitly as the square root of its diagonal elements

$$\hat{\sigma}_{S,k} = \sqrt{\text{diag}(\hat{\Sigma}_S)_k}. \quad (\text{D3})$$

### 2. Filter function normalization

For a system of multiple noise sources, the SVD of the raw filter functions,  $\hat{\mathbf{F}}$ , may present two issues. First, all

filter functions in the matrix  $\hat{\mathbf{F}}$  must have the same units, otherwise the SVD transformation would be invalid. The second issue is that different filter functions in the matrix  $\hat{\mathbf{F}}$  (corresponding to, in principle, controls of widely varying lengths or amplitudes), can differ in scale by orders of magnitude. In this case, the singular values will also present large variations, affecting the stability of the inversion process.

To account for these scenarios, we normalize the filter functions prior to performing the SVD. We define a  $c \times c$  diagonal scaling matrix

$$\{\mathbf{G}\}_{i,j} = \delta_{i,j} \sqrt{\sum_{k,l} |\hat{F}_{k,l}^j|^2}, \quad (\text{D4})$$

which quantifies the strength of the filter functions for the  $j$ -th control, as it sums up the contributions for all noise channels and frequencies, represented by indices  $k$  and  $l$ , respectively. We then use this scaling factor to define a dimensionless filter-function matrix  $\tilde{\mathbf{F}}$ :

$$\tilde{\mathbf{F}} = \mathbf{G}^{-1} \hat{\mathbf{F}}. \quad (\text{D5})$$

Given the SVD of this matrix:

$$\tilde{\mathbf{F}} = \mathbf{U}\mathbf{D}\mathbf{V}^\dagger, \quad (\text{D6})$$

we can write the original filter function matrix as

$$\hat{\mathbf{F}} = \mathbf{G}\mathbf{U}\mathbf{D}\mathbf{V}^\dagger. \quad (\text{D7})$$

The reconstruction solution given by Eq. (68) then becomes

$$\hat{\mathbf{S}} = \mathbf{V}\mathbf{D}^+\mathbf{U}^\dagger \mathbf{G}^+ \hat{\mathbf{I}}, \quad (\text{D8})$$

where, as before, a matrix  $\mathbf{A}^+$  corresponds to a diagonal matrix with entries  $1/A_i$  for all non-zero  $A_i$ , and zero otherwise.

### 3. Calculating weights due to sensitivity

One of the important issues with the reconstruction procedure is to ensure that the frequency range where the PSD to be reconstructed is appreciable is also well covered by the filter functions used in the inversion procedure. This means that the predictions for the noise PSD will diminish in relevance when the filter function sensitivity in a given frequency region is close to zero. In

order to capture this, we introduce an additional variable called a weight associated with each element in the noise predictor. We employ these weights in order to identify spectral regions where the validity of the SVD breaks down and uncertainties in the returned estimates become large.

The weights are defined as the sum of all  $c$  filter functions for a given noise  $k$ , normalized by their maximum value:

$$\{\mathbf{w}\}_k = \frac{\sum_{j,l} \{\hat{\mathbf{F}}\}_{k,l}^j}{\max_k (\sum_{j,l} \{\hat{\mathbf{F}}\}_{k,l}^j)}. \quad (\text{D9})$$

#### 4. Singular value truncation to prevent numeric instability

When the system of linear equations is over-determined, depending on the condition of the matrix  $\hat{\mathbf{F}}$ , the SVD reconstruction method can become numerically unstable. Intuitively, when some singular values of  $\hat{\mathbf{F}}$  are small, they introduce instability in the matrix pseudo-inverse as their inverses diverge.

To mitigate this, we truncate the singular values with a preset threshold  $\chi$ . The appropriate value of this preset threshold can be found by the following heuristic: For each experiment, run the circuits multiple times and reconstruct the noise spectrum using the measured results. The threshold of the singular values is set to be the value such that the reconstructed noise spectra from different converge within uncertainties, prior to the onset of potential numeric instability.

Suppose that  $\hat{\mathbf{F}}$  is a  $n \times m$  matrix, with  $n < m$ . Suppose the singular values in  $\mathbf{D}$  are ordered in the descending order such that the  $i+1$ -th entry of  $\mathbf{D}$  is less than  $\chi$ . Let  $\mathbf{D}'$  denotes the  $n \times m$  diagonal matrix obtained from  $\mathbf{D}$  with the  $i+1, \dots, n$  diagonal elements set to be zero. Then the SVD of the truncated filter function matrix is  $\hat{\mathbf{F}}' = \mathbf{U} \mathbf{D}' \mathbf{V}^*$ . We then use the truncated  $\hat{\mathbf{F}}'$  to perform the pseudo-inverse.

The last essential issue in the numerical reconstruction is the distribution of singular values in the decomposition of  $\mathbf{F}$ . Significant numerical instability can arise when the smallest singular value is *much* smaller than the largest one. This is due to the inversion in the reconstruction:

$$\hat{\mathbf{S}} = \mathbf{V} \mathbf{D}^+ \mathbf{U}^* \mathbf{G}^+ \hat{\mathbf{I}}. \quad (\text{D10})$$

If the ratio  $D_{\max}/D_{\min}$  between the maximum and minimum singular values, known as the *condition number*, is very large, then any noise in  $\hat{\mathbf{I}}$  will be strongly amplified, leading to a numerically unstable inversion process. To avoid this issue, we implement a truncation by considering only the first  $T_D$  values in  $\mathbf{D}$ . Using the truncated matrix  $\mathbf{D}_T$ , the estimation of the PSD is given by:

$$\hat{\mathbf{S}} = \mathbf{V} \mathbf{D}_T^+ \mathbf{U}^* \mathbf{G}^+ \hat{\mathbf{I}} \quad (\text{D11})$$

$$\hat{\mathbf{\Sigma}}_S = \mathbf{G}^* \mathbf{V} \mathbf{D}_T^+ \mathbf{U}^* \hat{\mathbf{\Sigma}}_I \mathbf{U} \mathbf{D}_T^+ \mathbf{V}^* \mathbf{G}^+. \quad (\text{D12})$$

We have implemented three different methods to select the truncation number  $T_D$  that are available when calling the reconstructor:

- Ratio-based truncation: The user can specify a truncation ratio  $r_T$  corresponding to the ratio between the maximum and minimum (truncated) singular values.  $T_D$  is the number of singular values that satisfy the specified ratio, that is,  $D_1/D_{T_D} < r_T$ .
- Fixed truncation: In this method, the user can specify the exact number  $T_D$  of singular values to be used for estimating noise PSD.
- Entropy truncation: In this method we estimate the truncation number  $T_D$  based on the entropy of the singular values defined as

$$H_D = - \sum_i \overline{D}_i \log_2(\overline{D}_i), \quad (\text{D13})$$

with  $\overline{D}_i = \frac{D_i}{\sum_j D_j}$ . Note that the entropy assumes that singular values that are zero have already been ignored, consistently with the use of  $D^+$  in the solution of the inversion problem. The number of orthogonal linearly independent vectors can then be estimated using the entropy. This is done in the standard way in which the information is estimated from the entropy, that is, by defining

$$\hat{N}_D = 2^{H_D}. \quad (\text{D14})$$

This provides a real number that quantifies the number of linearly independent vectors that the transformation captures. In order to get an integer truncation number, we define it as being the floor of  $\hat{N}_D$ , *i.e.*,  $T_D = \lfloor \hat{N}_D \rfloor$ .

## Appendix E: Methods for experimental demonstrations of quantum control benefits

### 1. Quasi-static error robustness

In Fig. 10b,c we demonstrate the robustness of various dynamically corrected gate protocols implementing a net  $\pi_X$  rotation to quasistatic errors in both the rotation angle and qubit frequency. For this demonstration, a single trapped ion qubit is prepared in  $|0\rangle$ , 10 microwave  $\pi$ -rotations are applied, and the difference between the final and target qubit states is measured. The measured quantity  $p_{|1\rangle}$  is the probability of finding the qubit in  $|1\rangle$ ; it can be considered as the sequence infidelity,  $\mathcal{I}$ , returning zero for error-free rotations. Four different pulse constructions are utilized: primitive gates (red), BB1 (purple), CORPSE (cyan), and reduced CinBB (blue).

In Fig. 10b, an over-rotation control error is engineered by scanning the pulse length around the appropriately tuned value. A sequence of 10  $\pi$ -rotations about the  $+X$  axis is applied for each error strength; this sequence amplifies the effect of over-rotation errors. In Fig. 10c, an engineered off-resonance error is created using an offset between the frequency of the qubit and that of the microwave drive. The absolute frequency detuning is normalized by the Rabi rate to quantify a relative error that is varied between  $\pm 10\%$ . To amplify the effect of the off-resonance error, the 10  $\pi$ -rotations are alternated between the  $+X$  and  $-X$  axes.

## 2. Suppression of time-varying noise

The experimental filter function reconstructions shown in Fig. Fig. 10d,e in the main text were performed through the application of a single frequency disturbance at  $\omega_{\text{sid}}$  added to either the control or the dephasing quadrature. We denote these time-dependent noise fields with  $\beta_k(t)$  with  $k \in \{\Omega, z\}$  and our corresponding Hamiltonian reads

$$H(t) = H_C(t)(1 + \beta_\Omega(t)) + \beta_z(t)\sigma_z, \quad (\text{E1})$$

where  $H_C(t)$  is the control Hamiltonian that represents the driven evolution through the microwave field,  $\beta_\Omega(t)$  is the amplitude noise and  $\beta_z(t)$  is the dephasing noise. Typically, we write  $H_C(t)$  in a rotating frame with respect to the qubit splitting such that it takes the form of a time-dependent  $x$ - or  $y$ -rotation with

$$H_C(t) = \frac{\Omega(t)}{2}(\cos \phi(t)\sigma_x + \sin \phi(t)\sigma_y), \quad (\text{E2})$$

where  $\Omega(t)$  is the time-dependent Rabi rate and  $\phi(t)$  is the control phase (see [72] for further details on the experimental system and the control synthesis). The noise fields take the explicit form of

$$\beta_k(t) = \alpha_k \cos(\omega_{\text{sid}}t + \varphi), \quad \text{for } k \in \{\Omega, z\}, \quad (\text{E3})$$

where  $\alpha_k$  is a constant factor to set the modulation depth. Through averaging over phase parameter  $\varphi \in \{0, 2\pi\}$ , this form of modulation produces a  $\delta$ -function like noise spectrum  $S_k(\omega) \approx \delta(\omega - \omega_{\text{sid}})$  which, using the relationship  $\chi \propto \int d\omega S(\omega)F(\omega)$  (cf. XXX), allows us to directly extract the value of the filter function at the frequency  $\omega_{\text{sid}}$  [17, 72]. For the experiments here, we used  $\alpha_\Omega = 0.25$  and  $\alpha_z = 0.7$  and the points were averaged over 5 values of  $\varphi$  spaced linearly between 0 and  $2\pi$ .

Experimentally, this is achieved via amplitude and frequency modulation of the microwave field that drives the qubit transition. The amplitude noise is added digitally to the I/Q control waveforms before upload to the microwave signal generator (Keysight E8267D), such that we obtain a noisy drive waveform with  $\Omega(t) \rightarrow \Omega(t)(1 +$

$\beta_\Omega(t))$ . The dephasing noise is engineered through an additive term in the phase of the control Hamiltonian (Equation E2), such the total phase component gets split into a control and noise term:  $\phi(t) \rightarrow \phi_C(t) + \phi_N(t)$ . A frame transformation with respect to this dephasing noise term via  $e^{i\phi_N(t)\sigma_z/2}H_C(t)e^{-i\phi_N(t)\sigma_z/2} - \frac{\dot{\phi}_N(t)\sigma_z}{2}$  yields

$$H(t) = -\frac{\Omega(t)(1 + \beta_\Omega(t))}{2}(\cos \phi(t)\sigma_x + \sin \phi(t)\sigma_y) - \frac{\dot{\phi}_N(t)\sigma_z}{2}. \quad (\text{E4})$$

Using our notation from Equation E1, we can identify the dephasing noise term  $\beta_z(t) = \dot{\phi}_N(t)/2$ . The corresponding dephasing noise waveforms are generated using an external arbitrary waveform generator (Keysight 33600A), whose output is fed into the analog FM port of the microwave generator, which produces the desired dephasing noise term. For more details, see chapter 2 in [72].

## 3. Error homogenization characterized via 10-qubit parallel randomized benchmarking

In Fig. 10f, we measure a spatially varying average error rate along a string of 10 trapped ion qubits (shown in Fig. 10f inset). In this system, ions are simultaneously addressed by a global microwave control field to drive global single-qubit rotations. However, due to a gradient in the strength of the microwave field, the qubits rotate with a spatially varying Rabi rate meaning that the control cannot be synchronously calibrated for all 10 qubits. Qubit 1 in the figure is used for calibration in this experiment, yielding the lowest error rate.

Error is measured using parallel randomized benchmarking in which all ions are illuminated with microwaves simultaneously and experience the same RB sequence. The general approach to RB sequence construction and experimental implementation is described in detail in the supplemental material of Ref. [38]. Sequences here are composed of up to 500 operations selected from the Clifford set. Measurement is conducted using a spatially resolved EMCCD camera in order to extract average error rates for each individual qubit. Given the relatively low quantum efficiency of this detection method, SPAM errors are in the range of  $\sim 3 - 5\%$ , approximately an order of magnitude higher than achieved using single-qubit RB, as measured via an avalanche photodetector.

## 4. Molmer-Sørensen drift measurements

In Fig. 10g-i, we compare two different constructions of phase-modulated two-qubit Mølmer-Sørensen gates, both designed to produce the entangled Bell state

$(|00\rangle - i|11\rangle)/\sqrt{2}$ . The gates are implemented by illuminating two ions with a pair of orthogonal beams from a pulsed laser near 355 nm, driving stimulated Raman transitions as described in [52]. The geometry of the beams enables coupling to the radial motional modes of the ions, which have approximate frequencies  $\omega_k/2\pi = (1.579, 1.498, 1.485, 1.398)$  MHz and are denoted from highest to lowest frequency by  $k = 1$  to  $k = 4$ . One of the Raman beams is controlled by an acousto-optic modulator driven by a two-tone radio-frequency signal produced by an arbitrary waveform generator. This results in a bichromatic light field that off-resonantly drives the red and blue sideband transitions, creating the state-dependent force used in the gate. We modulate the phase of the driving force  $\phi(t)$  by adjusting the phase difference between the red and blue frequency components,  $\phi(t) = [\phi_b(t) - \phi_r(t)]/2$ .

After an initial calibration of the mode frequencies and gate Rabi frequency, we repeatedly perform the entangling operations over a period of several hours without further calibration, alternating between the two different phase-modulated gate constructions (panel g vs i) in order to mitigate any systematic differences between measurements. The ions are optically pumped to  $|00\rangle$  and the selected gate is performed by applying the Raman beams for a duration of 500  $\mu$ s. For both constructions, the gate detuning set to -2 kHz from the  $k = 2$  mode. In this configuration, only the  $k = 2$  and  $k = 3$  modes are significantly excited during the operation. Each gate is repeated 500 times and the ion fluorescence measured after each repetition. We use a maximum likelihood procedure described in [52] to extract the state populations  $P_n$ , the probability of measuring  $n$  ions bright, for each set of repetitions.

The first phase-modulated gate construction consists of four phase segments and is calculated to ensure modes  $k = 2$  and  $k = 3$  are de-excited at the conclusion of the operation. The second is calculated to provide additional robustness to low frequency noise affecting the closure of mode  $k = 2$ , which necessitates doubling the number of phase segments as per the analytic procedure outlined in [52].

The required gate Rabi frequencies are  $\Omega = 2\pi \times 18.3$  kHz and  $\Omega = 2\pi \times 22.9$  kHz, for the first and second gates, respectively. The laser amplitude required to produce the desired  $\Omega$  for a particular gate construction is calibrated by fixing the amplitude of the single-tone Raman beam and varying the amplitude of the bichromatic beam. As the amplitude of the beam is increased, the populations  $P_0$  and  $P_2$  will converge to the point at which  $P_0 = P_2 \approx 0.5$ , indicating the creation of the Bell state and the correct laser amplitude.

## Appendix F: Product Features Summary

This appendix provides a concise summary of key product features in the Q-CTRL product suite. Additional in-

formation is available from <https://q-ctrl.com/products>.

### 1. BLACK OPAL

- Evaluate and select error-robust controls from a library in order to address specific noise-mitigation challenges.
- Use machine-learning optimization packages to generate tailored error-robust control solutions for custom hardware.
- Characterize noise in your hardware using qubits as transducers and custom spectrum reconstruction packages
- Perform error budgeting for in-built or custom uploaded controls using the filter-function framework
- Build intuition through advanced visualization modules to explore the impact of noise on quantum operations, and how control can mitigate error
- Access dedicated preconfigured workspaces and control libraries for single-qubit gates, two-qubit gates for superconducting circuits (cross-resonance and parametric drive) and trapped ions (Molmer-Sorensen), and noise characterization.
- Output control solutions in machine-ready formats such as CSV and JSON for upload to laboratory instrumentation or cloud based hardware.

### 2. BOULDER OPAL

The python package provides (via current and forthcoming features):

- Create numerically optimized error-robust controls for arbitrary high-dimensional quantum systems that suppress various error channels including dephasing, crosstalk, and leakage. Incorporate real experimental constraints on maximum power or control bandwidth.
- Simulate individual gates through to full circuits in the presence of realistic *colored* noise spectra (e.g.  $1/f$ ) to capture drift and non-Markovian noise dynamics.
- Verify and compare the error-robustness of any control, including optimized controls and controls created by other means and uploaded for analysis. Probe error robustness through direct calculation of quasistatic-error susceptibility and filter functions to illustrate time-varying noise susceptibility.
- Characterize noise in hardware through tailored qubit measurements to reconstruct noise spectra in different channels

- Calibrate control hardware to account for nonlinearities in modulators, finite band limits, and distortions induced by transmission lines.
- Discover and eliminate drifts and other system instabilities through time-series analyses of measurement records
- Automate control calibration and noise characterization through scripting routines integrated directly with experimental control software.

### 3. OpenControls

- Access a detailed open-source library of error-robust control solutions in a simple python module.
- Format controls directly for integration into dominant quantum programming frameworks including Qiskit, Cirq, and Pyquil. Modules exist for outputting controls directly formatted as circuits for each language.
- Integrate standard controls into programming workflows for circuit analysis incorporating Q-CTRL and custom python libraries.

### 4. Devkit

- Build deterministic robustness to noise into compiled quantum circuits using the physics of coherent averaging. Use optimization tools to find logically identical compilations which improve robustness against various error channels.
- Rapidly discriminate between logically identical circuit compilations using high-dimensional filter functions to understand relative susceptibility to error of nominally identical circuit compilations. Error channels include general common-mode dephasing, local perturbations, crosstalk, etc.
- Create hybrid circuits combining low-level robust controls on circuit subspaces with general circuit-level compilation. Optimize low-level circuit blocks at the analog layer and optimally compile for circuit-level error robustness [76, 77]. Tools are based on a custom singular-value-decomposition framework which allows efficient separation of optimization tasks between sub-blocks within a circuit.

### Appendix G: BLACK OPAL Visualizations of noise and control in quantum circuits

Q-CTRL provides an advanced visual interface that enables users to compose quantum circuits (Figs. 17(a) and 4(a)) and interactively track state evolution subject

using Bloch spheres and a visual representation of entanglement based on *correlation tetrahedra*. These tools offer unique, interactive, 3-dimensional visualizations, assisting users to build intuition for key logical operations performed in quantum circuits.

In our tools, an arbitrary sequence of single and multiqubit operations may be graphically composed or sequenced in python. The associated state evolution is calculated and displayed using interactive three.js objects. These may then be rendered in Q-CTRL products, or directly embedded in Jupyter notebooks or websites. Current visualization packages are limited to two-qubit subspaces, with forthcoming development expanding to larger circuits.

As an example consider the time-domain evolution of the state of a single qubit subject to control. A series of gates is described by an ideal target Hamiltonian:

$$H_{\text{tot}} = \frac{1}{2}\Omega(\cos(\phi)\sigma_x + \sin(\phi)\sigma_y) + \frac{1}{2}\Delta\sigma_z, \quad (\text{G1})$$

where,  $\Omega$  is the Rabi rate,  $\Delta$  the detuning and  $\sigma_{x,y,z}$  are the standard Pauli matrices. Depicted in Fig. 17(b) is a snapshot of the state vector evolution (purple pointer, Fig. 17(b)) along its present trajectory (solid red line, Fig. 17(b)) given by the last Hadamard gate (highlighted through a dynamic indicator). The visualization is dynamic and evolves in time; a user can interact with a time-indication slider in order to move through the time sequence. Moreover the view of the Bloch sphere and its color palette may be adjusted by the user, allowing for a user to gain insights that may be challenging in a simple 2D representation. In this specific example, for instance, it becomes immediately obvious that a Hadamard gate has the action not only of transforming a state  $|+z\rangle \rightarrow |+x\rangle$ , but that it does so as a rotation about an axis tilted out of the equatorial plane of the Bloch sphere.

The visualizer module also provides a means by which one may intuitively explore the effect of noise on Unitary operations performed within quantum circuits. Two noise channels are available: control-amplitude noise  $\Omega \rightarrow \Omega(1 + \beta)$ ; and ambient dephasing noise  $\Delta \rightarrow \Delta + \eta$ , where  $\beta$  is the fractional fluctuation away from the target driving rate  $\Omega$  and  $\eta$  is a fluctuation away from the target detuning  $\Delta$ . In this circumstance the ideal state evolution is perturbed by the presence of noise, as illustrated by a displaced trajectory on the Bloch sphere. Ultimately, the discrepancy between the final location of the state at the end of the circuit and the ideal transformation, illustrated by a dotted line, provides a clear visual representation of how noise reduces the fidelity of a Unitary transformation.

Producing an intuitive visual representation of entanglement poses a significant challenge due to the presence of non-classical correlations between quantum systems. The Q-CTRL visualizer provides an exact representation of a two-qubit system exhibiting entanglement and subject to Unitary controls utilizing two Bloch spheres and

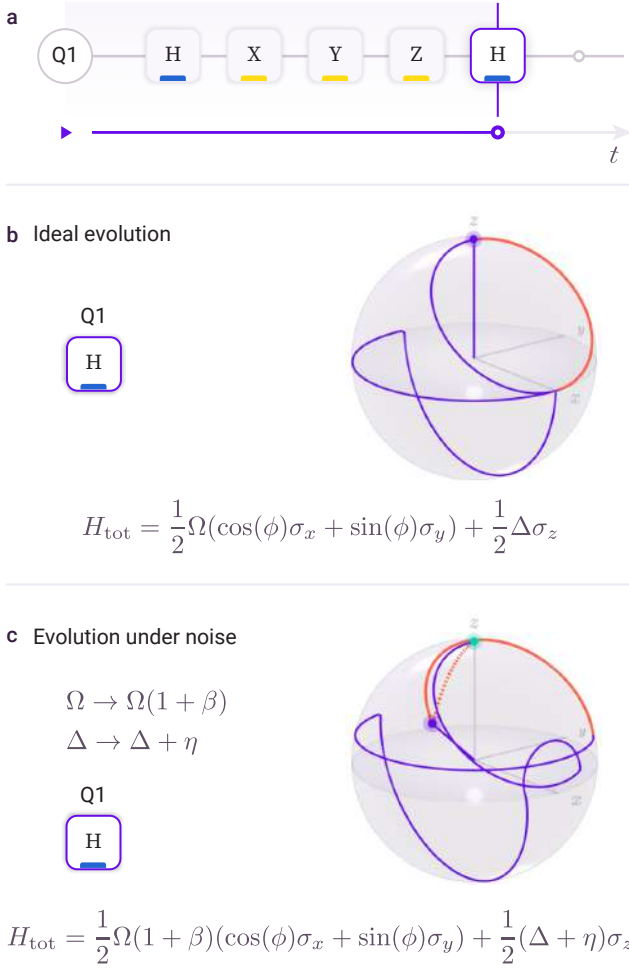


FIG. 17. Circuit evolution under noise. (a) The interactive Q-CTRL quantum circuit interface, paused during the second Hadamard gate (highlighted). (b) Evolution of the state vector (purple pointer) on the Bloch sphere, under ideal, noise-free conditions. The current trajectory on is highlighted in red (H-gate) which sequentially continues on the prior circuit evolution (purple). (c) Evolution of the state in the presence of two noise channels: control amplitude ( $\beta$ ) and ambient dephasing ( $\eta$ ). The cumulative error in the qubit state (dashed red) due to the presence of these noise channels is indicated by the dashed line, relative to the ideal target trajectory (green pointer).

three correlation tetrahedra. The Bloch spheres depict the standard Pauli observables corresponding to each of the qubits (Fig. 18(b)), given for qubits one and two respectively by:

$$\begin{aligned} X_1 &= \langle \sigma_x \otimes \mathbb{I} \rangle, \quad X_2 = \langle \mathbb{I} \otimes \sigma_x \rangle, \\ Y_1 &= \langle \sigma_y \otimes \mathbb{I} \rangle, \quad Y_2 = \langle \mathbb{I} \otimes \sigma_y \rangle, \\ Z_1 &= \langle \sigma_z \otimes \mathbb{I} \rangle, \quad Z_2 = \langle \mathbb{I} \otimes \sigma_z \rangle. \end{aligned} \quad (G2)$$

The surfaces of the Bloch spheres fully describe the space of separable states; the presence of any entanglement necessitates that the Bloch vectors shrink and the states

move off of the Bloch sphere surfaces. For instance, in Fig. 18(b), the magnitude of both Bloch vectors shrinks to zero following the first CNOT gate, as the system evolves into a maximally entangled Bell state as a result of this gate.

We visually depict entanglement using a set of observables corresponding to correlations between pairs of Cartesian observables for the two qubits. The correlation value between the observables is given by:

$$V(AB) = \langle \sigma_A \otimes \sigma_B \rangle - \langle \sigma_A \otimes \mathbb{I} \rangle \langle \mathbb{I} \otimes \sigma_B \rangle, \quad A, B \in \{X, Y, Z\}. \quad (G3)$$

The nine correlation-pairs are organized into three coordinate systems bounded by a tetrahedral geometry [78] given by the following axial arrangement of the observable pairs:  $(XX, YY, ZZ)$ ,  $(XY, YZ, ZX)$  and  $(XZ, YX, ZY)$ . For separable states all correlation values are zero and the visual indicator is set to the center of the tetrahedra. In the presence of non-zero entanglement, however, these visual indicators emerge from the origin of the correlation coordinate systems and grow towards the extrema of the convex hull for maximally entangled qubit pairs. The degree of entanglement is also visually represented using the concurrence  $C(\psi)$  defined as:

$$C(\psi) = 2|\langle 00|\psi\rangle\langle 11|\psi\rangle - \langle 01|\psi\rangle\langle 10|\psi\rangle|, \quad (G4)$$

which varies between 0 (separable states) and 1 (maximally entangled) throughout the system evolution, and shown using a horizontal indicator. Maximally entangled states may traverse the correlation tetrahedra when local unitaries are applied to the individual qubits, but the Bloch vectors remain at the centers of the Bloch spheres. Once again, noise processes may be added to the system's evolution in order to represent how the presence of noise perturbs the entangled states.

## Appendix H: Details on cloud architecture

Q-CTRLs suite of closed source products is designed and built upon a multitier application architecture. Often referred to as an  $n$ -tier architecture or multilayered architecture, a multitier architecture is a clientserver architecture in which presentation, logic, and data functions are physically separated. The most widespread use of the multitier architecture, and the form which Q-CTRL employs, is the three-tier architecture.

The three-tier architecture is a software architecture pattern in which the user interface (presentation), functional processes or *business rules* (logic), and data storage and access (data) are developed and maintained as independent layers.

By segregating an application into tiers, we acquire the option of modifying a specific layer, or even an individual component of each layer, instead of reworking the entire application. The three-tier architecture allows any tier

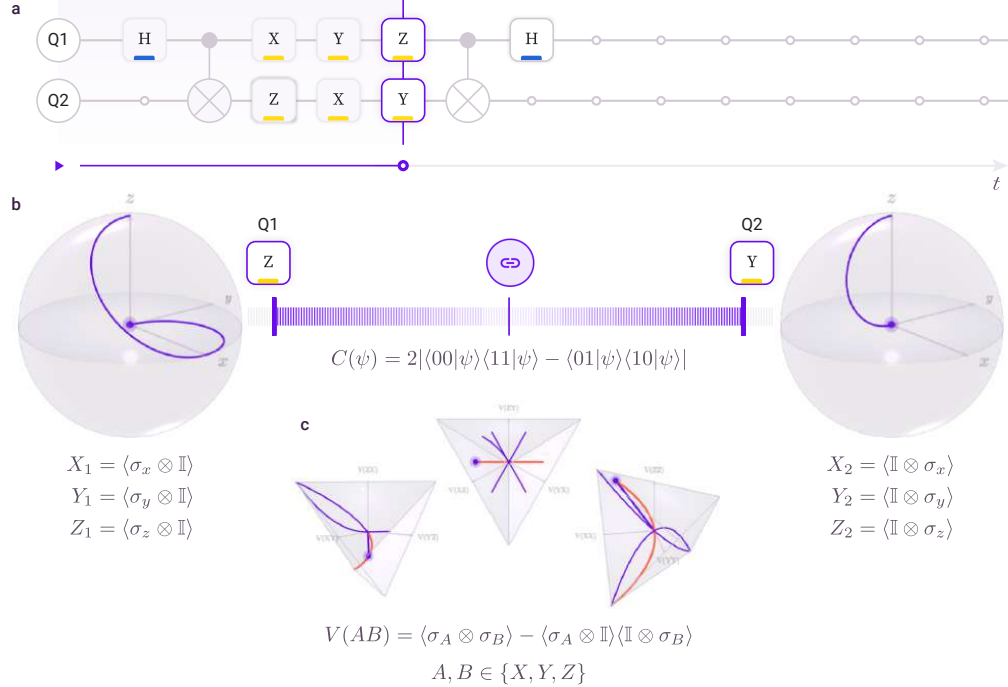


FIG. 18. Visualization of two-qubit entangled states using BLACK OPAL. (a) Evolution of a two-qubit entangling circuit paused during a pair of gates (circled in red). (b) The trajectories of individual qubit observables depicting separable states are represented on an interactive 3D Bloch sphere. The bloch vector goes to zero as qubits become entangled through the action of the CNOT gate. (c) Three interactive entanglement tetrahedra track correlations between the nine pairs of observables enabling visual representation of complete two-qubit state evolution. Concurrence indicates the level of entanglement (red markers) between the qubits throughout the evolution of the circuit. Control and/or dephasing noise may be added to assist in understanding its impact on the evolution of entangled states. Details of the visualization packages within BLACK OPAL are presented in App. G.

to be upgraded or replaced independently in response to changes in requirements or technology. For example, a change of database technology in the data tier would only affect the Application Programming Interface (API) code as the API is the interface between the data and logic tiers. Neither the presentation tier, nor any other component of the logic tier, would be aware of the change and would keep functioning as if there were no change at all. This provides a model by which we are able to create flexible, reusable and modular software with well-defined interfaces, or ways of communicating, between each tier.

### 1. Presentation tier

The presentation tier is the topmost level of the Q-CTRL application stack. This tier displays information related to such services as searching and viewing previous optimizations, creating new quantum circuit simulations or even signing up, logging in and managing your account subscription. It communicates with other tiers via the API component of the logic tier and is concerned with *presentation logic*, e.g. how the results of a simulation should be displayed, as opposed to *busi-*

*ness logic*, e.g. how a simulation is performed. In simple terms, it is the layer which users can access directly via, for example, a website such as the Q-CTRL Web App, or a client software package such as the Q-CTRL Python package. These two examples are part of the Q-CTRL product suite; however, due to the interoperable nature of the architecture it is possible for Q-CTRL customers to develop their own Custom applications that live alongside Q-CTRL-developed software on the presentation tier. Some examples of potential custom applications would be a client software package written in the R programming language or a tablet app used to design, simulate, and visualize quantum circuits.

### 2. Logic tier

The logic tier controls the applications functionality by performing detailed processing and consists of three distinct components: API, Queue, and Core. Controlled entirely by the API, the logic tier accepts requests from the presentation tier and routes them to the relevant layers and components within the stack. As mentioned above, the logic tier is concerned with business logic (sometimes

referred to as domain logic) and is the part of the application that encodes the real-world business rules that determine how data can be created, stored, and changed. It is contrasted with the other tiers of the application that are concerned with lower-level details of managing a database or presenting the user interface.

*API*: As mentioned above, the API provides the interface for, and is the entry point to, all requests made to the logic tier by the presentation tier. Strictly speaking, the API is a server-side web API consisting of a collection of public endpoints and can be characterized as being:

1. **Exposed via the web by means of a Hypertext Transfer Protocol (HTTP) web server**

The Hypertext Transfer Protocol (HTTP) is an application protocol. HTTP functions as a request/response protocol in the client/server computing model. A web browser running the Q-CTRL Web App, for example, may be the client and the Q-CTRL API, in this example, is the server. The client submits an HTTP request message to the server. The server, which provides resources such as JSON files and other content, or performs other functions (business logic) on behalf of the client, returns a response message to the client. The response contains completion status information about the request in the form of a HTTP status code (e.g. 201 Created) and may also contain requested content in its message body.

2. **Implemented in the Representational state transfer (REST) architectural style**

Representational state transfer (REST) is a software architectural style that defines a set of constraints to be used for creating Web services. Web services that conform to the REST architectural style, called RESTful Web services, provide interoperability between computer systems on the Internet. RESTful Web services allow the requesting systems to access and manipulate textual representations of Web resources by using a uniform and predefined set of stateless operations. By using a stateless protocol and standard operations, RESTful systems aim for fast performance, reliability, and the ability to grow by reusing components that can be managed and updated without affecting the system as a whole, even while it is running.

3. **Consisting of a well-defined request/response message system expressed in JavaScript Object Notation (JSON)**

JavaScript Object Notation (JSON) is an open-standard file or data interchange format that uses human-readable text to transmit data objects consisting of attribute/value pairs and array data types (or any other serializable value). It is a very common and language-independent data format with a diverse range of applications, including *e.g.* Openpulse formatting within Qiskit [40]. By using

a language-independent data format, the Q-CTRL API affords interoperability between systems, meaning applications can be developed in a wide array of languages and form factors.

4. **Formatted as per the JSON:API specification**

JSON:API is a specification for building RESTful APIs in JSON. The specification consists of a set of shared conventions relating to common requirements of RESTful APIs - including:

- Content negotiation: how a client should request and how a server should respond, including specific HTTP headers
- Document structure: how the JSON should be formatted
- Errors: How a server should respond in the case of an error, including specific HTTP status codes

By implementing the JSON:API specification, the Q-CTRL API provides client developers with the option to take advantage of generalized tooling in the form of the JSON:API compliant client libraries available in various languages, including Python, JavaScript, Ruby, R and iOS. Clients built around JSON:API are also able to take advantage of features relating to the efficient caching of responses, sometimes eliminating network requests entirely.

5. **Discoverable via an endpoint formatted as per the OpenAPI specification**

The OpenAPI Specification is a broadly adopted industry standard for describing modern RESTful APIs. Q-CTRL employs the OpenAPI specification as a way to both document its APIs, and to provide a means by which its APIs are discoverable by client applications. Q-CTRL's OpenAPI document is available at <https://api.q-ctrl.com/>. This is the root of Q-CTRL's API and acts as both a source of documentation for client application developers and as a discovery endpoint upon which client applications can self-generate client library code based on the specification. By adopting the OpenAPI specification, the Q-CTRL API provides client developers with the option to take advantage of generalized tooling in the form of OpenAPI compliant software such as auto document generation and industry standard API productivity and collaboration tools such as Postman.

*Queue*: The Queue is a distributed, asynchronous task scheduler based on distributed message passing. It is focused on real-time operation and also supports scheduling of long-running tasks (*e.g.* optimizations and simulations). Scheduling is the method by which work is assigned to resources that complete the work. In the case of Q-CTRL, the work is data flows performed by Core (see

below), which are in turn scheduled onto either shared or dedicated hardware resources.

The execution of tasks is performed concurrently on worker servers using multiprocessing and parallel processing to implement a variety of scheduling disciplines including (but not limited to): First come, first served (sometimes referred to as first in, first out or FIFO); Priority scheduling, and; Shortest remaining time first. The use of cloud-based worker servers allows the Queue to scale efficiently as the load and number of requests fluctuates. Additionally, the option for Q-CTRL customers to opt for dedicated hardware resources for the processing of their tasks enables even greater scaling and performance that would not be possible on personal hardware such as laptop devices.

The Queue is never accessed directly. Tasks are passed to the Queue by the API and execute asynchronously (in the background) so as not to disrupt or block the operation of client applications in the presentation tier. This allows users of the Q-CTRL Web App, for example, to request a control optimization to be performed and then to carry on using the app to perform other tasks while the requested optimization is performed in the background. Once the task is complete, the user is notified in-app and can then view the results.

*Core*: Core is the encapsulation of Q-CTRLs world-leading quantum control engineering expertise in the form of a Python package. However, unlike many Python packages that our customers are used to installing locally and accessing directly, Core (like the Queue above) is private and accessible via the Q-CTRL API. This allows Core to take advantage of the benefits of its siblings on the logic tier including: A language-independent interface allowing for almost unlimited interoperability and; Parallel processing on dedicated hardware for highly scalable performance.

### 3. Data tier

The data tier includes the data persistence mechanisms (database and storage), and the data access layer that encapsulates the persistence mechanisms and exposes the data. The data access layer provides an API to the logic tier that exposes methods of managing the stored data without exposing or creating dependencies on the data-storage mechanisms. As discussed earlier, avoiding dependencies on the storage mechanisms allows for updates or changes without the logic tier being affected by the change, allowing for easier scalability and maintenance.

*Database*: The Database is a relational database management system. While the database itself is simply an organized collection of data, the implementation of the relational model is used in concert with the concepts of domain-driven design in order to build a collection of data objects, and relationships (or cardinality) between these objects, to represent the domain of quantum control. For example, consider a series of one-to-many relationships

between data objects in which one system has many controls. Further, each object has attributes that further identify their context and purpose: a control can be one of three types (shift, drift or drive), whereas a simulation contains information relating to its initial state vector, point times and number of trajectories to be averaged.

As has been the case with all components of the application stack, the database is never accessed directly, rather, interactions are orchestrated via the API in order to maintain the security and integrity of the data contained within.

*Storage*: Storage is a file server that acts to provide access to static files accessible from disk. This is an alternative to retrieving information from the database which can be slow and unnecessary for requests that are common. For example, when certain types of optimizations or simulations prove to be commonplace or occurring regularly, the results are saved to storage as files which can be retrieved quickly without the need to queue the request for Core to reprocess.

## 4. Infrastructure

Providing the delivery mechanism for Q-CTRLs applications is the physical IT infrastructure comprising both physical equipment such as bare-metal servers as well as virtual machines and associated configuration resources. Provisioned on any cloud - public, private, hybrid or on-premise - and via the use of infrastructure as code (IaC) processes, Q-CTRLs infrastructure provides a platform for its applications to ensure the following at all times:

### 1. Performance:

- Utilization of more hardware-on-demand than could possibly fit into a consumer PC
- Utilization of all CPUs
- GPU acceleration
- Pre-compiled binaries

### 2. Availability:

- Redundancy in hardware due to infrastructure hosted across multiple availability zones in order to survive outage of a given data centre
- Autohealing via service checks with containers automatically restarted if health checks fail
- Cloud agnostic and code-driven so we can quickly re-deploy to another cloud provider if required
- Monitoring and alerting

### 3. Portability:

- Infrastructure as code (IaC)
- Containerized with Docker
- Orchestrated with Kubernetes

#### 4. Scalability:

- Autoscaling with the ability to add more compute resources on demand via public cloud providers
- Almost infinitely scalable and not limited to resources we need to provision and host ourselves
- Images tuned to start up as quickly as possible when joining the cluster
- Ability to scale down resources when not required (cost effective)

#### 5. Security:

- Nothing can reach production environments without going through a defined pipeline, starting with code. This ensures that we know that the state of our environment matches exactly what has been declared in code, and that everything that is deployed has gone through

a quality assurance and security check process. For example, all code and dependencies go through a security vulnerability check

- End-to-end SSL
- Enterprise-grade secrets management, leveraging HSMs for key management
- All network traffic is via Ingress
- Only select teams have access to virtual machines and containers running in the cluster
- All access is monitored and logged
- Leverages security provided by public cloud providers, e.g. Google Cloud Platform (GCP), Amazon Web Services (AWS), Microsoft Azure, etc.
- Kubernetes cluster upgrades and database security upgrades are applied automatically
- Zero-trust networking
- Applications run on non-privileged accounts inside Docker containers for greater isolation of running processes
- Surface attack area minimised by only deploying required components on minimalist CoreOS images that are constantly updated with security patches

---

[1] J. Preskill, *Quantum* **2**, 79 (2018).

[2] R. P. Feynman, *International Journal of Theoretical Physics* **21**, 467 (1982).

[3] J. Hennessy and D. Patterson, *Computer Architecture* (Morgan Kaufmann, 2017).

[4] A. W. Cross, L. S. Bishop, S. Sheldon, P. D. Nation, and J. M. Gambetta, *Phys. Rev. A* **100**, 032328 (2019).

[5] M. A. Nielsen and I. L. Chuang, *Quantum Computation and Quantum Information* (Cambridge University Press, 2001).

[6] R. F. Stengel, *Optimal Control and Estimation* (Dover Publications, 1994).

[7] R. C. Dorf and R. H. Bishop, *Modern Control Systems* (Pearson, 2016).

[8] T. D. Crouch, *The Bishop's Boys* (W. W. Norton and Company, 2003).

[9] I. Bhati, M.-T. Chang, Z. Chishti, S.-L. Lu, and B. Jacob, *IEEE Transactions on Computers* **65**, 1 (2015).

[10] T. J. Tarn, G. Huang, and J. W. Clark, *Mathematical Modelling* **1**, 109 (1980).

[11] J. W. Clark, D. G. Lucarelli, and T. J. Tarn, *Int. J. Mod. Phys. B* **17**, 5397 (2003).

[12] D. Dong and I. Petersen, *IET Control Theory and Applications* **4**, 1651 (2010).

[13] L. Bouting, R. V. Handel, and M. R. James, *SIAM J. Control Optim.* **46**, 2199 (2007).

[14] H. I. Nurdin, M. R. James, and I. R. Petersen, *Automatica* **45**, 1837 (2009).

[15] M. J. Biercuk, A. C. Doherty, and H. Uys, *J. Phys. B* **44**, 154002 (2011).

[16] T. J. Green, J. Sastrawan, H. Uys, and M. J. Biercuk, *New J. Phys.* **15**, 095004 (2013).

[17] A. Soare, H. Ball, D. Hayes, J. Sastrawan, M. C. Jarrett, J. J. McLoughlin, X. Zhen, T. J. Green, and M. J. Biercuk, *Nat. Phys.* **10**, 825 (2014).

[18] R. S. Gupta and M. J. Biercuk, *Phys. Rev. Applied* **9**, 064042 (2018).

[19] R. S. Gupta, A. R. Milne, C. L. Edmunds, C. Hempel, and M. J. Biercuk, “Autonomous adaptive noise characterization in quantum computers,” (2019), [arXiv:1904.07225 \[quant-ph\]](https://arxiv.org/abs/1904.07225).

[20] U. Haeberlen and J. S. Waugh, *Phys. Rev.* **175**, 453 (1968).

[21] S. Chaudhury, S. Merkel, T. Herr, A. Silberfarb, I. H. Deutsch, and P. S. Jessen, *Phys. Rev. Lett.* **99**, 163002 (2007).

[22] A. Smith, B. E. Anderson, H. Sosa-Martinez, C. A. Riofrío, I. H. Deutsch, and P. S. Jessen, *Phys. Rev. Lett.* **111**, 170502 (2013).

[23] R. W. Heeres, P. Reinhold, N. Ofek, L. Frunzio, L. Jiang, M. H. Devoret, and R. J. Schoelkopf, *Nature Communications* **8**, 94 (2017).

[24] A. D. Tranter, H. J. Slatyer, M. R. Hush, A. C. Leung, J. L. Everett, K. V. Paul, P. Vernaz-Gris, P. K. Lam, B. C. Buchler, and G. T. Campbell, *Nature Communications* **9**, 4360 (2018).

[25] P. B. Wigley, P. J. Everitt, A. van den Hengel, J. W. Bastian, M. A. Sooriyabandara, G. D. McDonald, K. S. Hardman, C. D. Quinlivan, P. Manju, C. C. N. Kuhn, I. R. Petersen, A. N. Luiten, J. J. Hope, N. P. Robins, and M. R. Hush, *Scientific Reports* **6**, 25890 (2016).

[26] B. M. Henson, D. K. Shin, K. F. Thomas, J. A. Ross, M. R. Hush, S. S. Hodgman, and A. G. Truscott, *Proceedings of the National Academy of Sciences* **115**, 13216 (2018), <https://www.pnas.org/content/115/52/13216.full.pdf>.

[27] N. C. Jones, R. Van Meter, A. G. Fowler, P. L. McMahon, J. Kim, T. D. Ladd, and Y. Yamamoto, *Phys. Rev. X* **2**, 031007 (2012).

[28] J. T. Merrill and K. R. Brown, “Progress in compensating pulse sequences for quantum computation,” in *Quantum Information and Computation for Chemistry* (John Wiley & Sons, Ltd, 2014) pp. 241–294.

[29] S. Lloyd, *Phys. Rev. A* **62**, 022108 (2000).

[30] A. C. Doherty, K. Jacobs, and G. Jungman, *Phys. Rev. A* **63**, 062306 (2001).

[31] S. Mavadia, V. Frey, J. Sastrawan, S. Dona, and M. J. Biercuk, *Nature Communications* **8**, 14106 (2017).

[32] S. Majumder, L. A. de Castro, and K. R. Brown, “Real-time calibration with spectator qubits,” (2019), [arXiv:1907.03864 \[quant-ph\]](https://arxiv.org/abs/1907.03864).

[33] R. S. Gupta and M. J. Biercuk, “Convergence analysis for autonomous adaptive learning applied to quantum architectures,” (2019), [arXiv:1911.05752 \[quant-ph\]](https://arxiv.org/abs/1911.05752).

[34] R. Vijay, C. Macklin, D. H. Slichter, S. J. Weber, K. W. Murch, R. Naik, A. N. Korotkov, and I. Siddiqi, *Nature* **490**, 77 (2012).

[35] M. Hirose and P. Cappellaro, *Nature* **532**, 77 (2016).

[36] P. Murali, J. M. Baker, A. J. Abhari, F. T. Chong, and M. Martonosi, “Noise-adaptive compiler mappings for noisy intermediate-scale quantum computers,” (2019), [arXiv:1901.11054 \[quant-ph\]](https://arxiv.org/abs/1901.11054).

[37] S. Nishio, Y. Pan, T. Satoh, H. Amano, and R. V. Meter, “Extracting success from ibm’s 20-qubit machines using error-aware compilation,” (2019), [arXiv:1903.10963 \[quant-ph\]](https://arxiv.org/abs/1903.10963).

[38] C. L. Edmunds, C. Hempel, R. J. Harris, V. M. Frey, T. M. Stace, and M. J. Biercuk, “Dynamically corrected gates suppress spatio-temporal error correlations as measured by randomized benchmarking,” (2019), [arXiv:1909.10727 \[quant-ph\]](https://arxiv.org/abs/1909.10727).

[39] J. P. Barnes, C. J. Trout, D. Lucarelli, and B. D. Clader, *Phys. Rev. A* **95**, 062338 (2017).

[40] D. C. McKay, T. Alexander, L. Bello, M. J. Biercuk, L. Bishop, J. Chen, J. M. Chow, A. D. Croles, D. Egger, S. Filipp, J. Gomez, M. Hush, A. Javadi-Abhari, D. Moreda, P. Nation, B. Paulovicks, E. Winston, C. J. Wood, J. Wootton, and J. M. Gambetta, “Qiskit backend specifications for OpenQasm and OpenPulse experiments,” (2018), [arXiv:1809.03452 \[quant-ph\]](https://arxiv.org/abs/1809.03452).

[41] K. Rudinger, S. Kimmel, D. Lobser, and P. Maunz, *Phys. Rev. Lett.* **118**, 190502 (2017).

[42] S. Gustavsson, O. Zwier, J. Bylander, F. Yan, F. Yoshihara, Y. Nakamura, T. P. Orlando, and W. D. Oliver, *Physical Review Letters* **110** (2013), 10.1103/physrevlett.110.040502.

[43] M. Jerger, A. Kulikov, Z. Vasselin, and A. Fedorov, *Physical Review Letters* **123** (2019), 10.1103/physrevlett.123.150501.

[44] M. A. Rol, L. Ciorciaro, F. K. Malinowski, B. M. Tarasin-ski, R. E. Sagastizabal, C. C. Bultink, Y. Salathe, N. Haandbaek, J. Sedivy, and L. DiCarlo, “Time-domain characterization and correction of on-chip distortion of control pulses in a quantum processor,” (2019), [arXiv:1907.04818 \[quant-ph\]](https://arxiv.org/abs/1907.04818).

[45] U. Haeberlen and J. S. Waugh, *Phys. Rev.* **175**, 453 (1968).

[46] A. Kofman and G. Kurizki, *Phys. Rev. Lett.* **87**, 270405 (2001).

[47] A. G. Kofman and G. Kurizki, *Phys. Rev. Lett.* **93**, 130406 (2004).

[48] G. Uhrig, *Phys. Rev. Lett.* **98**, 100504 (2007).

[49] G. A. Paz-Silva and L. Viola, *Phys. Rev. Lett.* **113**, 250501 (2014).

[50] S. Blanes, F. Casas, J. A. Oteo, and J. Ros, *Phys. Rep.* **470**, 151 (2009).

[51] W. Magnus, *Commun. Pure and Appl. Math.* **7**, 649 (1954).

[52] A. R. Milne, C. L. Edmunds, C. Hempel, F. Roy, S. Mavadia, and M. J. Biercuk, “Phase-modulated entangling gates robust to static and time-varying errors,” (2018), [arXiv:1808.10462 \[quant-ph\]](https://arxiv.org/abs/1808.10462).

[53] T. Caneva, T. Calarco, and S. Montangero, *Phys. Rev. A* **84**, 022326 (2011).

[54] P. Doria, T. Calarco, and S. Montangero, *Phys. Rev. Lett.* **106**, 190501 (2011).

[55] “IBM Q,” <http://web.archive.org/web/20080207010024/http://www.808multimedia.com/winnt/kernel.htm> (2019).

[56] “pyGSTi,” <https://www.pygsti.info> (2019).

[57] F. Motzoi, J. M. Gambetta, P. Rebentrost, and F. K. Wilhelm, *Phys. Rev. Lett.* **103**, 110501 (2009).

[58] R. Harper, S. T. Flammia, and J. J. Wallman, “Efficient learning of quantum noise,” (2019), [arXiv:1907.13022 \[quant-ph\]](https://arxiv.org/abs/1907.13022).

[59] T. J. Evans, R. Harper, and S. T. Flammia, “Scalable bayesian hamiltonian learning,” (2019), [arXiv:1912.07636 \[quant-ph\]](https://arxiv.org/abs/1912.07636).

[60] S. Krastanov, S. Zhou, S. T. Flammia, and L. Jiang, *Quantum Science and Technology* **4**, 035003 (2019).

[61] Here the factor 1/2 implements the trapezoidal rule.

[62] T. J. Green and M. J. Biercuk, *Phys. Rev. Lett.* **114**, 120502 (2015).

[63] M. Reagor, C. B. Osborn, N. Tezak, A. Staley, G. Prawiroatmodjo, M. Scheer, N. Alidoust, E. A. Sete, N. Didier, M. P. da Silva, E. Acala, J. Angeles, A. Bestwick, M. Block, B. Bloom, A. Bradley, C. Bui, S. Caldwell, L. Capelluto, R. Chilcott, J. Cordova, G. Crossman, M. Curtis, S. Deshpande, T. El Bouayadi, D. Girshovich, S. Hong, A. Hudson, P. Karalekas, K. Kuang, M. Lenihan, R. Manenti, T. Manning, J. Marshall, Y. Mohan, W. O’Brien, J. Otterbach, A. Papageorge, J.-P. Paquette, M. Pelstring, A. Polloreno, V. Rawat, C. A. Ryan, R. Renzas, N. Rubin, D. Russel, M. Rust, D. Scarabelli, M. Selvanayagam, R. Sinclair, R. Smith, M. Suska, T.-W. To, M. Vahidpour, N. Vodrahalli, T. Whyland, K. Yadav, W. Zeng, and C. T. Rigetti, *Science Advances* **4** (2018), 10.1126/sciadv.aaq3603.

[64] N. Didier, E. A. Sete, M. P. da Silva, and C. Rigetti, *Phys. Rev. A* **97**, 022330 (2018).

[65] R. Schutjens, F. A. Dagga, D. J. Egger, and F. K. Wilhelm, *Phys. Rev. A* **88**, 052330 (2013).

[66] J. Koch, T. M. Yu, J. Gambetta, A. A. Houck, D. I. Schuster, J. Majer, A. Blais, M. H. Devoret, S. M. Girvin,

and R. J. Schoelkopf, Phys. Rev. A **76**, 042319 (2007).

[67] S. A. Caldwell and *et al.*, Phys. Rev. Applied **10**, 034050 (2018).

[68] H. Ball and M. J. Biercuk, EPJ Quantum Technol. **2**, 11 (2015), 10.1140/epjqt/s40507-015-0022-4.

[69] J. Bylander, S. Gustavsson, F. Yan, F. Yoshihara, K. Harrabi, G. Fitch, D. G. Cory, Y. Nakamura, J.-S. Tsai, and W. D. Oliver, Nat. Phys. **7**, 565 (2011).

[70] G. A. Álvarez and D. Suter, Phys. Rev. Lett. **107**, 230501 (2011).

[71] C. Ferrie, C. Granade, G. Paz-Silva, and H. M. Wiseman, New Journal of Physics **20**, 123005 (2018).

[72] V. Frey, Ph.D. thesis, The University of Sydney, NSW 2006, Australia (2019).

[73] “IBM Q 5 Tenerife,” [https://github.com/Qiskit/qiskit\\_ibmq-device-information/tree/master/backends/tenerife/V1](https://github.com/Qiskit/qiskit_ibmq-device-information/tree/master/backends/tenerife/V1) (2019).

[74] The assumption of independence is reasonable, for instance, in the case of a driving field where random fluctuations in frequency and amplitude arise from different physical processes. A general model including correlations between noise processes is possible, however, following the approach outlined by Green *et al.* [16].

[75] S. L. Miller and D. Childers, *Probability and Random Processes with Applications to Signal Processing and Communications* (Academic Press, Boston, MA, 2012).

[76] P. Gokhale, Y. Ding, T. Propson, C. Winkler, N. Leung, Y. Shi, D. I. Schuster, H. Hoffmann, and F. T. Chong, Proceedings of the 52nd Annual IEEE/ACM International Symposium on Microarchitecture - MICRO 52 (2019), 10.1145/3352460.3358313.

[77] Y. Shi, N. Leung, P. Gokhale, Z. Rossi, D. I. Schuster, H. Hoffmann, and F. T. Chong, Proceedings of the Twenty-Fourth International Conference on Architectural Support for Programming Languages and Operating Systems - ASPLOS 19 (2019), 10.1145/3297858.3304018.

[78] K. Modi, A. Brodutch, H. Cable, T. Paterek, and V. Vedral, Rev. Mod. Phys. **84**, 1655 (2012).